Copy No. _____

Defence Research and Development Canada
Recherche et développement pour la défense Canada

DEFENCE R&D DÉFENSE

Superomniphobic Surfaces for Military Applications: Nano- and Micro-Fabrication Methods

Year Two Report

Alidad Amirfazli

Prepared by:
Alidad Amirfazli
Department of Mechanical Engineering
University of Alberta
Edmonton, AB T6G 2G8

Contract Scientific Authority: Paul Saville, 250-363-2892
PWGSC Contract Number: W7707-098197

Defence R&D Canada – Atlantic

Contract Report
DRDC Atlantic CR 2011-255
December 2011

Canada

This page intentionally left blank.

Superomniphobic Surfaces for Military Applications: Nano- and Micro-Fabrication Methods

Year Two Report

Alidad Amirfazli

Prepared By:
Alidad Amirfazli
Department of Mechanical Engineering
University of Alberta
Edmonton, Alberta T6G 2G8

CSA: Paul Saville, 250-363-2892
PWGSC Contract Number: W7707-098197

Defence R&D Canada – Atlantic

Contract Report
DRDC Atlantic CR 2011-255
December 2011

Principal Author

Original signed by Alidad Amirfazli

Alidad Amirfazli

Approved by

Original signed by Gary Fisher

Gary Fisher

Head Dockyard Laboratory Pacific

Approved for release by

Original signed by Calvin Hyatt

Calvin Hyatt

Head Document Review Panel

This work sponsored under 12SZ20

Abstract

This report explains the work accomplished during the reporting period (i.e. year 2) in four main areas: (i) Continued development of practical repellent coatings; a procedure was developed that results in improved durability under abrasion and water immersion while maintaining coating versatility. Additionally, a set of different layered superhydrophobic coatings have been proposed. (ii) Understanding the relationship between surface wear and wetting characteristics for superhydrophobic surfaces: a methodology was devised using confocal scanning microscopy that permits collection of quantitative information for surface texture. This, combined with measuring the contact angles on superhydrophobic coatings that were worn systematically, was used to compare findings with the predictions based on the classical Cassie equation. The need to develop a new relationship was identified. (iii) Theoretical work on developing fundamental knowledge about wetting of textured surfaces; a thermodynamic depiction of edge effect has been developed by free energy analysis. Results show good agreement with previous works. A universal wetting plot for describing the four wetting regions was obtained relating edge angle and intrinsic contact angle. The results have provided fundamental rules for designing robust superhydrophobic and superoleophobic surfaces. (iv) Fabrication of textured surfaces by lithographic methods to achieve repellency for oily liquids and surfactant solutions; not only were the re-entrant structures proposed in the original proposal produced, but a new structured surface, called silicon grass that shows considerable promise for oleophobicity, when compared to the re-entrant structures, was produced. The results of this work have been published in peer reviewed publications, and presented at international conferences.

Résumé

Le présent rapport explique les travaux réalisés durant la période du rapport (c.-à-d. année 2) dans quatre domaines : (i) Élaboration continue de revêtements imperméables : Une procédure conférant une meilleure durabilité aux matériaux soumis à l'abrasion et à l'immersion dans l'eau, tout en maintenant la polyvalence du revêtement a été mise au point. De plus, un ensemble de différents revêtements superposés a été proposé. (ii) Comprendre la relation entre l'usure de surface et les caractéristiques de mouillage des surfaces superhydrophobes : une méthode a été créée à l'aide d'un microscope confocal à balayage qui permet de recueillir de l'information quantitative sur la texture de la surface. Cette méthode, combinée à la mesure des angles de contact sur des revêtements superhydrophobes qui étaient usés systématiquement, a été utilisée pour comparer les résultats avec les prévisions basées sur l'équation classique de Cassie. La nécessité de développer une nouvelle relation a été identifiée. (iii) Travaux théoriques portant sur le développement de connaissances fondamentales sur le mouillage des surfaces texturées : Une représentation thermodynamique de l'effet de bord a été mise au point dans le cadre d'une analyse de l'énergie libre. Les résultats montrent une bonne concordance avec les travaux antérieurs. Une représentation graphique universelle du mouillage décrivant les quatre régions de mouillage et mettant en relation l'angle de bord et l'angle de contact intrinsèque a été obtenue. Les résultats ont permis de déterminer les règles fondamentales pour la conception de surfaces superhydrophobes et superoléophobes robustes. (iv) Fabrication de surfaces texturées grâce à des méthodes lithographiques pour repousser des liquides huileux et des solutions contenant des

surfactants : Non seulement des structures rentrantes ont-elles été proposées dans la proposition originale, mais également une nouvelle surface structurée, appelée « pelouse de silicium », qui semble prometteuse à cause de ses propriétés oléophobes, lorsqu'on la compare aux structures rentrantes, a été produite. Les résultats de ces travaux ont été publiés dans des publications à comité de lecture, et présentés lors de conférences internationales.

Executive summary

Superomniphobic Surfaces for Military Applications: Nano- and Micro-Fabrication Methods: Year Two Report

Amirfazli, A.; DRDC Atlantic CR 2011-255; Defence R&D Canada – Atlantic; December 2011.

Introduction: This report explains the work accomplished during the reporting period (i.e. year 2) in four main areas: (i) continued development of practical repellent coatings; (ii) understanding the relationship between surface wear and wetting characteristics for superhydrophobic surfaces; (iii) theoretical work on developing fundamental knowledge about wetting of textured surfaces; and (iv) fabrication of textured surfaces by lithographic methods to achieve repellency for oily liquids and surfactant solutions.

Results: With regards to (i), improved coating formulations have been developed for better coating stability in water. The results from such investigations should produce improved durability under surface abrasion and prolonged water immersion. Finding a relationship between surface topography and wetting behaviour (Area ii) is the most challenging part of the project. Such understanding is very important for development of durable superhydrophobic coatings. Surface texture information, from confocal scanning microscopy and contact angle measurements of systematically worn coatings, were used to compare the wetting predictions based on the classical Cassie equation. Based on this data, it may be that the Cassie equation is not a good predictor for practical worn surfaces, and a new relationship is required. (iii) Superomniphobic surfaces have been developed empirically by taking advantage of sharp edges, e.g. a re-entrant structures. However, the thermodynamic mechanism of edge effect was incompletely understood. A thermodynamic depiction of edge effect has been given by Free Energy analysis. Results show good agreement with previous works. A universal wetting plot for describing the four wetting regions is obtained relating edge angle and intrinsic contact angle. The results have provided fundamental rules for designing robust superhydrophobic and superoleophobic surfaces. (iv) Re-entrant structures have been successfully produced along with a new structure, herein termed silicon grass, that show considerable promise for oleophobicity, when compared to the re-entrant structures.

Significance: This work is establishing the basis for producing durable materials with military relevance. The theoretical work provides a means through which practical materials can be designed. The wear studies are important for the development of durable materials as many superhydrophobic surfaces developed to date are fragile and readily become wettable. The development of practical coatings and lithographically produced surfaces may lead to the production of materials that repel water and oils which will have many applications for personnel and equipment protection.

Future plans: Work will continue on the four fields discussed above, particularly, trialling the superhydrophobic coating, extending wear analysis to highly defined systems such as lithographically produced array, and the continued development of lithographically produced oleophobic structures.

Sommaire

Superomniphobic Surfaces for Military Applications: Nano- and Micro-Fabrication Methods: Year Two Report

Amirfazli, A. ; DRDC Atlantic CR 2011-255 ; R & D pour la défense Canada – Atlantique; décembre 2011.

Introduction : Le présent rapport explique les travaux réalisés durant la période du rapport (c.-à-d. année 2) dans quatre domaines principaux : (i) Élaboration continue de revêtements imperméables; (ii) Comprendre la relation entre l'usure de surface et les caractéristiques de mouillage des surfaces superhydrophobes; (iii) Travaux théoriques portant sur le développement de connaissances fondamentales sur le mouillage des surfaces texturées; et (iv) Fabrication de surfaces texturées grâce à des méthodes lithographiques pour repousser des liquides huileux et des solutions contenant des surfactants.

Résultats : Pour ce qui est de (i), des formulations de revêtement améliorées ont été mises au point pour améliorer la stabilité des revêtements dans l'eau. Les résultats de ces examens doivent conférer une meilleure durabilité aux matériaux soumis à l'abrasion et à l'immersion dans l'eau. Trouver une relation entre les aspérités de la surface et le comportement de mouillage (région ii) est le plus grand défi du projet. Il est très important de comprendre cette relation pour mettre au point des revêtements superhydrophobes durables. L'information sur la texture de la surface, à l'aide d'un microscope confocal à balayage et de mesures de l'angle de contact sur des revêtements usés systématiquement, a été utilisée pour comparer les prévisions du mouillage basées sur l'équation classique de Cassie. À la lumière de ces données, il se peut que l'équation de Cassie ne soit pas un bon outil de prévision dans le cas des surfaces usées, et une nouvelle relation est requise. (iii) Des surfaces superomniphobes ont été mises au point empiriquement en tirant profit des arêtes vives, par exemple les structures rentrantes. Cependant, les connaissances relatives au mécanisme de thermodynamique de l'effet de bord gagneraient à être approfondies. Une représentation thermodynamique de l'effet de bord a été obtenue à l'aide d'une analyse de l'énergie libre. Les résultats montrent une bonne concordance avec les travaux antérieurs. Une représentation graphique universelle du mouillage décrivant les quatre régions de mouillage et mettant en relation l'angle de bord et l'angle de contact intrinsèque a été obtenue. Les résultats ont permis de déterminer les règles fondamentales pour la conception de surfaces superhydrophobes et superoléophobes robustes. (iv) Des structures rentrantes ont été produites avec succès ainsi qu'une nouvelle structure, appelée ici « pelouse de silicium », qui semble prometteuse à cause de ses propriétés oléophobes, lorsqu'on la compare aux structures rentrantes.

Importance : Ces travaux ont établi les fondements de la production de matériaux durables pertinents pour les militaires. Les travaux théoriques sont un moyen de concevoir des matériaux pratiques. Les études sur l'usure sont importantes pour élaborer des matériaux durables, étant donné que de nombreuses surfaces superhydrophobes élaborées à ce jour sont fragiles et deviennent rapidement mouillables. L'élaboration de revêtements pratiques et de surfaces produites par lithographie pourrait mener à la production de matériaux qui repoussent l'eau et les huiles et qui auront de nombreuses applications dans la protection du personnel et de l'équipement.

Perspectives : Les travaux se poursuivent dans les quatre domaines mentionnés précédemment, particulièrement les essais sur les revêtements superhydrophobes, l'application de l'analyse sur l'usure à des systèmes de haute définition, comme les réseaux lithographiques et l'élaboration continue de structures oléophobes produites par lithographie.

This page intentionally left blank.

Table of contents

Abstract ……. i
Résumé ….... i
Executive summary iii
Sommaire iv
Table of contents vii
List of figures ix
List of tables xv
1 Overview..... 1
2 Sprayable Superhydrophobic Coatings..... 2
2.1 Introduction 2
2.2 Brief Summary of Previous Reporting Period..... 2
2.3 Updates and Changes to SH Recipe, Spray Application and Testing Procedures..... 3
2.3.1 Changes to adhesive and sealant and the addition of Teflon® AF 3
2.3.2 Changes to solvent..... 4
2.3.3 Changes to nano-particles..... 5
2.3.4 Final/Current mix and mixing procedure..... 5
2.3.5 Changes to spray techniques..... 6
Curing Technique Investigations 9
2.3.5.1 Introduction and Background Information 9
2.3.5.2 Materials & Methods 10
2.3.5.3 Results and Analysis: Part 1 – B22-A..... 12
2.3.5.4 Results and Analysis: Part 2 – B22-B & B22-C 14
2.3.5.5 Summary and Conclusions..... 17
2.3.5.6 Recommendations and Future Work..... 18
2.4 SH Coating in Digital Microfluidics: Lab-on-Chip & Lab-on-Paper Applications 18
2.5 Superhydrophobic Coating Application and Testing Study Plan 19
2.5.1 Introduction..... 19
2.5.2 Objectives 20
2.5.3 Materials and Methods 20
2.6 Current and Future Work: Alternative SH Coatings 23
2.6.1 Introduction..... 23
2.6.2 Materials and Methods 23
2.6.3 Discussion of Proposed Alternative SH Coatings 23
2.6.4 Conclusions 29
2.7 Summary and Conclusions..... 29
3 Wetting Performance of Worn Superhydrophobic Surfaces..... 30
3.1 Introduction 30

3.2 Experimental Section ... 31
3.2.1 Noise filtering of the CSM data ... 33
3.2.2 Calculating Cassie contact angles and penetration depths ... 37
3.2.3 Prediction of wetting for worn surfaces ... 42
3.3 Future work ... 51
4 A Thermodynamic Approach for Understanding the EdgeEffect on Wetting ... 52
4.1 Introduction ... 52
4.2 Theoretical Section ... 54
4.2.1 Edge effect theories ... 54
4.2.2 Thermodynamic Model ... 56
4.3 Results and Discussion ... 58
4.3.1 Thermodynamic Origin of the Edge Effect ... 58
4.3.2 Four Typical Drop Wetting States ... 60
4.3.3 Drop Wetting Graphics on Single Pillar ... 64
4.4 Conclusions ... 66
4.5 Associated Content ... 67
5 Superhydrophobic and Superoleophobic Behaviour on Variant Geometry Micropillar Arrays ... 68
5.1 Introduction ... 68
5.2 Photomask Design ... 68
5.3 Fabrication Process ... 69
5.4 Specific Fabrication and Results ... 70
5.5 Future Work ... 88
References ... 90
Annex A SEM Images for different Curing Techniques ... 95
Annex B A Thermodynamic Approach for Understanding the Edge Effect on Wetting: Supplementary Information for Section 3 ... 99
List of symbols/abbreviations/acronyms/initialisms ... 102
Distribution list ... 105

List of figures

Figure 2-1: Spray gun nozzle components: a) Nozzle; b) Internal pin holder; c) Spring for spray thickness control; d) Pin for spray thickness control. Nozzle assembly with and without c) & d) allows for thin vs. thick sprays. 7

Figure 2-2: Plot of the different thicknesses achieved by each of the four different treatments, where * corresponds to the respective batch number. Measurements were taken with a micrometer on treated microscope glass slides (compensating for 1.0mm glass thickness). It can be seen that 1 layer of thick treatment (B*T) is roughly the same as 2 layers of thin treatment (2XB*). 8

Figure 2-3: 1000X Scanning Electron Microscopy (SEM) Images of Unimmersed (a) and Immersed (b) microscope glass slides treated with 2XB21T. It can be seen that the unimmersed (a) image shows a rougher surface then the smoother immersed (b) image. Also, various pinholes (arrows) are also visible on the immersed image and not on the unimmersed image. The pinholes shown could be evidence of the release of solvent entrapment in the sprayed coating. 9

Figure 2-4: Schematic of the treated glass sample showing the relevant portions for the preliminary immersion test performed. 12

Figure 2-5: Plots of the CA measurements for the first 9 treated samples for each of the curing methods. CA measurements were taken before immersion, after immersion and after 1 week in ambient conditions. It can be seen that the samples that cured in vacuum have the best overall wetting performance with the lowest hysteresis when compared to curing at room temperature or at 75˚C at ambient pressure. 13

Figure 2-6: CA measurements for the control samples for each of the three separate batches of B22 made. Although the wetting performance is very similar between the three separate B22 batches, some differences are still noticeable and can be attributed to differences in coating thickness and differences in mixing ratios of the components that make up the SH coating. 14

Figure 2-7: CA measurements for the three different vacuum curing scenarios using samples B22-A, B22-B, and B22-C: a) Vacuum for 3 hours at 75°C, b) Vacuum for 24 hours at 21°C and c) Vacuum for 24 hours at 75°C. It can be seen from the plots that curing at vacuum and temperature (a and c) produces a better performing surface than curing in vacuum at room temperature (b). 15

Figure 2-8: Distribution of samples across the different steel plates and different pre-treatments. 22

Figure 3-1: Schematic showing how drop is able to roll off easily on undamaged SHS (a), drop is immobile on a damaged SHS (b). 31

Figure 3-2: SEM of unworn plasma etched Teflon® 32

Figure 3-3: a) Artificial spikes created around the edge of an engraving on a coin. b) Same line profile after noise filtering. 20x Objective is used in the imaging. 33

Figure 3-4: Schematic of pyramid algorithm for filtering the noise. Each pixel in image is analyzed for values above threshold and reduced step by step using Gaussian pyramid. Original image is re-created by replacing zero-weight pixels with new pixel values given by pyramid function. This removes artificial spikes created around edges..... 34

Figure 3-5: SEM of 27 minutes glass beads abraded Teflon® sample. The line on the image is Representative of CSM line profile in Figure 3-6a and b..... 35

Figure 3-6: (a) Line profile across a sample worn for 27 minutes. Both axes are in μm. (b): Line profile across a CSM data on 27 min abraded Teflon® sample after noise filtering. Both axes are in μm. Notice that only outliers have been affected on by the filter and finer features are intact. (c): Line profile across a CSM data on 27 min abraded Teflon® sample after noise filtering on a different place than one depicted in (a) and (b). Notice a peak not affected by noise filtering. Both axes are in μm. 36

Figure 3-7: Histogram filtering to remove artificial spikes remaining after noise filtering. Histogram shows the distribution for unworn (5.949 μm – 18.579 μm) (a), 3 minutes worn (3.148 μm – 13.323 μm)(b), 15 minutes worn (5.245 μm – 16.483 μm) (c), and 27 min worn sample (4.901 μm – 9.883 μm) (d). Shaded portions in blue are for visualizing the 0.025 and 0.975 probability range. X-axis is height distribution and Y-axis denotes frequency in all of the graphs. 37

Figure 3-8: Schematic to describe the assumption that liquid-air interface does not sag and remains flat, and liquid drop does not follow the surface topography, as it should have otherwise touched the second peak from right. Also shown is how the parameters used in equation (1) and (2) are defined. 38

Figure 3-9: Comparison of contact angles calculated using eq. (1) and (2) with measured contact angles on Sample 27-1. 10% penetration shows a near co-relation with measured CAs for eq. (2). For graphical clarity only two penetration depths (5% and 10%) are shown for eq. (2), while eq. (1) gives CAs of 180° for all penetration depths. Error bars show standard deviation..... 39

Figure 3-10: A representative image showing how, what a drop may see on a topography as, contact line are selected for calculating line contact angles according to eq. (1). The lines are selected randomly on the surface and are one pixel wide..... 40

Figure 3-11: Inset circles show the pixels which will be in contact with the water drop, considering a fixed penetration, but do not contribute towards line parameters as they are less than 5 conjoined pixels. 41

Figure 3-12: Variation of f1 over three horizontal lines 1, 2 and 3 taken on a PTFE sample 27-1. Each line signifies a different position on the same sample, as schematically shown in Figure 3-11. The high deviation between the parameter over different lines on same sample show location dependency of parameters. 43

Figure 3-13: Graph showing f_1 values and comparison considering vertical and horizontal lines on a sample and whole area of the PTFE sample. 43

Figure 3-14: Graph showing f_2 values and comparison considering vertical and horizontal lines on a sample and whole area of the PTFE sample. 44

Figure 3-15: f_l parameter on two powder samples (David). X-axis shows two different samples 4 and 5. Variation between horizontal and vertical line parameter; while 15% penetration is relatively direction immune but area parameter is twice the average of line parameters..... 44

Figure 3-16: Predicted Cassie advancing CAs for PTFE Needle-like geometry surfaces on an area density basis. Equation (1) remains indeterminate for any amount of penetration, while equation (2) is able to predict advancing CA for an unworn surface. 45

Figure 3-17: Cassie CAs on linear density basis as a surface wears down for PTFE surfaces. As can be seen 15% penetration with equation (2) is able to predict CA. 45

Figure 3-18: SEM of Teflon®-Nanoclay spray coated sample. Inset shows a zoomed in view . 46

Figure 3-19: Predicted Cassie CAs on area density basis for different penetration percentages by equation (1) and equation (2) on Teflon®-Nanoclay spray coated sample..... 47

Figure 3-20: Predicted Cassie CAs on linear density basis for different penetration percentages by equation (1) and equation (2) on Teflon®-Nanoclay spray coated sample. 47

Figure 3-21: SEM of wearing PTFE plasma etched sample with glass beads on a gyratory shaker at 250rpm. Unworn surface (a), worn down for 12 minutes (b), 18 minutes (c), and 30 minutes (d). 48

Figure 3-22: Wetting characteristic of plasma etched PTFE sample as it wears down. It can be seen superhydrophobicity is lost after 6 minutes of wearing down..... 49

Figure 3-23: Prediction of CA behaviour with equation (1) and equation (2) for plasma etched PTFE samples. Advancing CA, hence adhesion can be predicted by fitting equation (2). Receding CA cannot be predicted by any of the two equations. Equation (1) remains indeterminate for all values of percentage penetration..... 49

Figure 3-24: Predicting intermediate wetting behaviour of plasma etched PTFE surface by using unworn and long term behaviour characteristics. Advancing CAs are calculated by interpolating f parameter based on values of f at unworn and long term wear. Linear fit between unworn and long term wear is also shown. With respect to interpolation, linear fit is consistently giving good with predicting intermediate advancing CAs. 50

Figure 3-25: Co-relating Wetting and wear of plasma etched PTFE surfaces by comparing the linear fit with 10% penetration CAs predicted by eq. (2). With comparison to eq. (2), linear fit is consistently better at predicting intermediate advancing CAs..... 50

Figure 4-1: Schematic showing the transition of drop from composite state to noncomposite state. Note that the edges of the pillars play an important role for inhibiting the transition..... 53

Figure 4-2: (a) Schematic depiction of the motion of the drop TPCL on a single pillar with increasing the volume: the TPCL is approaching the pillar edge (1), pinned at the pillar edge (2) and after crossing over the pillar edge. (b) Schematic showing drops with constant volume sitting on one single pillar from upright frustum to

inverted frustum geometries. Note that the single pillar can be one of the periodically aligned pillars for the model SHS. 55

Figure 4-3: Illustration of FE analysis for a drop on a single pillar. (a) For drops sitting at the reference position A and an arbitrary position B before crossing over the edge. (b) For drops sitting at the reference point A and an arbitrary position C after crossing over the edge. Note that the apparent CA is defined as the angle between the tangent to the drop at the three-phase contact line and the horizon. If $\Phi = 180°$, the model becomes a flat surface; if $\Phi < 90°$, the model pillar becomes inverse-trapezoidal or re-entrant structure. 58

Figure 4-4: Normalized free energy as a function of the apparent CA on a flat model surface ($\theta_Y = 60º$, $L_A = 4.6\times10^{-5}$ m, $\theta_A = 100º$, $\Phi = 180º$, $V = 2.8\times10^{-4}$ µl)..... 59

Figure 4-5: (a) Schematic showing drops placed on model surfaces with different edge angle Φ (180º, 150º and 120º). (b) Normalized FE curves as a function of the apparent CA for the cases shown in (a) ($\theta_Y = 60º$, $L_A = 4.6\times10^{-5}$m, $\theta_A = 100º$, $\Phi = 120º$, 150º and 180º, $V = 2.8\times10^{-4}$µl)..... 60

Figure 4-6: (a) The normalized FE of a drop sitting on single pillar as a function of apparent CA and edge angle Φ ($\theta_Y = 60º$, $L_A = 4.6\times10^{-5}$m, $\theta_A = 160º$, $V = 0.01$µl). (b) The same FE graph as (a) from another observation direction..... 61

Figure 4-7: A part of FE graph (Figure 4-6) for edge angle Φ ranged from 40° to 60°, which is defined as wetting case 1. ($\theta_Y = 60º$, $L_A = 4.6\times10^{-5}$m, $\theta_A = 160º$, $V = 0.01$µl)..... 62

Figure 4-8: A part of FE graph (Figure 4-6) for edge angle Φ ranged from 60° to 95°, which is defined as wetting case 2 ($\Phi = 60°\sim80°$) and case 3 ($\Phi = 80°\sim95°$). The enlargement is given for edge angle Φ ranged from 70° to 75°. ($\theta_Y = 60º$, $L_A = 4.6\times10^{-5}$ m, $\theta_A = 160º$, $V = 0.01$µl)..... 63

Figure 4-9: A part of FE graph (Figure 4-6) for edge angle Φ ranged from 100 to 150°, which is defined as wetting case 4. ($\theta_Y = 60º$, $L_A = 4.6\times10^{-5}$ m, $\theta_A = 160º$, $V = 0.01$µl)..... 64

Figure 4-10: Wetting graphics for drop with fixed volume ($V = 0.01$µl if $L_A = 4.6\times10^{-5}$ m) on single pillars with the relationship between edge angle (Φ) and intrinsic CA (θ_Y)..... 65

Figure 4-11: (a) Wetting graphics for drop on single pillars with varying drop volume in the relationship between edge angle (Φ) and intrinsic CA (θ_Y). (b) The same wetting graphics as shown in (a), taking $\theta_A = 115°$ as an example..... 66

Figure 5-1: SEM images of the Settings studied, with Setting 5 on the left, Setting 11 in the centre, and Setting 15 on the right, with the images taken from the HU pillars. 3000X magnification for all images..... 71

Figure 5-2: SEM image of a 90° pillar taken from Setting 5. 7000X magnification..... 72

Figure 5-3: SEM image of a 80° pillar taken from Setting 5. 7000X magnification..... 72

Figure 5-4: SEM image of CU pillars from Setting 5. 7000X magnification. 73

Figure 5-5: SEM image of a HU pillar from Setting 5. 7000X magnification. 73

Figure 5-6: SEM image of LSG pillars from Setting 5. 7000X magnification. 74

Figure 5-7: From left to right hexadecane drops on coated silicon, 90° Pillars, 80° Pillars, CU Pillars, HU Pillars, and SG Pillars. All pictures taken for Setting 5. 76

Figure 5-8: From left to right hexadecane drops on coated silicon, 90° Pillars, 80° Pillars, CU Pillars, HU Pillars, and SG Pillars. All pictures taken for Setting 11. 76

Figure 5-9: Representative SEM images from the MSG wafer. The upper left image is from Setting 1, the upper right from Setting 3, the lower left from Setting 5, and the lower right from setting 7, demonstrating the various ways the silicon was etched. 7000X magnification for all images. 77

Figure 5-10: The first study of contact angle behaviour for the studied cases in comparison to increasing surfactant concentration. Mechanical agitation was not intentionally applied. 79

Figure 5-11: The second study of contact angle behaviour for the studied cases in comparison to increasing surfactant concentration. Mechanical agitation was intentionally applied. 79

Figure 5-12: SEM images taken of Case 6 and how the pillars failed to form. The left side is a top down view, while the right side is taken from a 70° angle. 5000X magnification 80

Figure 5-13: Top down SEM image of Case 7 showing how the pillars are linked together. 7000X magnification. 81

Figure 5-14: SEM image of Case 2 taken at a 70° angle. 7000X magnification. 81

Figure 5-15: All textured cases and the contact angle response to increasing surfactant concentration, with the concentrations normalized to the critical micelle concentration of 8mM. 82

Figure 5-16: All smooth cases and the contact angle response to increasing surfactant concentration, with the concentrations normalized to the critical micelle concentration of 8mM. 83

Figure 5-17: SEM images representative of the pillar geometries for the OP wafer. The left side is from Case 1 while the right side is from Case 2. Both images are taken at a 70° angle. 7000X magnification 84

Figure 5-18: Hexadecane drops on the various textured cases of the water, showing their elevated contact angle in comparison to the smooth sections of the surface on the outer portions of the wafer. 85

Figure 5-19: Change in contact angle with surface tension on smooth surfaces. 87

Figure 5-20: Change in contact angle with surface tension on Case 1 of OP wafer. 87

Figure 5-21: Change in contact angle with surface tension on Case 2 of OP wafer. 88

Figure 5-22: Change in contact angle with surface tension on Case 3 of OP wafer. 88

Figure A-1: SEM images of SH coating treated glass samples cured at Room Temperature (21°C) for 17 hours and immersed for 24 hours. 95

Figure A-2: SEM images of SH coating treated glass samples cured at in vacuum at 75°C for 3 hours followed by curing at ambient pressure and room temperature for 14 hours then immersed for 24 hours. 96

Figure A-3: SEM images of SH coating treated glass samples cured at room temperature (21°C) 3 hours followed by curing at ambient pressure and 75°C for 14 hours then immersed for 24 hours. 97

Figure B-1: (a) Comparison of variations of normalized FE with apparent CA for various drop volumes (θ_Y=80°, L_A=0.001m, θ_A=60-160°, Φ=60°). (b) Schematic showing the drop spreading behaviour in wetting case A. 99

Figure B-2: (a) Comparison of variations of normalized FE with apparent CA for various drop volumes (θ_Y=80°, L_A=0.001 m, θ_A=40-160°, Φ=120°). (b) Schematic showing the drop spreading behaviour in wetting case B. 100

Figure B-3: (a) Comparison of variations of normalized FE with apparent CA for various drop volumes (θ_Y=80°, L_A=0.001m, θ_A=40-160°, Φ=85°). The enlarged view of the dashed box is also given. (b) Schematic showing the drop spreading behaviour in wetting case C. 101

List of tables

Table 1-1: The project goals for year two. 1

Table 2-1: Percentages by weight of the different components used in the B21 and B22 variations of the SH coating developed. The only difference between the two is that B22 has a cross-linking agent added to improve durability of the fluorinated sealant. 5

Table 2-2: Contact Angle (CA) measurements for microscope glass slides treated with the 4 different variations of B21 of the SH coating. It can be seen that the 2-coat treatments (2XB21 and 2XB21T) have the lowest CA hysteresis; nonetheless, all treatment variations are SH. 8

Table 2-3: Data comparison between the theoretical and actual component mixing percentages and final coat thicknesses. It can be seen that while there is no significant difference between the amounts of the different components that make up the SH coating, the thickness of B22-B is 63% of what it should be, hence possibly explaining the difference in wetting performance observed for the B22-B samples. 16

Table 2-4: Number of samples per pre-treatment. All plates are then coated with B22T for performance testing. 21

Table 2-5: Summary of advantages and disadvantages of single-mix and layered SH coating spray applications. 24

Table 2-6: This is the caption for the table shown below. 25

Table 2-7: Summary of layered type coating variations with changes in the base/adhesive, roughness and hydrophobic layers. 26

Table 2-8: Summary of advantages and disadvantages of the different adhesives and nano-particles used in creating SH coatings via spray applications. 27

Table 3-1: Threshold values for used for noise filtering. Threshold values vary depending upon the wear time and surface topography. 34

Table 3-2: Penetration percentage depth (in μm) for various samples. 38

Table 3-3: T-test showing that the means of the sample 27-1 are significantly different, owing to the small probability for each set. 46

Table 5-1: Dimensions of Settings studied for the first five wafers and the ideal dimensions, with Setting 5 on the left, Setting 11 in the centre, and Setting 15 on the right. 71

Table 5-2: Contact angle measurements for the 90° pillars with water. 75

Table 5-3: Contact angle measurements for the 80° pillars with water. 75

Table 5-4: Contact angle measurements for the CU pillars with water. 75

Table 5-5: Contact angle measurements for the HU pillars with water. 75

Table 5-6: Contact angle measurements for the LSG pillars with water. 75

Table 5-7: Summary of dynamic CAs for the MSG wafer. 78
Table 5-8: Comparison of desired dimensions and measured dimensions for the SS wafer. 82
Table 5-9: Measured dimensions of the tops of the pillars for the OP wafer. 84
Table 5-10: Dynamic contact angle measurements for three liquids on smooth surface of the OP wafer..... 85
Table 5-11: Dynamic contact angle measurements for three liquids on Case 1 of the OP wafer..... 86
Table 5-12: Dynamic contact angle measurements for three liquids on Case 2 of the OP wafer..... 86
Table 5-13: Dynamic contact angle measurements for three liquids on Case 3 of the OP wafer..... 86

1 Overview

This report covers the activities done in year two as described in Table 1-1. There are four main chapters reporting on each of the topics described in the Table 1-1. Also, the following dissemination of work was done based on the results obtained in the reporting period, and some of the findings from year 1 of this project.

Journal Publication

- D. Barona and A. Amirfazli, "Producing a Superhydrophobic Paper and Altering its Repellency Through Ink-jet Printing," Lab on a Chip, vol. 11, no. 5, p. 936-940, Jan. 2011.

Conference Papers

- D. Barona, A. Amirfazli "A Robust Superhydrophobic Surface for Digital Microfluidics", ASME- ICNMM2011, Jun 19-22, Edmonton, Canada, 2011.

Conference Presentations

- M. Singh, D. Barona, A. Amirfazli, "Wetting Performance of Worn Superhydrophobic Surfaces" ASME Applied Mechanics and Materials Conference, McMAT-2011, Chicago, USA, May 31 to June 2, 2011.
- G. Fang, A. Amirfazli, "Contact Angle Phenomenon at Sharp Edges: A Thermodynamic Approach", 241st ACS Nat. Meeting, Anaheim, USA, Mar. 27-31, 2011.
- D. Barona and A. Amirfazli, "Enabling Lab-on-paper Devices Through Producing a Superhydrophobic Paper and Altering its Wetting Properties Using Ink-jet Printing" SIS 2010, Melbourne, Australia, Nov 14-19, 2010. Invited Talk

Table 1-1: The project goals for year two.

To perform systematic studies to understand the relationship between surface texture and material, with contact angle and contact angle hysteresis. Exploit the developed surfaces in the context of the military, i.e. understanding of durability of surfaces.
To develop fabrication techniques for production of: i. Model surfaces with high liquid repellency (lithographical techniques). ii. Practical surface with high liquid repellency (sprayable coating).
To perform theoretical work for understanding the edge effect (a subset of which includes surface textures with re-entrant geometry). To comprehend the underpinning of omniphobic surfaces, through such theoretical analysis.

2 Sprayable Superhydrophobic Coatings

2.1 Introduction

The information contained in this report summarizes the main activities and achievements of the development, testing and study of sprayable superhydrophobic (SH) surfaces during the past twelve months. The activities for the first year were able to conclude in the successful design and application of a sprayable and versatile SH coating; however, significant progress has been achieved in making such coatings more versatile and durable.

While the coating developed at the conclusion of the first year's activities (referred to as B3) exhibited excellent superhydrophobicity, wetting performance and versatility, it was soon discovered that it was susceptible to both wear and significant degradation (on the order of minutes) from water immersion. The activities of this reporting year have therefore focused on further understanding the different variables that ultimately affect the coating's performance without impacting its versatility. Such variables are: coating component selection, component ratios, spraying techniques and curing methods.

Additionally, maintaining the coatings versatility has allowed for an additional investigation on the use of the SH coating for Lab-on-Chip (LOC) and Lab-on-Paper (LOP) applications by spraying the coating on plain office-grade printer paper. Such an investigation provided additional information on the performance and durability of the SH coating while discovering that the coating's wetting performance can be easily tuned down by printing on it with an ink-jet printer.

The latest developed and tested SH batches (B21 and B22) have maintained the coating's versatility while demonstrating much improved durability under abrasion and prolonged water exposure (via immersion). Treated surfaces can now withstand several hours of wear or water immersion before surface repellency is significantly impacted.

This report briefly summarizes the main activities from the previous reporting period while discussing the change to the different components, spray and curing techniques employed in making the SH coating. The properties and advantages of the latest SH coatings developed compared to previously reported coatings are discussed in the context of durability under various test conditions. Furthermore, the use of the SH coating in the context of microfluidics is also presented along with potential improvements from additional changes to the coating and the way it is applied onto different substrates.

2.2 Brief Summary of Previous Reporting Period

The previous report submitted to DND in the summer of 2010,[86,87] summarized the activities and results for several different tasks as follows:

- Wearing plasma etched PTFE: Started with a complete feasibility investigation along with the full description of the experimental set-up to be used. The observations made and conclusions drawn from such investigation were used to subject various plasma etched

PTFE samples to abrasive wear in order to understand the relationships between a surface's topographical characteristics and its performance under wetting. Several connections were made between some of the surface roughness parameters and the changes in contact angles measured. Although such connections/relationships were clearly demonstrated, it was concluded that additional work needed to be performed in order to fully understand the role of each roughness parameter in a surface's wetting performance.

- Wearing aluminum foil coated with SH coating: Having developed a testing procedure and understanding of how to conduct abrasive experiments on SH surfaces, it was decided that such techniques would be used on wearing aluminum foil samples treated with a SH coating obtained from the University of Illinois. It was determined from this testing that such a sprayable SH coating was more robust than the previously tested plasma etched PTFE samples. It was also concluded that on such a surface, different roughness scales/sizes exist, all contributing towards the durability and wetting performance of such a surface.
- Developing the first batches of SH coating (B1-B3): An in-house version was developed of such SH coating named Batches 1-3 (i.e. B1-B3), with different components concentrations which resulted in different durability and wetting characteristics. Wetting performance was characterized through contact angle measurements of the third coating (B3) for different number of coats and spraying techniques. It was also demonstrated that the coating could be successfully applied to a variety of substrates such as: paper, cotton and polyester/nylon fabrics, metal mesh, composite materials, cardboard and wood.

2.3 Updates and Changes to SH Recipe, Spray Application and Testing Procedures

As part of the ongoing SH coating development work, components, mixture ratios and spray techniques have been varied and optimized such that wetting performance and coating durability are improved. Although the developed coating formulation (B3) had good durability and excellent wetting performance, it was determined that its durability under prolonged exposure to water was significantly impacted. Such results resulted in a complete re-examination of the various components that make up the SH coating

The following sections describe the changes made to the different components that make up the SH coating. Such changes have led to an increasingly more durable and robust sprayable SH coating.

2.3.1 Changes to adhesive and sealant and the addition of Teflon® AF

After developing the first successful SH coating (B3), it was noticed that its performance after prolonged water immersion was degraded in a matter of minutes. Following a quick and purely qualitative examination of the different components when immersed in water, it was determined that the thread-locking adhesive (Permabond MM115 Pure) and fluorinated sealant (Zonyl 8740 – waterborne dispersion of fluorochemical particles) were easily degraded and removed from surfaces after continuous immersion in water.

After researching different adhesives and sealants that were water-proof or water resistant, we decided to replace the previously mentioned components with Gorilla Glue's flagship adhesive (similar chemistry to thread-locking adhesive and advertised as waterproof) and Fluonova's Fluorinated Polyurethane (2k-4FVBA) sealant (fluoropolymers adhesive/sealant for coating applications). After acquiring both components, a qualitative examination of their durability under prolonged water exposure demonstrated that both products were in fact more durable than their predecessors. Additionally, 4FVBA can be used with a polyisocyanate cross-linker that aids in the formation of macro-molecules, which can lead to improved coating strength and durability.

Although the Gorilla Glue and Fluonova products were resistant to prolonged water exposure, they lack the necessary hydrophobic component required to make the coating superhydrophobic. While various trials from B4 to B12 yielded a stronger surface than what could be obtained with B3, a SH coating could not be achieved. It was therefore decided to add a hydrophobizing agent to the coating's mix such that a treated surface could be rendered SH.

Finally, a particular combination of the Gorilla Glue, 4FVBA and Teflon® AF, along with the remaining components (solvent and nanoparticles) yielded a miscible and sprayable coating that could be used to achieve SH surfaces (B13). However, given the different polarities of the different components, in particular the strong polarity of Gorilla Glue (consisting of polyurethane) and the strong non-polarity of Teflon® AF (consisting of fluorocarbons), it was very challenging to achieve a miscible and homogeneous solution. In order to be able to achieve such a solution, a separate investigation was necessary such that an intermediary solvent could be found (described in next section).

2.3.2 Changes to solvent

The original coating formulation contained two solvents: DMSO (mainly a dispersant) and ethanol. These two solvents were originally used to allow for the different components to be mixed and sprayed. However, while ethanol can evaporate very quickly under spray applications, DMSO can get trapped within the various components that make up the mix. It was determined that due to DMSO's hygroscopic nature, if it were to be trapped in the final sprayed film, it can absorb moisture from the surrounding environment, reducing the coating's ability to be able to repel water. Additionally, it was also determined that DMSO could also contribute to the absorption of moisture into the mix while in storage. It was therefore decided that DMSO will not be used as part of the mix and that only a single solvent would be used for particle dispersion and component solubility.

However, given that the mixture without a hydrophobizing agent (i.e. Teflon® AF) was not SH, a new solvent needed to be considered in order to be able to add Teflon® to the mixture. Such a solvent would allow for efficient and improved miscibility and solubility of the different polar and non-polar chemistries that make up the SH coating. After testing different solvents and co-solvents, trifluoroethanol (obtained from Sigma-Aldrich) was identified as a suitable solvent for new SH coating batches containing Teflon® AF. Trifluoroethanol can more readily mix with polar and non-polar components, compared to any of the other solvents tested (i.e. acetone, ethanol, chloroform, toluene, DMSO, FC-75, HFE-7100 and tetrahydrofuran).

2.3.3 Changes to nano-particles

Latest and future variations of SH coatings consider the use of different nanoparticles. The motivation behind changing the Nanomer® nanoclay particles is that they are known to absorb water during prolonged exposure to water. In particular, montmorillonite Nanomer® nanoclay is: known to greatly increase in volume when it absorbs water, resulting in clay to swell several times its original volume 1–6; used as a soil additive to hold soil water in drought prone areas, used to prevent leakage of fluids; used to remove moisture from air and gases; used to absorb and/or clump other fluids. Based on such characteristics of the Nanomer® nanoclay, it has been determined that using different particles, such as SiO_2 nanoparticles, can potentially reduce coating thickness while maximizing coating durability under prolonged water exposure. Section 2.6 discusses the use of alternative nano-particles in more detail.

2.3.4 Final/Current mix and mixing procedure

Following the developments in the SH coating batches as mentioned in section 2.3.1, several additional batches were made (from B13 to B20) in order to achieve an optimized component mixture. The qualitative results obtained from preliminary observations of B21, suggested that a balance between surface wetting and durability had been achieved. The latest developed and studied SH batches, Batch 21 (B21) and Batch 22 (B22), were made following the percentages, by weight, shown in Table 2-1. The only difference between B21 and B22 was that B22 included the cross-linking agent previously mentioned, which was not previously used for any other batch. Additionally, B21 or B22 were not fully tested with alternative nano-particles as later described in section 2.6.

Table 2-1: Percentages by weight of the different components used in the B21 and B22 variations of the SH coating developed. The only difference between the two is that B22 has a cross-linking agent added to improve durability of the fluorinated sealant.

Component	B21 Percentage (by Weight)	B22 Percentage (by Weight)
Nanomer® nanoclay Particles	6.28%	6.16%
Gorilla Glue Adhesive	2.39%	2.34%
Trifluoroethanol Solvent	38.59%	37.88%
4FVBA Fluonova Sealant	29.99%	29.44%
Polyisocyanate Cross Linker	-	1.83%
Teflon® AF	22.75%	22.34%
Total	100%	100%

The various batches of the SH coating have been mixed in a particular and systematic way in order to optimize mixture of the various components shown in Table 2-1. An empty 50ml bottle was cleaned with acetone, dried and weighed for proper tracking and control of all the components as they were mixed. Once the tare weight was noted, solvent and Nanomer®

nanoclay were added to the empty bottle. Both components were shaken together such that the particles were fully dispersed in the trifluoroethanol solvent. At this point, Gorilla Glue adhesive and 4FVBA Fluoropolymer sealant (with or without poly-isocyanate cross linker) were added to the mix since their compatibility in polarity with the trifluoroethanol allowed them to completely dissolve into the solution after shaking. Teflon® AF, being highly non- polar, was added last so that its fluorine atoms could mix well with the trifluoroethanol solvent and the chlorotrifluoroethene, present in the 4FVBA sealant. The final combination of all the components was manually shaken until the solution was of a homogeneous and uniform color and consistency.

Once the components were fully mixed and ready to be sprayed, they were poured into a small bottle that feeds the mix into a pressurized air-brush. This air-brush can be fitted with nozzles of different sizes; however, for the work performed to date, a 0.50mm nozzle was used.

2.3.5 Changes to spray techniques

Since the previous reporting period, different spray variations were implemented in order to achieve different wetting and durability results. The current methodology on different coating applications has become 1 thin coat (B*), 2 thin coats (2XB*), 1 thick coat (B*T) and 2 thick coats (2XB*T). Different coats and coat thicknesses allow for a more comprehensive study of coating durability.

In order to achieve a thin or thick variation of the SH coating films, different parts of the nozzle assembly are either removed or inserted. Figure 2-1 shows the different components of the air-brush nozzle (Aztek A320). The nozzle is assembled with component d) placed into c), c) into b) and b) into a). The subset of c) and d) is defined in this report as the internal pin mechanism. When this mechanism is inserted into the nozzle assembly, it allows for a limited amount of control over spray thickness (actuated by a knob in the spray gun). The turning of the knob pushes on the internal pin to increase its penetration through the nozzle orifice such that the diameter of the opening increases or decreases; removing the internal pin mechanism allows for the spray to flow through a larger and invariable orifice. Spraying without the internal pin mechanism is how the thick ‘B*T’ variations (B*T & 2XB*T) are achieved.

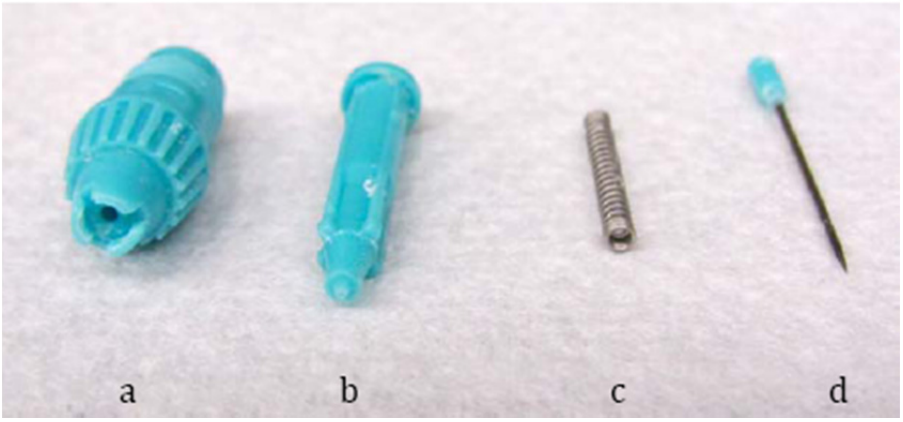

Figure 2-1: Spray gun nozzle components: a) Nozzle; b) Internal pin holder; c) Spring for spray thickness control; d) Pin for spray thickness control. Nozzle assembly with and without c) & d) allows for thin vs. thick sprays.

Four different spray variations were achieved by the inclusion/exclusion of the internal pin mechanism:

1. B*: One coat using 0.50mm air-brush nozzle with internal pin mechanism inserted.

2. B*T: One coat using 0.50mm air-brush nozzle with internal pin mechanism removed.

3. 2XB*: Two coats using 0.50mm air-brush nozzle with internal pin mechanism inserted.

4. 2XB*T: Two coats using 0.50mm air-brush nozzle with internal pin mechanism removed.

Figure 2-2 shows the thicknesses achieved by each of the four different treatments applied. These thickness measurements were made with a micrometer over three different areas of treated 1.0 mm thick microscope glass slides (measured with a micrometer). Microscope glass slides were selected for treatment thickness measurement because of their uniformity (in shape and thickness) when compared to other substrates commonly used in the lab, such as aluminum and composite materials. Since the treatment technique (i.e. handling and spraying) is employed in the same manner for the aluminum and composite material samples, treatment thickness on those (and any other) substrates should be the same. Figure 2-2 also shows that the thickness achieved from spraying one thick layer (B*T) is roughly as thick as two thin layers of material (2XB*). This means that any differences observed in wetting for samples treated with 2XB* and B*T would come from the coating's topography and uniformity rather than from any material thickness/volumetric differences of the sprayed films. Additionally, the measured contact angles for each spray variation are included in Table 2-2 (for B21). Durability information is included in reference.[89]

Table 2-2: Contact Angle (CA) measurements for microscope glass slides treated with the 4 different variations of B21 of the SH coating. It can be seen that the 2-coat treatments (2XB21 and 2XB21T) have the lowest CA hysteresis; nonetheless, all treatment variations are SH.

Treatment	Advancing CA (Deg)	Receding CA (Deg)	CA Hysteresis (Deg)
B21	162.6° ± 3.8°	145.0° ± 10.2°	17.6° ± 10.9°
2XB21	159.5° ± 2.6°	147.5° ± 5.1°	12.0° ± 5.7°
B21T	160.3° ± 2.4°	145.4° ± 4.7°	14.9° ± 5.3°
2XB21T	157.9° ± 3.8°	146.0° ± 9.4°	12.0° ± 10.1°

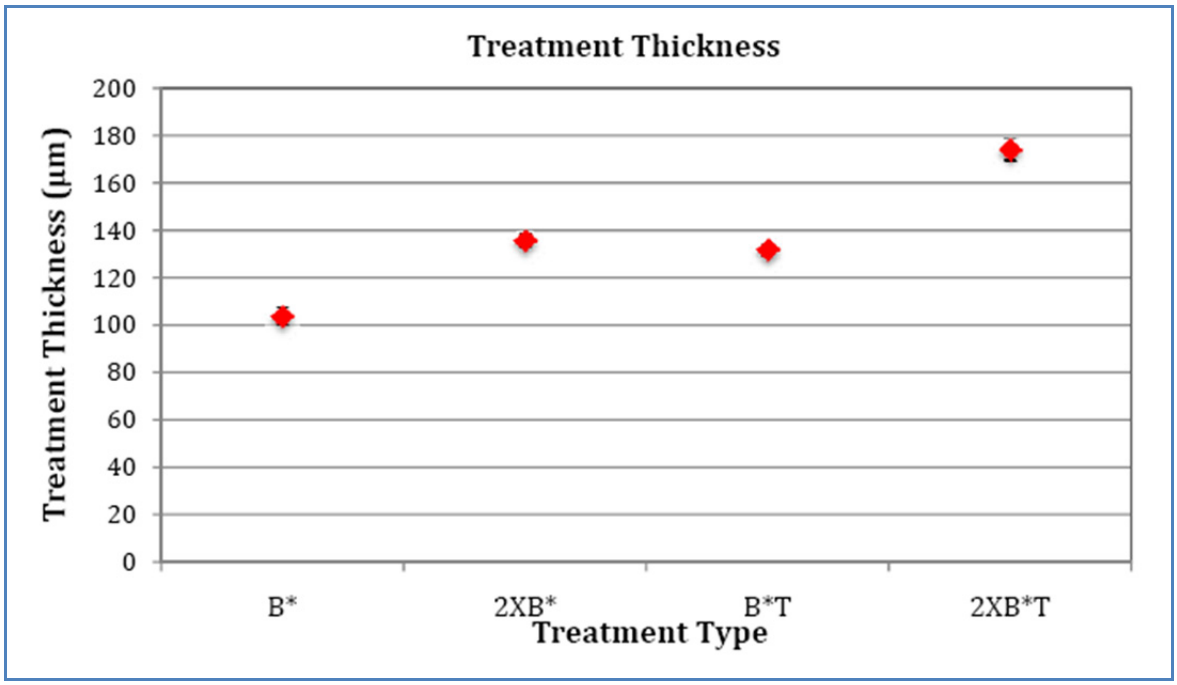

*Figure 2-2: Plot of the different thicknesses achieved by each of the four different treatments, where * corresponds to the respective batch number. Measurements were taken with a micrometer on treated microscope glass slides (compensating for 1.0mm glass thickness). It can be seen that 1 layer of thick treatment (B*T) is roughly the same as 2 layers of thin treatment (2XB*).*

Curing Technique Investigations

2.3.5.1 Introduction and Background Information

Alternate curing methods have been explored since solvents may be trapped within the coating, later to be released while the samples are immersed in water. Solvent entrapment can diminish the coating's performance if it does not evaporate completely from the sprayed films. While most of the solvent is expected to evaporate through the spraying process, some of it can get trapped within the sprayed film and become unable to evaporate. If the solvent does not evaporate from a treated surface, it can change the wetting performance of the surface by absorbing water molecules (due to the solvent's hygroscopic nature). Additionally, exposing a treated surface to water may also release the trapped solvent in a way that damages the sprayed film by changing the film's topography as shown in the SEM images of Figure 2-3. The SEM images show evidence of possible solvent release when the coating is exposed to water as indicated by the presence of pinhole sized tears on the coating's surface.

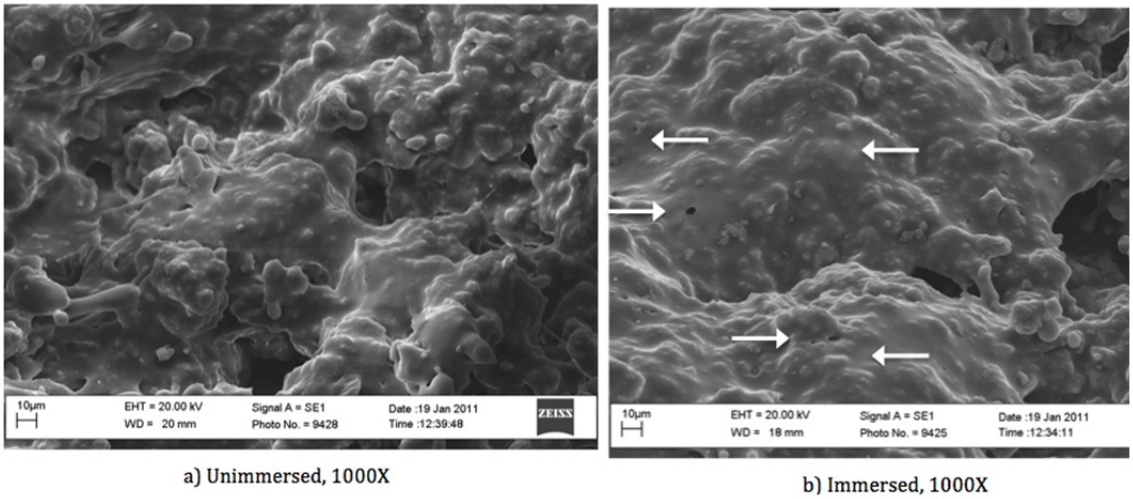

Figure 2-3: 1000X Scanning Electron Microscopy (SEM) Images of Unimmersed (a) and Immersed (b) microscope glass slides treated with 2XB21T. It can be seen that the unimmersed (a) image shows a rougher surface then the smoother immersed (b) image. Also, various pinholes (arrows) are also visible on the immersed image and not on the unimmersed image. The pinholes shown could be evidence of the release of solvent entrapment in the sprayed coating.

Vacuum curing for the current component mixture, as described in the following subsections, has been shown to noticeably increase surface durability for prolonged water immersion tests as shown in the following section of this report. It is believed that solvent and volatile entrapment may be contributing to the measurable decrease in wetting performance after minutes to hours of continuous exposure to (or immersion in) water. The first part of this study focused on investigating the effects on wetting performance after curing under the following three conditions:

- Ambient air pressure at room temperature
- Vacuum (0.1 inHg) at 75˚C

- Ambient air pressure at 75˚C

The second section of this study continued the curing investigation by further exploring curing in vacuum with the following curing scenarios:

- Ambient air pressure at room temperature for 24 hours
- Vacuum (0.1 inHg) at room temperature for 24 hours
- Vacuum (0.1 inHg) at 75˚C for 24 hours

The results from these two separate investigations provide additional information that has been useful towards determining what causes reduction in wetting performance of the SH coating after being immersed in water for prolonged periods of time. Conclusions from this work have been applied to ongoing development and application of the SH coating as developed for further study and improvement.

2.3.5.2 Materials & Methods

During this study, the previously developed B22 SH formulation has been chosen due to its excellent durability and wetting performance (see reference[89]). Table 2-1 contains the component percentages by weight as mixed in the SH formulation; these values come from calculations considering the final desired volume, component densities and component ratios and concentrations. In order to avoid any potential effects from aging of the formulation (solvent evaporation, moisture absorption, etc.), three batches of this formulation (B22-A, B22-B and B22-C) have been made fresh and sprayed immediately onto the samples used in this study. Microscope glass slides have been chosen as the substrate since they are smooth, easy to handle, of homogeneous physical characteristics (i.e. size, shape and thickness) and allow for a much easier visual examination of the applied coating (due to their transparency, it's easier to visually determine the uniformity of the applied coating).

For a comprehensive sample set, a total of 21 microscope glass slides were treated with the B22T variation (one single thick layer of B22 coating) of the SH formulation. This variation was chosen in particular because it provides a good balance between coating thickness and wetting performance (as determined from previous work). Additionally, a one-coat treatment was desired (instead of slightly better performing two-coat treatments) so that the logistics of the coating's age and of the curing process for two coats would not introduce additional variables to the problem. The 21 samples were then divided into the following curing methods, with 3 samples per method allowing us to obtain more consistent and statistically significant data:

Preliminary Temperature and Vacuum Curing combinations (batch B22-A)

- Samples 1-3 cured at room temperature (21˚C) at ambient pressure and at a relative humidity of 14% for a total of 17 hours.
- Samples 4-6 cured in vacuum (0.1 inHg) at 75˚C for 3 hours and then at room temperature for 14 hours for a total curing time of 17 hours.
- Samples 7-9 cured at ambient pressure at 75˚C. The samples first cured at room temperature for 3 hours and then at 75˚C for 14 hours for a total curing time of 17 hours.

Vacuum Curing at Room Temperature (batch B22-B)

- Samples 10-12 cured at room temperature (21˚C) at ambient pressure and at a relative humidity of 14% for a total of 24 hours (control samples).
- Samples 13-15 cured in vacuum (0.1 in Hg) at 21˚C (room temperature) for 24 hours

Vacuum Curing at 75°C (batch B22-C)

- Samples 16-18 cured at room temperature (21˚C) at ambient pressure and at a relative humidity of 14% for a total of 24 hours (control samples).
- Samples 19-21 cured in vacuum (0.1 in Hg) at 75˚C for 24 hours

For the first set of tests (batch B22-A), samples 4-6 (vacuum) and samples 7-9 (temperature, ambient pressure) were staggered due to the fact that we currently have one vacuum oven. Additionally, the different sets of samples were cured as simultaneously as possible so that no effects were induced from aging or premature curing of the sprayed coating. Therefore, samples 4-6 were put in vacuum first so that any trapped solvents/volatiles could be more easily released (prior to any coating hardening). On the other hand, since heat is only supposed to accelerate the curing process (when compared to curing at room temperature), samples 7-9 were allowed to start curing at room temperature, later to be placed in the curing oven (upon removal of samples 4-6). All samples started and finished curing at the same time for a cumulative curing period of 17 hours (from one day's afternoon to the next day's morning).

For the second set of tests (batches B22-B and B22-C), samples under "Vacuum Curing at Room Temperature" were produced from a fresh batch of B22 (B22-B), which was sprayed onto 6 microscope glass slides immediately after mixing. All the samples were sprayed, cured and tested simultaneously to minimize the introduction of additional variables (such as aging, contamination, etc.) into the experiment. Once the testing of these 6 samples was completed (3 curing at ambient pressure and room temperature + 3 curing in vacuum at room temperature), a new and fresh batch of B22 (B22-C) was mixed to produce 6 more samples (3 curing at ambient pressure and room temperature + 3 curing in vacuum at 75˚C) to be tested under identical conditions.

Once the curing process was complete for each of the curing methods, the samples were immediately characterized for wetting performance by taking contact angle (CA) measurements. Each sample underwent advancing and receding CA measurements with a total of ~30 images per sample for a total of ~90 images and ~180 contact angle measurements per curing method.

Following the initial characterization, the samples were partially immersed in deionized (DI) water for a total period of 24 hours (see Figure 2-4). After the immersion period, the samples were removed blown dry with dry nitrogen and characterized again through CA measurements. All the samples were then placed in a dry and dark area at ambient temperature and air pressure for one week before for further testing. A final set of CA measurements was collected from samples 1-9 to determine if there are any changes to the coating with time such as:

- Aging
- Additional or remaining curing

- Additional drying after the immersion period

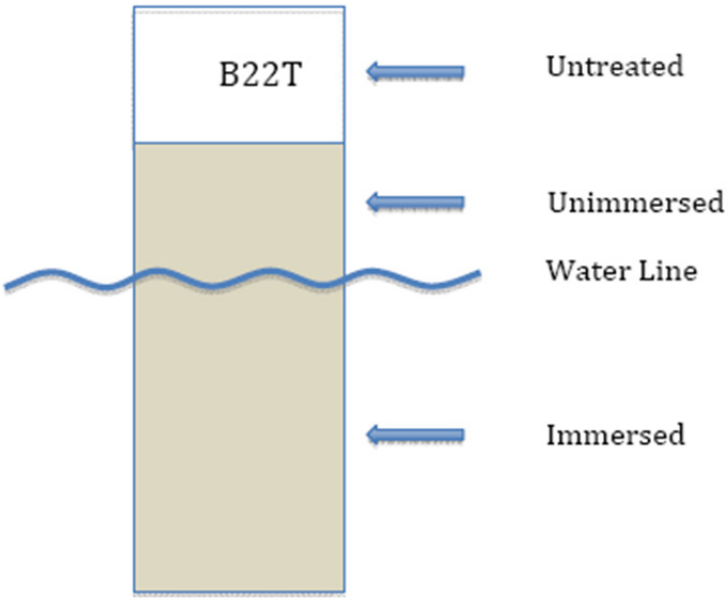

Figure 2-4: Schematic of the treated glass sample showing the relevant portions for the preliminary immersion test performed.

The CA measurements and any observations are discussed in the subsequent sections of this report. Additionally, Scanning Electron Microscopy (SEM) images are included in Annex A for comparison between the different curing methods before and after immersion.

2.3.5.3 Results and Analysis: Part 1 – B22-A

Contact angle measurements were taken for the first 9 treated samples for the following three stages:

- Immediately after curing (and immediately before being immersed).
- Immediately after being immersed.
- One week after being removed from the water and allowed to dry.

The contact angle measurements for these three stages for each of the curing techniques used are plotted in Figure 2-5. Figure 2-5 shows that the samples cured in vacuum have slightly better wetting performance overall when compared to the other two cases as follows:

- Before immersion: slightly higher contact angles, smallest contact angle hysteresis and smallest standard deviation
- After immersion: advancing contact angles remain above 150˚ and receding contact angles remain above 120˚. Both measurements are higher when compared to the other two curing methods.

However, after allowing the samples to fully dry for a period of 1 week, it can be seen from the plots that:

- The wetting performance of the samples cured at room temperature did not change.
- The wetting performance of the samples that cured in vacuum slightly decreased (slight increase in CA hysteresis and its standard deviation).
- The wetting performance of the samples that cured at 75˚C slightly improved (slight decrease in CA hysteresis and its standard deviation).

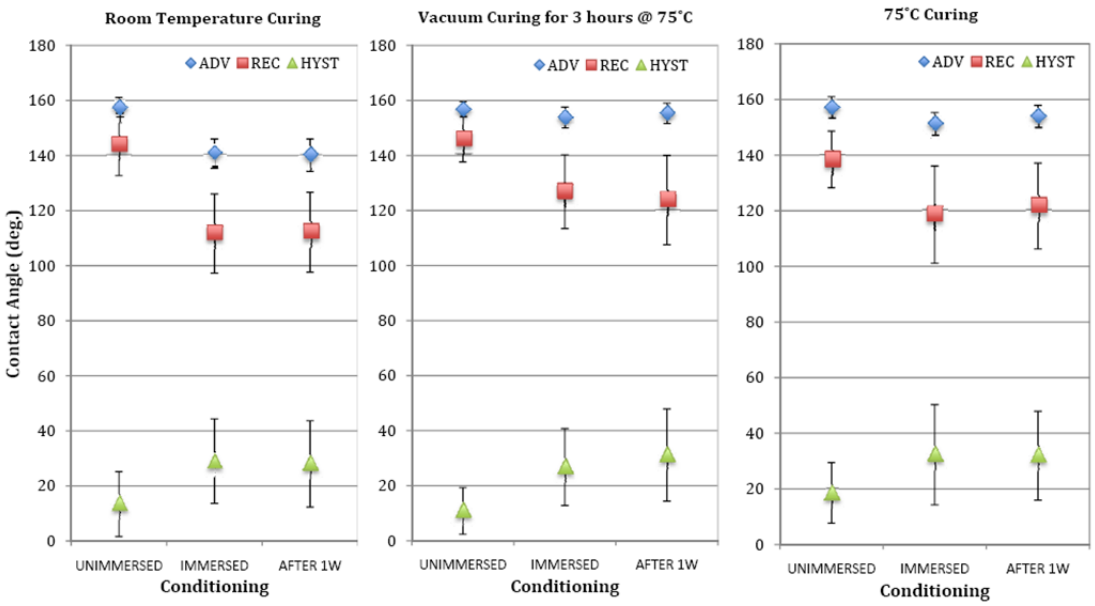

Figure 2-5: Plots of the CA measurements for the first 9 treated samples for each of the curing methods. CA measurements were taken before immersion, after immersion and after 1 week in ambient conditions. It can be seen that the samples that cured in vacuum have the best overall wetting performance with the lowest hysteresis when compared to curing at room temperature or at 75˚C at ambient pressure.

Although the results obtained for the three different curing techniques are not completely conclusive, they do provide additional insight into how different curing methods will have a different impact on the performance of the coating when exposed to the elements. The fact that the wetting performance of the samples cured at room temperature did not change between the removal from immersion and one week later, suggest that at those curing conditions, the samples were able to fully cure in the cumulative 17-hour period. On the other hand, the change in wetting performance after the one-week drying period for the vacuum and temperature cured samples, could suggest that the samples may not have cured completely before immersion in water; for these two curing methods, longer curing times are explored in the second part of this curing investigation in order to allow the coating to properly settle and harden.

Nonetheless, it is apparent from the plotted data that there are some advantages to curing samples in vacuum, which translate into better wetting performance. Whether these advantages are the better evaporation of solvents/volatiles which interfere with (or are susceptible to) the surface's

exposure to water or not, is yet to be conclusively determined. However, it is recommended to proceed with vacuum curing as a better alternative to the temperature-only curing method used to date.

2.3.5.4 Results and Analysis: Part 2 – B22-B & B22-C

Contact angle measurements were taken for the second set of treated samples (samples 10-21) for the following two stages:

- Immediately after curing (and immediately before immersion).
- Immediately after removal from immersion.

The contact angle measurements for these two stages for each of the curing techniques used are plotted in Figure 2-6 and Figure 2-7. Figure 2-6 shows the plots of the contact angle measurements for the control samples of the three different experiments using three different batches of B22 (B22-A, B22-B and B22-C). The control samples were cured at room temperature and underwent the same characterization, curing and immersion/testing processes. On the other hand, Figure 2-7 shows the contact angle measurements for the treated samples under the three different vacuum curing conditions.

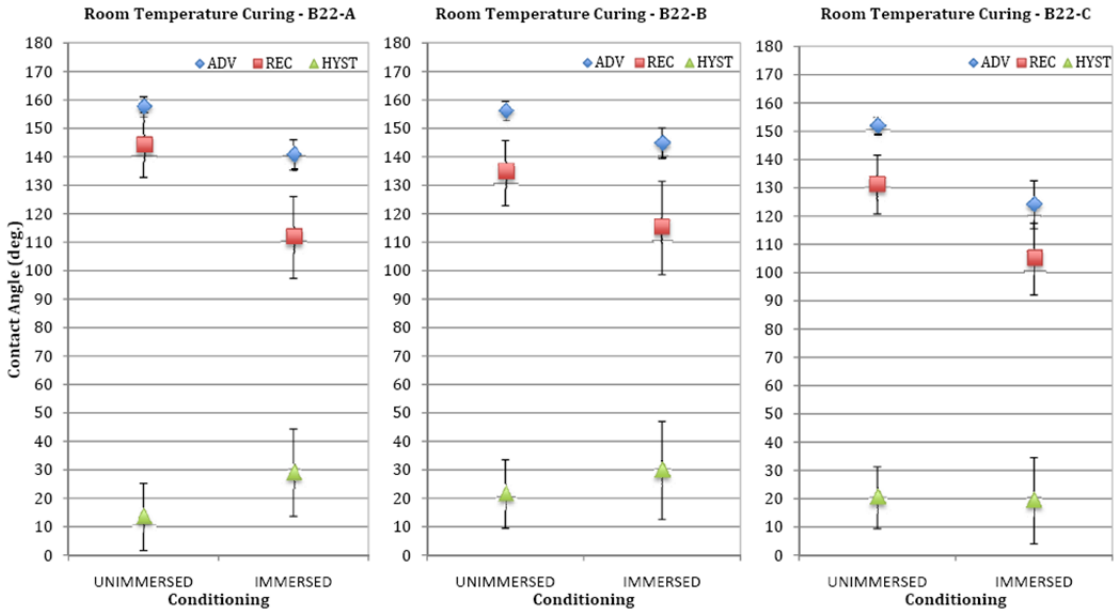

Figure 2-6: CA measurements for the control samples for each of the three separate batches of B22 made. Although the wetting performance is very similar between the three separate B22 batches, some differences are still noticeable and can be attributed to differences in coating thickness and differences in mixing ratios of the components that make up the SH coating.

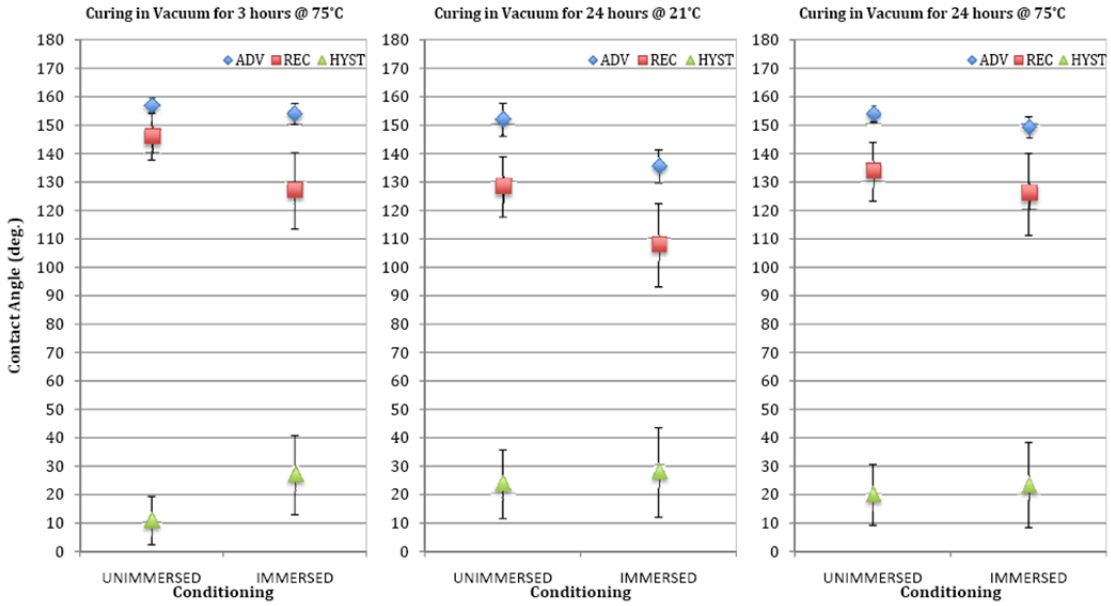

Figure 2-7: CA measurements for the three different vacuum curing scenarios using samples B22-A, B22-B, and B22-C: a) Vacuum for 3 hours at 75°C, b) Vacuum for 24 hours at 21°C and c) Vacuum for 24 hours at 75°C. It can be seen from the plots that curing at vacuum and temperature (a and c) produces a better performing surface than curing in vacuum at room temperature (b).

It can be seen from Figure 2-6 that the wetting performance of the control samples (cured at room temperature) before and after immersion is very similar. However, there are some differences that are easily observed between the wetting results:

- Prior to immersion, B22-A shows the smallest CA hysteresis.
- After immersion, B22-B shows the highest advancing and receding contact angles, but at the same time, an average CA hysteresis of ~30˚.
- After immersion, B22-C shows the smallest CA hysteresis and at the same time, the worst wetting performance.

The only factors that can explain any difference in wetting between the three B22 batches are any differences between the component mixing ratios and the coating thicknesses. In order to better quantify and explain why there are some noticeable differences between the different treated surfaces, the actual component mixing percentages (by weight) and the coating thicknesses have been included in Table 2-3.

Table 2-3: Data comparison between the theoretical and actual component mixing percentages and final coat thicknesses. It can be seen that while there is no significant difference between the amounts of the different components that make up the SH coating, the thickness of B22-B is 63% of what it should be, hence possibly explaining the difference in wetting performance observed for the B22-B samples.

Component	B22 Theoretical Percentage by Weight	B22-A Percentage by Weight	B22-B Percentage by Weight	B22-C Percentage by Weight
Nanomer® Nanoclay Particles	6.16%	6.17%	6.29%	6.12%
Gorilla Glue Adhesive	2.34%	2.33%	2.28%	2.35%
Trifluoroethanol Solvent	37.88%	37.45%	37.44%	38.20%
4FVBA Fluonova Sealant	29.44%	29.25%	28.94%	29.23%
Polyisocyanate Cross Linker	1.83%	2.10%	2.65%	1.92%
Teflon® AF	22.34%	22.70%	22.40%	22.18%
TOTAL	**100%**	**100%**	**100%**	**100%**
Coat Thickness	131.66µm ± 2.64µm	145.20µm ± 19.52 µm	83.18µm ± 5.19µm	132.50µm ± 30.00µm
% thickness wrt. target thickness	**100%**	**110%**	**63%**	**101%**

It can be seen from Table 2-3 that the previously discussed differences in wetting observed, may be explained by the following:

- B22-A has the thickest coat, therefore exposing the least amount of substrate to the water drops. It also has a slightly higher concentration of Teflon® AF, potentially (and noticeably) improving the surface's wetting performance due to its water repelling properties.
- B22-B has the thinnest coat, potentially explaining why, after immersion, the CA hysteresis is ~30˚. However, its advancing and receding contact angles are slightly higher (better) than those from B22-A and B22-C, which could be possibly due to having the highest concentration of cross-linker. A higher concentration of crosslinker would aid in the formation of sealant macromolecules, which make the film stronger and more durable to abrasion and breaking apart.
- B22-C shows the lowest advancing and receding contact angles; however, it also shows the smallest CA hysteresis after immersion. This batch has the least amount of Teflon® AF, Nanoparticles and cross linker while at the same time, having the highest concentration of solvent; such combination of concentrations may explain why B22-C is the worst performer under room temperature curing. Additionally, the fact that it has the smallest CA hysteresis does not necessarily mean that it has better wetting performance; it is the smallest because of having the strongest deterioration in the advancing CA measured, narrowing the gap to the receding CA.

On the other hand, after curing, characterizing and testing the treated samples under the three different curing methods, the following observations can be made from the data plotted in Figure 2-7:

- Prior to immersion, B22-A shows the best wetting performance and smallest CA hysteresis. This can be partially attributed to B22-A being sprayed in the thickest coating. Although difficult to assess how the curing method changes the properties of the surface or of the coating components, B22-A having the smallest CA hysteresis may be also attributed to having a slightly higher concentration of Teflon® AF when compared to the other two batches.
- Prior to and after immersion, B22-B shows the worst wetting performance. This can be mostly attributed to B22-B being sprayed in the thinnest coating (63% of what it should have been). It is unclear on whether or not the additional amount of cross linker has had any impact on the coating's performance under those specific curing conditions.
- Although unimmersed B22-C shows lower advancing and receding contact angles than B22-A, immersed B22-C has the lowest hysteresis of the three batches with similar wetting characteristics to B22-A. Although it has the correct thickness (101% of what it should be), difference in performance may be partially attributed to the lower concentrations of Teflon® AF, Nanoparticles and cross linker.

While there are some minor differences between the ratios of the different components that make up the SH coating, the big picture view of changes to the wetting performance with respect to curing method, is that vacuum curing at 75˚C for a period of at least 3 hours, provides improved durability when compared to samples cured in ambient pressure and room temperature as well as samples cured at ambient pressure and 75˚C.

While this study has also shown that vacuum curing at temperature improves surface durability over standard/ambient conditions, additional factors such as minor differences in component ratios and coating thickness, have been identified as contributors to the ultimate performance of the SH coating when tested. In order to more conclusively point out the specific contributing factors to better coating durability, more precise mixing and spraying of the SH coating would need to be achieved.

2.3.5.5 Summary and Conclusions

This experiment was motivated by the previously observed (and measured) decrease in wetting performance for treated samples that were later immersed in water for minutes to hours at a time. One of the possible causes for this decrease in wetting performance is thought to be the entrapment of solvents/volatiles within the sprayed coating film. It was therefore decided to examine different curing methods which may provide additional insight as to what exactly may be happening to the coating when immersed. The wetting performance for the different curing methods, as determined from the contact angle measurements taken, indicates that vacuum curing is a better option, which generally yields higher advancing and receding contact angles with the smallest contact angle hysteresis. It is thought that vacuum curing may indeed be helping in the final evaporation of any remaining solvents/volatiles from the SH coating which may alter the properties of the coating when in contact with water.

While any additional testing in vacuum curing may not yield any new information on optimizing the handling of the SH coating, it has been determined that component ratios and coating thickness are critical factors when it comes to improving on the durability of SH coatings.

2.3.5.6 Recommendations and Future Work

- Cure treated samples in vacuum at 75˚C for a period of at least 3 hours.
- Analyze and potentially take additional Scanning Electron Microscopy (SEM) images of vacuum cured and immersed samples described in this and other reports.
- Explore surface topography with Confocal Scanning Microscopy (CSM) of immersed and unimmersed samples in order to determine any topographical or morphological changes to the surfaces for the different curing methods.

2.4 SH Coating in Digital Microfluidics: Lab-on-Chip & Lab-on-Paper Applications

After developing the first batches of SH coating and obtaining one that exhibited good wetting properties and reasonable durability (B3), it was decided that such coating would be applied on a variety of surfaces to assess its versatility. One of the surfaces treated with the coating was paper. Mostly out of curiosity, the paper was ran through a printer to determine if a SH paper/surface could be printable. To our surprise, not only did ink droplets adhere to the surface, they also modified the wetting properties of it. This enabled us to study how different levels/intensities/concentrations of ink alter a surface's superhydrophobicity.

The work described in the paper titled "Producing a superhydrophobic paper and altering its repellency through ink-jet printing"[88] conducted a wetting investigation on a SH coated paper printed on with a conventional home-office grade inkjet printer. A specific pattern with varying ink intensities, consisting of control and test areas, was used for assessing the wetting performance of the uniformly coated SH paper printed under different levels of ink applied. The results from this work concluded that: (1) a method for fabricating SH paper had been demonstrated; (2) simple printing technology can be used to manipulate the wetting of SH paper to support the development of LOP devices; (3) for a range of hydrophilic ink intensities (0–85%), water drop mobility can be changed almost independent of repellency; (4) different inks and printing methods yield different rates of change of mobility and repellency with respect to increased ink intensity.

The fact that the repellency and mobility of water drops on SH paper can be altered by printing patterns with a home or office grade printer gives more strength to the argument of using LOP devices for inexpensive sampling, mixing, transport and storage of various liquids. However, it was also determined that exposure of the surface to bulk water for more than ~5 minutes causes irreversible degradation of the performance of this particular superhydrophobic coating.

Based on such published results, along with other observations, it was decided that a more thorough investigation needed to be performed such that the different components that make up the SH coating could be optimized. A successful optimization would yield a more robust, durable

and still versatile SH surface. The details of how and why the different components that make up the SH coating were changed are described in the first subsections of Section 2.3.

After several variations and combinations of the components and component ratios were explored, B21 resulted to be a significantly more robust SH coating to that used in the printable SH paper study. The work and results from testing this new coating were published and presented for the 2011 ASME 9th International Conference on Nanochannels, Microchannels and Minichannels. This work, titled "A Robust Superhydrophobic Surface for Digital Microfluidics",[89] describes the development, testing and advantages of the B21 coating with respect to B3 and in the context of digital microfluidics, such as Lab-On-Chip (LOC) and Lab-On-Paper (LOP) devices. The study concluded that the newly developed SH coating formulation can withstand prolonged periods of wear and exposure to water. The results discussed show considerably improved durability when compared to previously studied coatings which were sensitive to light amounts of abrasion, or exposure to water for ~5 minutes. Even after 240 minutes of abrasive wear and 5.5 hours of immersion in water, the tested samples remain hydrophobic with excellent repellency and good mobility.

2.5 Superhydrophobic Coating Application and Testing Study Plan

2.5.1 Introduction

The information in this section lays out the experimental methods, techniques and materials used to study different application techniques and performance of the previously developed B22, Teflon®-based, superhydrophobic (SH) coating on different substrates.

Other SH coating alternatives such as Fluorinated Polyhedral Oligomeric Silsesquioxanes (FluoroPOSS) and Poly(methyl methacrylate) have not yet been investigated but remain within the scope of SH coating research. It has been previously demonstrated and reported (see section 2.3.6) that Teflon®-based B22 treated samples, which cured in vacuum at 75˚C for at least 3 hours, have better overall wetting performance (after prolonged water immersion) when compared to samples from the same batch cured at ambient pressure and/or reduced temperatures. However, although the coating has previously been applied on different substrates as a demonstration of the versatility/feasibility of application on different materials (i.e. paper, cardboard, wood, fabrics, composite, aluminum, etc.), no significant and quantitative testing has been carried out to properly assess changes in performance from differences in the underlying substrate. In order to properly quantify these differences (and in-line with research goals and future/planned weathering testing done through Defence R&D), the SH coating will be applied to bare and primed mild steel plates.

The coating will be tested after prolonged water immersion (24, 48 and 72 hours) after being applied to:

- Bare steel
- Fluonova primed steel
- Intershield 300 primed steel

- Interzinc 52 primed steel.

Based on the results from this investigation, a better determination can be made on whether or not the SH coating's performance and durability is susceptible to different underlying chemistry. Conclusions from this work will be applied to the future application of the SH coating for improved performance and durability under weathering tests.

2.5.2 Objectives

The objectives of this study plan are to:

- Produce a homogeneous set of samples pre-treated with three different primers.
- Capture any differences in wetting performance from each of the different pre-treatments.
- Determine which pre-treatment may be the best for improved SH coating performance and durability.

2.5.3 Materials and Methods

During this study, the previously developed B22 SH formulation has been chosen due to its excellent mechanical and water immersion durability as well as for its excellent wetting performance. Table 2-1 (see section 2.3.4) contains the desired component percentages by weight as mixed in the SH formulation; these values come from calculations considering the final desired volume, component densities, component ratios and concentrations. In order to avoid any potential effects from aging of the formulation (solvent evaporation, moisture absorption, etc.), a new batch will be made fresh and sprayed immediately onto the samples used in this study. Mild and untreated steel plates (such as those obtained from DRDC Atlantic) will be used as the main substrate since they will later be tested at DRDC Atlantic facilities under different weathering conditions. The samples are smooth and homogeneous, making handling and testing consistent from one plate to the next.

Four different pre-treatments are considered in this study:

No pre-treatment: application directly onto acetone cleaned bare steel. Fluonova 4FVBA: Fluorinated Polyol sealant, currently used as one of the components of the SH coating, provides improved adhesion to a variety of substrates. Primer to be coated while tacky as well as before hard drying (touch/soft dry). Following manufacturer instructions, typical 2 hours for touch/soft dry and 8 hours for hard dry at room temperature. Surface finish while tacky and touch/soft dry is smooth.

Intershield 300: abrasion resistant Aluminum Pure Epoxy currently used by DND for underwater hull coating. Primer to be coated while tacky as well as before hard drying (touch/soft dry). Following manufacturer instructions, typical 3 hours for touch/soft dry and 6 hours for hard dry at room temperature. Surface finish while tacky and touch/soft dry is smooth.

Interzinc 52: corrosion resistant zinc rich epoxy primer currently used by DND for above water hull coating. Primer to be coated while tacky as well as before hard drying (touch/soft dry).

Following manufacturer instructions, typical 75 minutes for touch/soft dry and 4 hours for hard dry at room temperature. Surface finish while tacky and touch/soft dry is smooth.

Two different variations for each pre-treatment are being considered: tacky and touch/soft dry. For the tacky variation, the SH coating will be applied within 60 minutes of applying the pre-treatment/primer. This variation will allow for the SH coating to more directly bond with the pre-treatment/primer, potentially improving overall coating durability. On the other hand, for the touch/soft dry variation, the pre-treatment/primer will be applied to the steel plate and allowed to dry for the manufacturer's prescribed time (after tacky and before hard dry) before being coated with the SH coating. The dry variation will allow the determination of whether the difference in underlying chemistry changes any of the SH coating's adhesion or performance under wetting.

For a comprehensive sample set, each pre-treated plate will be divided into six samples as shown in Figure 2-8 for a total of four plates (one plate per pre-treatment) and 21 samples to be coated simultaneously. Each pre-treatment will be divided into 3 samples (see Table 2-4) to be coated with B22T (one single thick layer of B22 coating). This B22 variation was chosen in particular because it provides a good balance between coating thickness and wetting performance (as determined from previous work). Additionally, a one-coat treatment was desired (as opposed to better performing two-coat treatments) so that the logistics of the coating's age and of the curing process for two coats would not introduce additional variables to the problem.

Table 2-4: Number of samples per pre-treatment. All plates are then coated with B22T for performance testing.

Plate #	Pre-treatment (Primer)	Tacky	Dry
Plate #1	No primer	3 samples	
Plate #2	Fluonova	3 samples	3 samples
Plate #3	Intershield 300	3 samples	3 samples
Plate #4	Interzinc 52	3 samples	3 samples

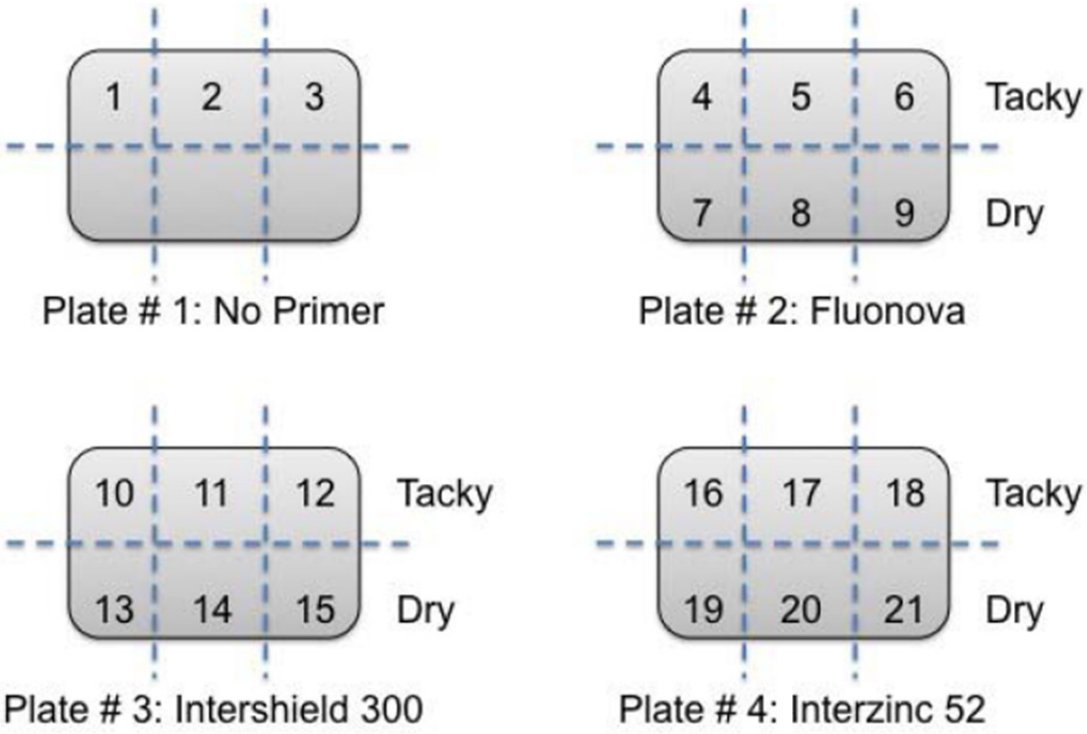

Figure 2-8: Distribution of samples across the different steel plates and different pre-treatments.

The preparation and priming of the bare samples will be staged and scheduled in such a way that all the pre-treated/primed samples are ready for simultaneous SH coating.

Following the simultaneous spraying of the SH coating, the 21 samples will also be simultaneously cured in vacuum (0.1 inHg) at 75˚C for 24 hours. Once the curing process is complete, the samples will be immediately characterized for wetting performance by taking contact angle (CA) and sliding angle (SA) measurements. Each sample will undergo advancing and receding CA measurements with a total of ~30 images per sample for a total of ~90 images and ~180 contact angle measurements per pre-treatment. Additionally, three SA measurements will be taken per sample for a total of 9 SA measurements per pre-treatment.

Following the initial wetting characterization, the samples will be completely immersed in de-ionized (DI) water for a total of 72 hours consisting of 24 hour intervals. After each immersion interval, the samples will be removed, blown dry with dry nitrogen and characterized again through CA and SA measurements. The samples will then be placed in a dry and dark area at ambient temperature and air pressure for any potential follow-up testing.

The CA, SA measurements and any additional observations will be directly compared between the different pre-treatments as well as with data obtained from B22T coated microscope glass slides from a previous study (see section 2.3). In this case, a direct comparison with a previous experiment's data set is legitimate since the handling, preparation and testing methods employed on the SH coating are exactly the same. Such direct comparison of wetting performance between

samples will allow for a better determination on how sensitive or insensitive the developed SH coating is to any differences in the underlying chemistry/substrate.

Depending on the differences in wetting between the different pre-treatments, Scanning Electron Microscopy (SEM) images and/or Confocal Scanning Microscopy (CSM) data might be collected from the samples tested if necessary.

2.6 Current and Future Work: Alternative SH Coatings

2.6.1 Introduction

The information contained in this section of the report summarizes the approach to be taken towards making and testing different superhydrophobic (SH) coatings. The coatings are divided into two groups: single-mix spray and layered spray. The reasoning behind each one of the developed coating types is explained along with its general identified and anticipated advantages and disadvantages. The motivation for this work has come from being able to demonstrate the versatility of spray applications of different components to achieve tailored SH surfaces.

2.6.2 Materials and Methods

The materials and methods used for the single mix coating work described in this section of the report are the same as those reported for batches B21 and B22 in Section 2.3, with the exceptions that: a) Nanomer® nanoclay particles are replaced by SiO_2 and/or PTFE particles and b) the concentrations/ratios of the different adhesive components between themselves are varied without changing the overall component ratios.

The materials and methods used for the layered coating work described in this section are the same as those described in the different subsections of Section 2.3, forming the basis of this work.

2.6.3 Discussion of Proposed Alternative SH Coatings

The coatings to be discussed in this section of the report are divided into two groups:

- Single-mix spray: All the necessary components are mixed into a single batch and sprayed in single step approach. Subsequent layers of the same coating can be sprayed to increase thickness, and in most cases, to improve wetting performance and durability. The mix consists of solvent, adhesives, cross-linker, nano-particles and Teflon® AF.
- Layered spray: The necessary components required to make a surface SH are sprayed separately from each other and in layers. They usually consist of a base/adhesive layer for bonding to the substrate, nano/micro particles layer for surface roughness and a hydrophobic layer (such as Teflon® AF) for maximum water repellency.

Table 2-5 summarizes the general advantages and disadvantages of these two techniques for making SH surfaces. The severity of some of the disadvantages for both coating types can be increased/reduced depending on the components used and the handling given to them and to the spraying equipment.

Table 2-5: Summary of advantages and disadvantages of single-mix and layered SH coating spray applications.

SH Coating Type	Advantages	Disadvantages
Single-Mix	- Single step application. - Single curing process - Can be applied in multiple layers to improve coating uniformity and/or thickness. - Good inter-particle adhesive/boding strength. - Previously shown to have good abrasion resistance	- Can be difficult to mix different component chemistries and polarities. - Improper storage/handling, along with instabilities in the chemistry may cause the mix to separate, react, dry, solidify or absorb moisture. - Sprayed surface roughness is usually higher than layered applications
Layered	- Sprayed surface roughness is usually lower than single-mix applications - Incompatible chemistries/polarities are easier to deal with (or a non-issue). - Storage of different components is more stable than single-mixes, allowing for different components to be fresh prior to any application.	- Multiple step application process - Possibly, multiple step curing process - Cannot be practically applied in multiple layers as each subsequent layer will cover over previous layers; therefore, very high coating uniformity is required for best results. - Previously observed as being less durable under abrasive conditions.

Furthermore, different variations of the single-mix and layered SH coatings are made to further demonstrate how different spray applications can be used to achieve SH surfaces.

The variations to this coating type can come from changing the adhesive components and/or the nano particles used. Table 2-6 shows the different variations for the single-mix type coatings.

Table 2-6: This is the caption for the table shown below.

Coating No.	Adhesive(s)	4FVBA : Crosslinker Concentration	Particles	Description
#1	Gorilla Glue + 4FVBA + Cross-linker (7 : 87.6 : 5.4 by weight)	16:1 (per supplier)	SiO_2	Standard adhesive ratios from B22. This serves as a baseline coating for the single-mix type.
#2	Gorilla Glue + 4FVBA + Cross-linker (7 : 46.5 : 46.5 by weight)	1:1	SiO_2	Increased cross-linker concentration shown to be significantly stronger than the standard concentration. However, final result may still be susceptible to water due to the presence of 4FVBA.
#3	Gorilla Glue + Cross-linker (7 : 93 by weight)	0:1	SiO_2	Cross-linker only adhesive base. Cross-linker has been observed to be very tough. Testing would determine if cross-linker alone can serve as a suitable adhesive base.

It can be seen from Table 2-6 that only SiO_2 particles are used in the single-mix coating variations. The alternative particles are Nanomer® nanoclay or PTFE nanoparticles.

Nanomer® nanoclay particles have been extensively used in the previous batches of the SH coatings being developed. It has been recently argued and reported (see section 2.3.3) that Nanomer® nanoclay absorbs moisture/water, therefore potentially explaining why there is such an evident decrease in performance when a treated sample is exposed to water for a prolonged period of time. Aside from complicating particle dispersion/mixing, PTFE nanoparticles are considered to be impractical for single-mix application because their hydrophobic properties would be coated over by the adhesives and other components of the mix; therefore, PTFE particles would mostly, if not only, contribute to the roughness of the SH coating and not to its hydrophobicity.

The layered type coatings consist of three layers sprayed in immediate succession such that the different layers bond best (the different coating type variations are shown in Table 2-7):

- Base/Adhesive layer: A combination of Gorilla Glue, 4FVBA and/or cross-linker. The concentration of cross-linker is also varied such that different hardness of the cured base layer can be achieved.
- Roughness layer: PTFE or SiO_2 particles (both in the nm range) make up this layer. PTFE particles also provide hydrophobicity, while SiO_2 require to be coated with a hydrophobic component.

- Hydrophobic layer: Teflon® AF is the hydrophobic component used to make SiO_2 treated samples SH. Additionally, a subset of the samples containing PTFE particles (coatings 5, 8, 11 and 14) are coated over with Teflon® AF to protect the base/adhesive layer from direct contact with water. This Teflon® coat can help to better quantify how susceptible the base/adhesive layer is when exposed to water.

Table 2-7 shows the different variations for the layered type coatings where the components for the base/adhesive layer, roughness layer and hydrophobic layer are varied such that SH surfaces can be achieved.

Table 2-7: Summary of layered type coating variations with changes in the base/adhesive, roughness and hydrophobic layers.

Coating No.	Base/Adhesive Layer	Roughness Layer	Hydrophobic Layer	Description
#4	Gorilla Glue	PTFE Particles		Gorilla Glue is used for its hard, tough and water proof characteristics.
#5		PTFE Particles	Teflon® AF	
#6		SiO_2 Particles	Teflon® AF	
#7	4FVBA + Cross-linker (16 : 1 by weight)	PTFE Particles		Standard adhesive ratios used in the B22 coating to serve as the control or reference treatment.
#8		PTFE Particles	Teflon® AF	
#9		SiO_2 Particles	Teflon® AF	
#10	4FVBA + Cross-linker (1:1 by weight)	PTFE Particles		Increased cross-linker concentration shown to be significantly stronger than the standard concentration. However, final result may still be susceptible to water due to the presence of 4FVBA.
#11		PTFE Particles	Teflon® AF	
#12		SiO_2 Particles	Teflon® AF	
#13	Cross-linker only	PTFE Particles		Cross-linker only adhesive base. Cross-linker has been observed to be very tough. Testing would determine if cross-linker alone can serve as a suitable adhesive base.
#14		PTFE Particles	Teflon® AF	
#15		SiO_2 Particles	Teflon® AF	

Table 2-8 shows the advantages and disadvantages of the different adhesives and nanoparticles used to achieve SH surfaces.

Table 2-8: Summary of advantages and disadvantages of the different adhesives and nano-particles used in creating SH coatings via spray applications.

Component	Group Component	Advantages	Disadvantages
Adhesives	Gorilla Glue	- Very strong bonding to most surfaces - Advertised as being a water-proof adhesive - When cured, its consistency is very hard and unaffected by a variety of organic solvents - Very difficult to break or remove from surfaces.	- Highly polar chemistry that makes it difficult to combine with the highly non-polar fluorinated products; therefore, can only be used in small quantities. - Yellow in colour. - Not developed for coating/spray applications
	4FVBA + Cross-linker	- Developed specifically for coating applications - Compatible with a wide variety of polar and non-polar chemistries - Advertised as water repelling and highly durable - Hazy colourless appearance. - Cross-linker concentration can be optimized for best strength and durability	- Observed to somehow degrade when immersed in water - May release trapped solvents with time - Can be removed from surfaces by using organic solvents. - When cured, consistency is 'rubbery' and somewhat flexible (can be hardened by increasing cross-linker concentration). - Increasing cross-linker concentration seems to increase curing time.
	Cross-linker Only	- Clear/colourless appearance - Similar chemistry to that of Gorilla Glue - When cured, its consistency is very hard and unaffected by a variety of organic solvents. - Very difficult to break or remove from surfaces. - Designed for coating/spray applications	- From preliminary testing, it takes longer to dry than 4FVBA or Gorilla Glue - Not yet comprehensively tested (i.e. its susceptibility to prolonged water exposure as well as any chemical incompatibilities are unknown). - Not originally intended/designed to be used by itself

Particles	Nanomer® nanoclay	- Can be easily dispersed in a variety of polar and non-polar solvents - Provides good surface roughness required for superhydrophobicity - Due to particle size, low particle densities can achieve necessary roughness	- Known to absorb water/moisture. - Particles are in the μm range, leading to 'thick' coats when compared to other particles. - Particles are not hydrophobic, requiring them to be coated by a hydrophobic component in order to achieve superhydrophobicity.
	PTFE Nano-particles	- Particle sizes are in the nm range - Particles are inherently hydrophobic because of their chemistry	- Can only be dispersed in non-polar solvents (such as FC-75). - Not suitable for single-mix applications because the particle's chemistry would be coated over by the other components of the mix, hence nulling the hydrophobic chemistry of the particles. Best suited for layered applications. - Particles' chemistry may hinder/complicate mixing with polar components - Due to small particle sizes, higher particle densities (i.e. thicker spray) on coated film may be needed to achieve necessary surface roughness for superhydrophobicity
	SiO_2 Nano-particles	- Particle sizes are in the nm range - Particle chemistry is compatible with a variety of polar and nonpolar components - Can be effectively used in single-mix and layered applications	- Due to small particle sizes, higher particle densities (i.e. thicker spray) on coated film may be needed to achieve necessary surface roughness for superhydrophobicity - Particles are not hydrophobic, requiring them to be coated by a hydrophobic component in order to achieve superhydrophobicity.

Following the treatment of samples with the different single-mix and layered coatings, the samples will be characterized by contact angle (CA) and sliding angle (SA) measurements as well as by the use of Scanning Electron Microscopy (SEM) and/or Confocal Scanning Microscopy

(CSM). Following sample/treatment characterization, the samples will be subject to prolonged water immersion testing (24+ hours) and abrasive testing to properly quantify each treatment's durability as described in previous sections of this report.

2.6.4 Conclusions

Asides from being able to demonstrate the versatility obtained by using spray techniques for creating SH coatings, the results and observations gathered from this study will result in improvements to the ongoing SH coating development. Such improvements will be applied to future work such that more robust and durable single-mix and/or layered SH coatings can be obtained.

2.7 Summary and Conclusions

The activities performed towards the further development of the SH coating for this reporting year can be summarized with the following points:

- The original components that made up the SH coating recipe by the end of the first year's activities were susceptible to prolonged water exposure. An investigation on alternate components has resulted in improved durability under abrasion and water immersion while maintaining coating versatility. Most components were changed and those currently used are: Gorilla Glue (adhesive), Fluonova 4FVBA fluoropolymer + polyisocyanate cross-linker (sealant), trifluoroethanol (solvent) and Teflon® AF (hydrophobic agent). It is believed that Nanomer® nanoclay can also have a negative impact on the coating's durability; it has therefore been proposed that alternative nanoparticles such as PTFE or SiO_2 be used.
- Four different coating variations have been specified: B*, 2XB*, B*T, 2XB*T. Coating thickness and wetting performance is also included in this report. These coating variations allow for a more complete and consistent investigation of the coating's properties under different testing scenarios.
- Curing techniques have been discussed. It has been demonstrated that vacuum curing at 75˚C for at least 3 hours results in better performing SH surfaces.
- The use of the SH coating in microfluidic applications such as Lab-on-Chip and Lab-on-Paper has been discussed. It was determined that the SH coating could be sprayed onto office-grade paper and printed with different ink intensities to achieve different levels of hydrophobicity. The results of such work have been published and presented to the scientific community (see reference[89]).
- Alternate SH have also been identified. In particular, a variation of the single-mix B22 coating has been presented in which Nanomer® nanoclay particles are replaced by SiO_2 particles. Additionally, a set of different layered SH coatings have been proposed for study. The results from such investigation should produce improved durability under surface abrasion and prolonged water immersion.

3 Wetting Performance of Worn Superhydrophobic Surfaces

3.1 Introduction

Superhydrophobic surfaces (surfaces with contact angle greater than 150 deg. and low contact angle hysteresis) are presently an untapped resource; despite various reported wide-ranging applications. Superhydrophobic surfaces (SHS) have not made commercial inroads yet. Some of the applications that stem from self-cleaning nature of these surfaces include: preventing frost from adhering to the surfaces, stain-resistant garments, and frictional drag reduction on boat hulls. The combination of surface chemistry and topography helps in making a surface superhydrophobic. Durability of superhydrophobic surfaces is limited by the fragility of microstructures present on them. Mild mechanical wear on these surfaces results in loss of superhydrophobicity. Abrasive mechanical wear "planarizes" the roughness features on SHS resulting in rise of Contact Angle (CA) hysteresis, Figure 3-1 depicts this loss of superhydrophobicity. The response of researchers until now has been to seek ever more diverse ways of making such surfaces in hope of producing a robust superhydrophobic surface. A more in-depth study of mechanical wear on SHS and ways to minimize it is required in order for them to be used in day-to-day applications. This is the aim of the present research.

Mechanical abrasion has not been quantified on SHS across various papers in literature due to lack of a standard test procedure for SHS. Until now wear has been done by rubbing the specimen against some kind of cloth or sandpaper under a certain load or dropping sand onto a 30˚ tilted SHS from a height. When a SHS is worn down its wetting and surface characteristics change affecting superhydrophobicity. Wetting characteristics of a SHS are defined by advancing and receding CAs. Advancing CA (θ_A) is measured as a liquid drop volume increases and it advances across a surface, while receding CA (θ_R) is when a liquid drop volume shrinks and it recedes across a surface. Advancing contact angle is always larger than or equal to the receding contact angle ($\theta_A < \theta_R$), for the cases known until now.

The difference between the two is called contact angle hysteresis.

Mechanical durability of superhydrophobic surfaces has been the subject of various studies.[7–11] These studies involve imparting superhydrophobicity to the bulk material by use of a fluorinated polymer, when wear happens the polymer coating is abraded away leaving a site of heterogeneity (in terms of differing chemistry and roughness from neighboring material) on the surface. This site of heterogeneity now affects the wetting properties. So combined effects of, change in roughness and surface chemistry, are producing a change in the wetting characteristics. These two components need to be studied separately to gain an in-depth knowledge of the individual effect of each on wetting. Besides these studies,[7-11] the rest remained focused only on wetting characteristics.

It is necessary to systematically and extensively study the surface topography parameters that change during wear on SHS and correlate them to wetting characteristics (advancing and receding CA) to aid in development of durable SHS.

Presently, only the effect of the change in surface roughness on the wetting characteristics is being investigated by using a hydrophobic bulk material. The focus of the present research is finding surface parameters that can predict adhesion and mobility of a drop on a surface, which in turn will help us designing durable superhydrophobic surfaces. In this study, SHS are worn down at fixed intervals and their wetting characteristic and roughness parameters are measured at each wear interval.

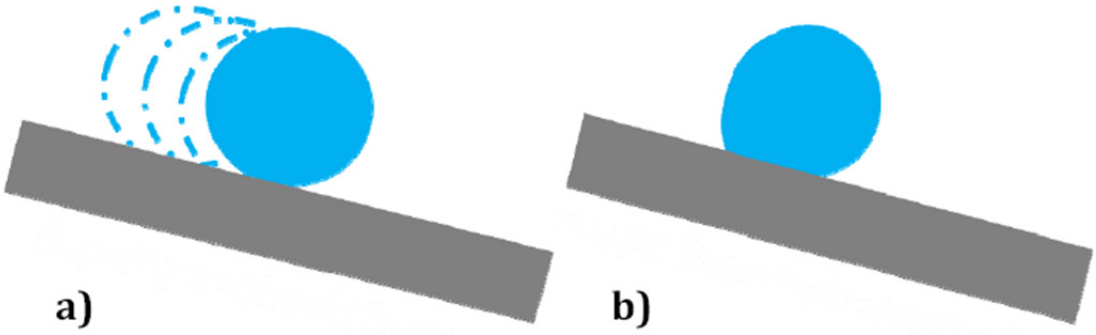

Figure 3-1: Schematic showing how drop is able to roll off easily on undamaged SHS (a), drop is immobile on a damaged SHS (b).

3.2 Experimental Section

Mechanical wear on SHS can induce changes in both surface chemistry and surface topography. To circumvent looking into the changes occurring in surface chemical composition during mechanical wear at this stage, intrinsically hydrophobic polymer Polytetrafluoroethylene (PTFE) is chosen as a subject of present study. This has been a continuation of building on what was started in year one of this project.

PTFE is a low surface energy polymer, whose surface topography can be modified relatively easily with plasma etching to impart superhydrophobicity. Experimental details of the superhydrophobic PTFE surfaces used in this study have been described elsewhere.[12] Superhydrophobic PTFE SHS used in our study contain needle-like structures with random geometry as shown in Figure 3-2.

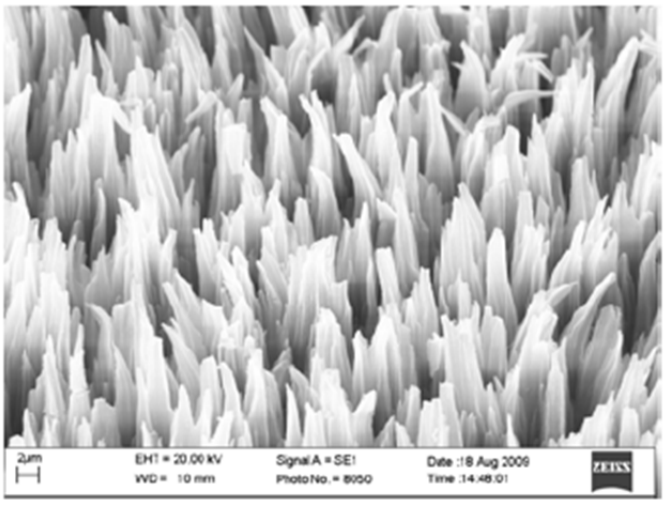

Figure 3-2: SEM of unworn plasma etched Teflon®

Mechanical wear on this surface is done by protocol developed in the previous reporting period.[87] Briefly, the surfaces were abraded using ½ mm glass beads on a gyratory shaker, with experiment designed under standard test similar to specification ASTM F735- 06 (Standard test Method for Abrasion Resistance of Transparent Plastics and Coatings using the Oscillating Sand Method).[13] Samples are placed flat at the bottom of the gyratory shaker while 2L of glass beads, used as abrading material, cover the samples fully. This method of abrasion is repeatable, and one can control wear on a surface, produces little to no contamination of samples, one can choose different abrading materials and importantly it produces random wear pattern. The SHS surface is worn down in varying intervals of three minutes at 250 rpm on a gyratory shaker.

After each wear interval, an abraded SHS was cleaned by ultrasonication in ethanol to get rid of any contaminants on the sample surface. Surface topography and surface descriptors of the samples were then resolved with Carl Zeiss Axio-700 Confocal Scanning Microscope (CSM). A 100x objective with image field of 117 µm x 94 µm and 0.16 µm lateral resolution was used for all the samples. Contact angles were always measured with de-ionised water using the sessile drop method. Water was pumped into the drop at the rate of 0.5 µl/s, and advancing CAs were measured at intervals of one second, as drop volume increased from 20 µL to 60 µL. The reported advancing angle was then an average of the CAs measured every second.

Water was then removed at a rate of 0.5 µL/s from this 60 µL volume water drop until it reached a volume of 20 µL. Receding CAs were measured at intervals of one second. The reported receding CA was an average of the CAs measured at each interval. Surface imaging is done by Scanning Electron Microscope (Carl Zeiss LEO 1430). Before SEM imaging, a gold layer of 10 nm was deposited on the sample surface. Care was taken such that CSM, SEM and CAs were all measured on the same position on the sample; this ensured that the parameters (surface descriptors, wetting characteristics) collected through each measurement (CSM, SEM, and CAs) were correlated and representative of each other.

3.2.1 Noise filtering of the CSM data

In this reporting period, it was found that CSM could not properly resolve edges around steep craters or hills and this tends to create artificial spikes around steep edges. This could be due to light reflectivity issues around the edges. The height profile across an engraving on a coin shows these artefacts in Figure 3-3. These artefacts distort the reality and this extra noise should be removed.

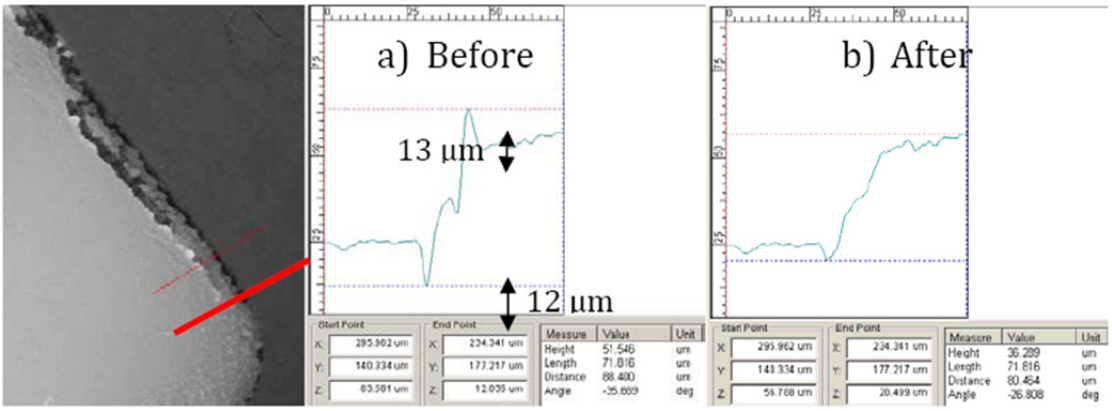

Figure 3-3: a) Artificial spikes created around the edge of an engraving on a coin. b) Same line profile after noise filtering. 20x Objective is used in the imaging.

After some investigation the inbuilt noise cut filter in the CSM software was used. The noise cut filter employs a variation of the pyramid filter. Input given to the filter is a threshold value, which is gradually changed according to the state of the abraded sample.

A visual representation of how this filtering process works is given in Figure 3-4. This filter does not interfere too much with the fine features in a surface while ensuring removal of unrealistic features restoring "normalcy" to the data. For unworn surfaces, no filtering is done as even a small threshold value interferes heavily with data. Sample threshold values for different wear intervals are given in Table 3-1.

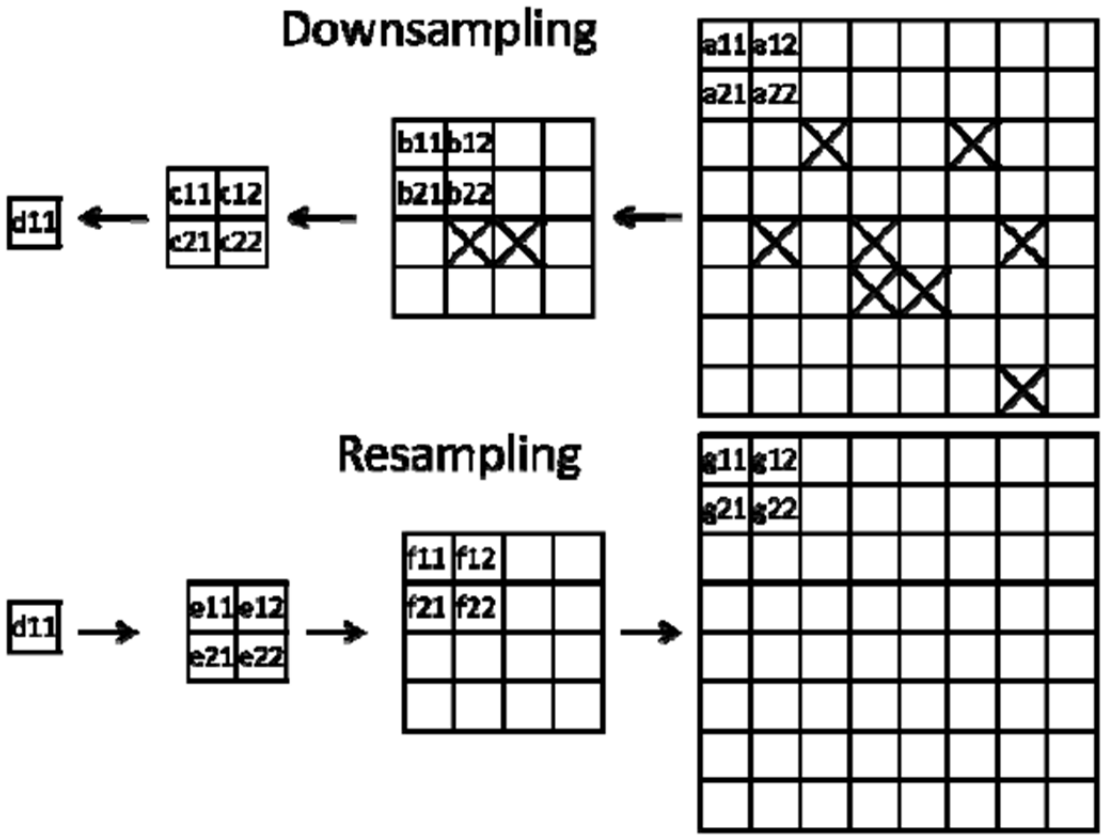

Figure 3-4: Schematic of pyramid algorithm for filtering the noise. Each pixel in image is analyzed for values above threshold and reduced step by step using Gaussian pyramid. Original image is re-created by replacing zero-weight pixels with new pixel values given by pyramid function. This removes artificial spikes created around edges.

Table 3-1: Threshold values for used for noise filtering. Threshold values vary depending upon the wear time and surface topography.

Time (minutes)	Threshold Value for Sample 1	Threshold Value for Sample 2	Threshold Value for Sample 3
0	0	0	0
6	60	60	65
12	65	70	65
18	70	75	75
24	80	85	85
30	85	90	85

The data from year one were revisited in light of SEM observations which resulted in the realization that the CSM imaged PTFE samples contained artefacts which did not correspond to the reality of the physical samples. For example, Figure 3-5 shows the Teflon® sample abraded

for 27 minutes. It was observed that the sample has become flat with relatively few protruding peaks, compared to the unworn surface shown in Figure 3-2. Figure 3-6a shows the CSM taken on the sample worn for 27 minutes; it shows peaks of 10 μm in the sample, which is not representative of the samples considering SEM data which shows a flat surface with the peaks flattened out. This "contamination" of data is considered as noise in the data and was removed by using the noise cut filter option in the software. Figure 3-6b shows the line profile of Figure 3-6a after noise filtering, it is noticeable that fine features are intact and the high peaks have been removed. Some pits were affected too, and are noticeable in Figure 3-6c as a peak of 9 μm height. For each wear interval, thresholding was constrained to a degree such that it was effective in reducing artefacts while shielding fine roughness features on the sample surface from the filter.

Increasing the threshold value to greater than 90 interfered with fine features, affecting roughness features. The remaining artefacts (e.g. peak of 8 μm in Figure 3-6c) were screened by the histogram analysis method detailed below.

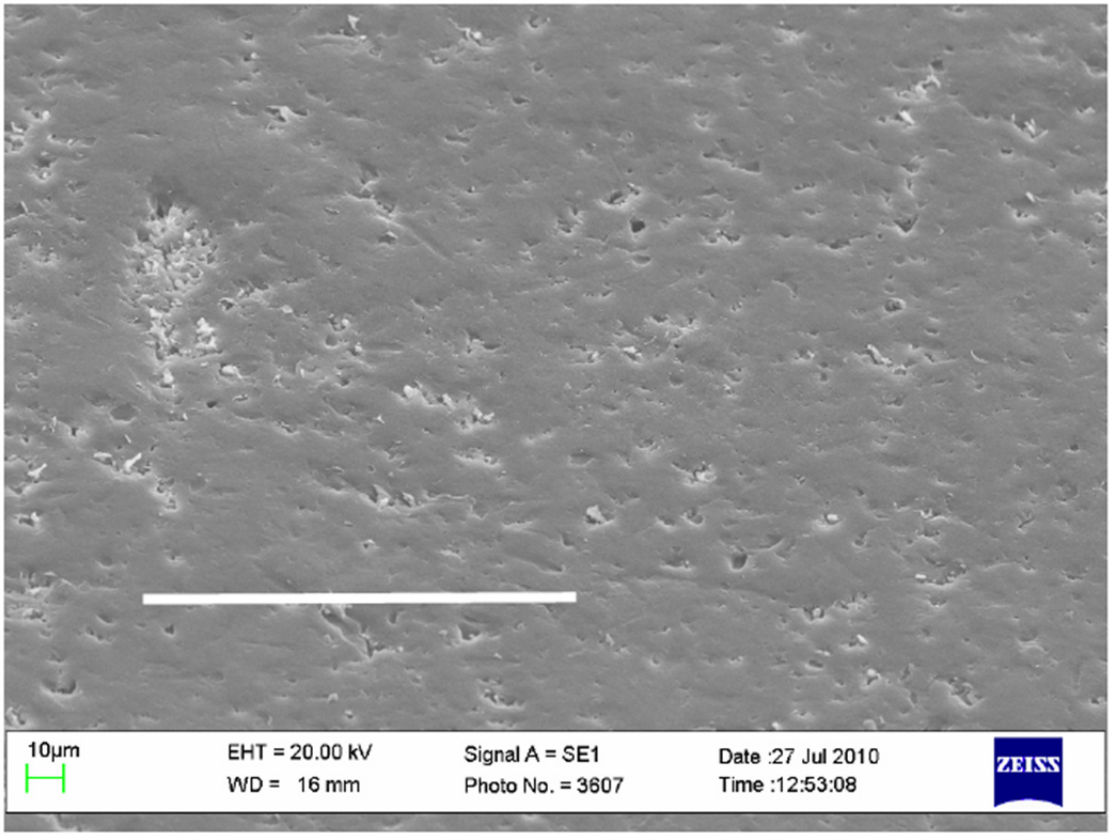

Figure 3-5: SEM of 27 minutes glass beads abraded Teflon® sample. The line on the image is Representative of CSM line profile in Figure 3-6a and b.

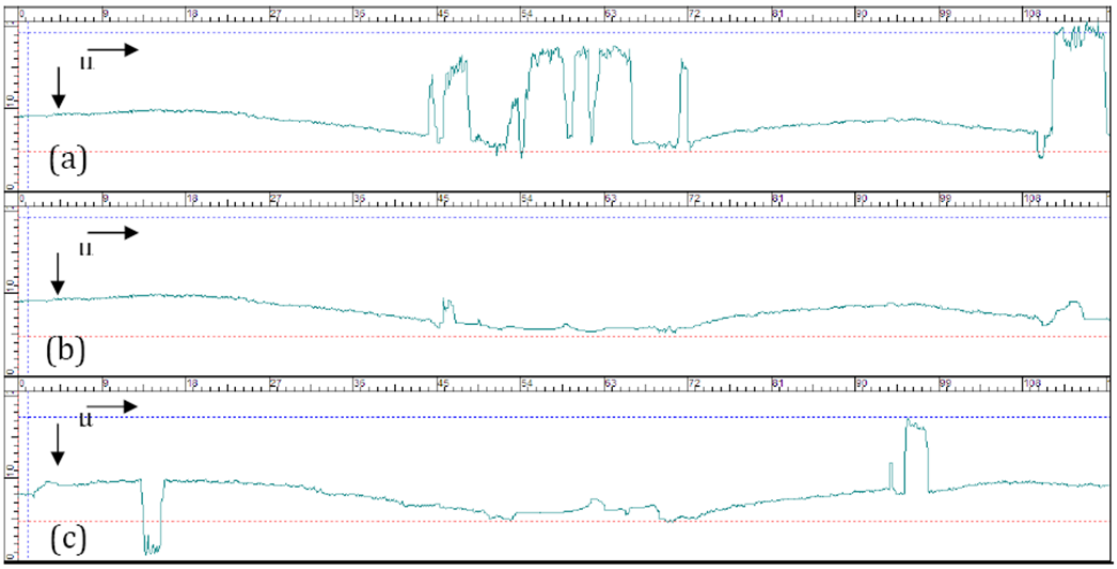

Figure 3-6: (a) Line profile across a sample worn for 27 minutes. Both axes are in μm. (b): Line profile across a CSM data on 27 min abraded Teflon® sample after noise filtering. Both axes are in μm. Notice that only outliers have been affected on by the filter and finer features are intact. (c): Line profile across a CSM data on 27 min abraded Teflon® sample after noise filtering on a different place than one depicted in (a) and (b). Notice a peak not affected by noise filtering. Both axes are in μm.

The height data in the z-image of the samples is stored in a sheet of 1280 x 1024 cells, with each cell containing height at each pixel. This sheet after noise-filtering is exported in Excel format and a cumulative probability distribution function (CDF) plot is plotted from this data using MATLAB program. From this whole distribution height data, values from cumulative probability of 0.025 to 0.975 are considered. The rest of height values falling outside this range are considered to be outliers, as even after noise filtering with pyramid filter the sample worn for 27 minutes contain peaks of 8 μm height, as seen in Figure 3-6c.

The height distribution of an unworn Teflon® sample starts with a normal distribution with a wide distribution of heights. With wearing it became a Chi-square distribution with a right handed tail, and then gradually became a nearly normal distribution again with a narrower base. Figure 3-7 shows the histogram filtering for various wear intervals; the heights before 0.025 and after 0.975 probability were removed from analysis of various parameters. The histogram is a gradation value histogram (height distribution), in which the x-axis shows the height distribution in μm and the y-axis plots the frequency. So filtering was done in two stages; through noise cut and through histogram analysis so that the samples represent, as closely as possible, the sample surface topography.

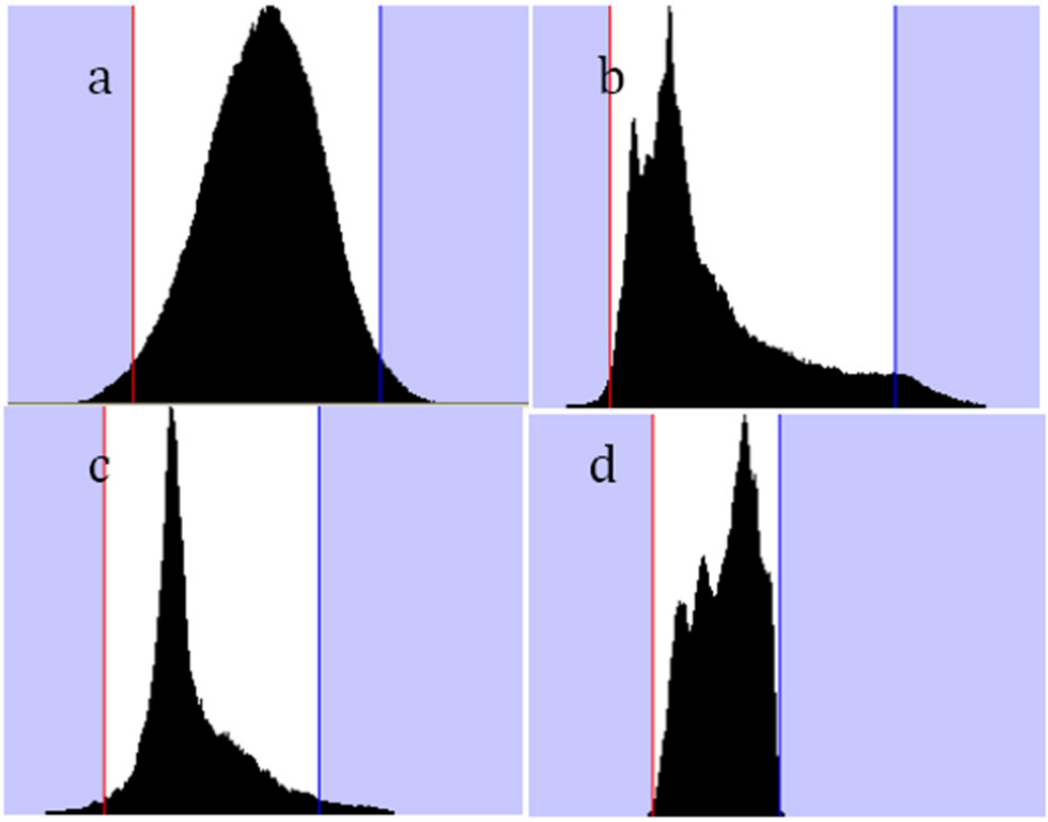

Figure 3-7: Histogram filtering to remove artificial spikes remaining after noise filtering. Histogram shows the distribution for unworn (5.949 µm – 18.579 µm) (a), 3 minutes worn (3.148 µm – 13.323 µm)(b), 15 minutes worn (5.245 µm – 16.483 µm) (c), and 27 min worn sample (4.901 µm – 9.883 µm) (d). Shaded portions in blue are for visualizing the 0.025 and 0.975 probability range. X-axis is height distribution and Y-axis denotes frequency in all of the graphs.

3.2.2 Calculating Cassie contact angles and penetration depths

Various surface topography descriptors can be deduced from CSM data: e.g. average and RMS roughness, skewness, summit density etc. Wetting characteristics can also be calculated from CSM surface topography data and compared with measured advancing CA and receding CA. CAs can be calculated from Cassie's equation given by equation (1); equation (2) is another form of Cassie's equation which has been propagating through literature. Cassie and Baxter defined f_1 as the total area of solid under the drop per unit projected area under the drop, with θ_1 as the contact angle on a smooth surface of material 1. Likewise, f_2 is defined in an analogous way, with material 2 as air. In equation (2), f is defined as the surface area in contact with liquid over total surface area. These equations give predictions for an equilibrium contact angle, which is generally less than the advancing CA and lies between advancing and receding CA's.

$$\cos\theta_c = f_1 \cos\theta_1 - f_2 \quad (1)$$

$$\cos\theta_c = f\cos\theta - (1-f) \quad (2)$$

Equation (1) is as originally defined by Cassie, whereas equation (2) is only valid if liquid does not penetrate the asperities and is only sitting on the top of surface features with flat tops. This latter scenario is not possible for our needle-like structures and penetration is expected for worn and unworn surfaces. Two assumptions while calculating CA's by these two equations are that: (1) the liquid interface does not sag and is flat, between asperities on the surface, and (2) the liquid does not follow the topography. Figure 3-8 demonstrates these assumptions.

To calculate the CA theoretically, various penetration depths are chosen between 5% and 15% of unworn surface height. The absolute values of penetration depths, as shown in Table 3-2, are kept constant and propagated to the entire set of abraded surfaces for finding various f, f_1, and f_2 values on worn down samples. Table 3-2 shows the various percentage penetration depths and their corresponding absolute values on the surfaces. Equation (1) and (2) parameters (f, f_1, and f_2) are calculated at each penetration depth and corresponding CAs are found. Essentially one should do a sensitivity analysis and find a theoretically calculated CA closer to measured CA to estimate penetration depth. In calculation of CAs both the equations are used, and the merit of using equation (2) will be explained later. All such calculation is needed to lay the foundation for understanding the durability of surfaces (wear profile and relation to wettability) so they can be useful for the tough requirements of military applications.

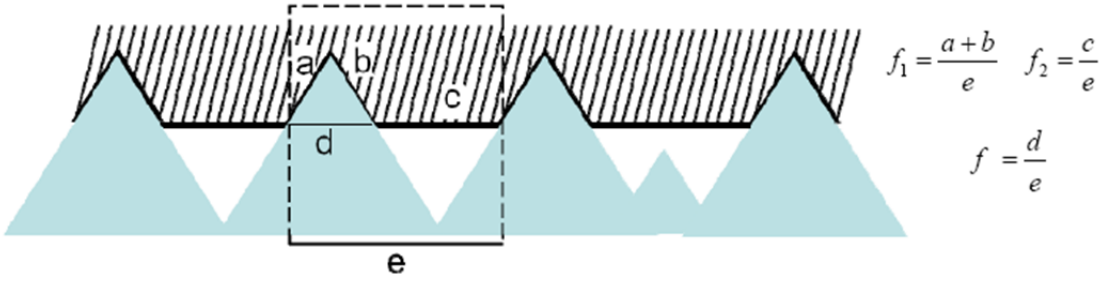

Figure 3-8: Schematic to describe the assumption that liquid-air interface does not sag and remains flat, and liquid drop does not follow the surface topography, as it should have otherwise touched the second peak from right. Also shown is how the parameters used in equation (1) and (2) are defined.

Table 3-2: Penetration percentage depth (in µm) for various samples.

Sample	5% depth (µm)	10% depth (µm)	15% depth(µm)
25	0.6047	1.2094	1.8141
27-1	0.5779	1.1558	2.3116
27-2	0.5565	1.1131	2.2262
29	0.8	1.6	3.18

An intrinsic contact angle of 120° for Teflon® is used in equation (1) and (2). Each assumed liquid penetration depth i.e. 5%, 10%, 15% will give different values of f, f_1, and f_2; these parameters can be computed from the CSM data, as described in Figure 3-8. CSM allows us to map topography and calculate intra-peak distances, height and depth of peaks amongst other things, allowing us to calculate f, f_1, and f_2. Using the equations (1) and (2) one can find contact angles at each wear interval for different penetrations. Comparing these calculated contact angles with measured contact angle gives us the penetration percentage on the sample.

Figure 3-9 shows the calculated contact angles for different penetrations using Equations (1) and (2). It can be seen that using eq. (2), 10% penetration depth broadly agrees with measured advancing contact angles giving us an estimation of penetration theoretically. Similarly for other samples we find the penetration depth which varies from 7% to 12%. It is to be noted here that eq. (1), the original Cassie- Baxter equation, fails to predict CA for any of the depths. Whilst, advancing angles can be predicted by eq. (2), receding angles cannot be. Receding angles are in the range of 90 deg. for wear intervals greater than 9 minutes. The minimum CA predicted by eq. (2) is 120˚, so a new model which is effective in predicting receding CAs is needed. This is a significant finding, as it may point to the fact that we cannot use the current theories to describe the performance of a worn SHS and there is a need to develop new relationships. This will be the focus of the year three for this segment of the project.

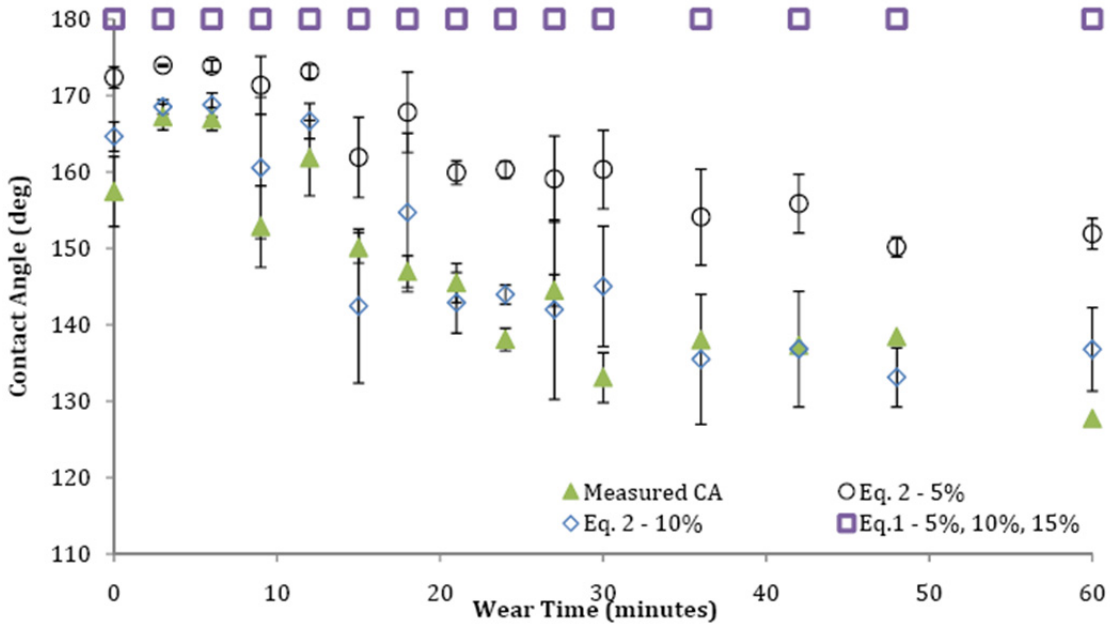

Figure 3-9: Comparison of contact angles calculated using eq. (1) and (2) with measured contact angles on Sample 27-1. 10% penetration shows a near co-relation with measured CAs for eq. (2). For graphical clarity only two penetration depths (5% and 10%) are shown for eq. (2), while eq. (1) gives CAs of 180° for all penetration depths. Error bars show standard deviation.

Before proceeding to develop a new relationship to describe the wetting behaviour of worn SHS, it was thought to test a competing theory put forward by two different scientists, i.e. Extrand, and McCarthy, e.g. [90-92], that proposed that the triple contact line between liquid, solid and vapour

phases influences the contact angle. CAs using contact line parameters, i.e. length of contact line crossing the air (trapped inside the asperities) and solid, should be used instead of traditional surface areas as proposed by the Cassie Eq. (in this case line parameters are used equation (1)). Using parameters on the whole area of the image, or considering horizontal and vertical lines such thinking also fails to give CA values at any penetration depth i.e. only a value of 180° is predicted as the equation is bounded between 120° and 180°. Equation (2) behaves the same way for line parameters as it does for the area parameters, by increasing penetration percentage we can get close to the value of experimental contact angles. As such, the theories of Extrant and McCarthy are not useful for durability studies of SHS. Details of calculating the line parameters are given below for completeness.

On a sample, a line of one pixel width and entire length of an image was chosen as a representation of what a drop may "see" as the contact line on the given topography. The width of this pixel varies according to the objective used; 0.092 μm for 100x objective and 0.9 μm for 20x objective. Lines were analyzed on horizontal and vertical directions spanning the whole image width, as shown in Figure 3-10. Lines at an angle were not possible to draw in the software, as it only calculates roughness parameters for more than 5 conjoined pixels. This is illustrated in Figure 3-11. This is not a hindrance, as both horizontal and vertical lines fail to predict CAs for any value of the percentage penetration depth for equation (1), and penetration depth is mostly more than 5% for equation (2).

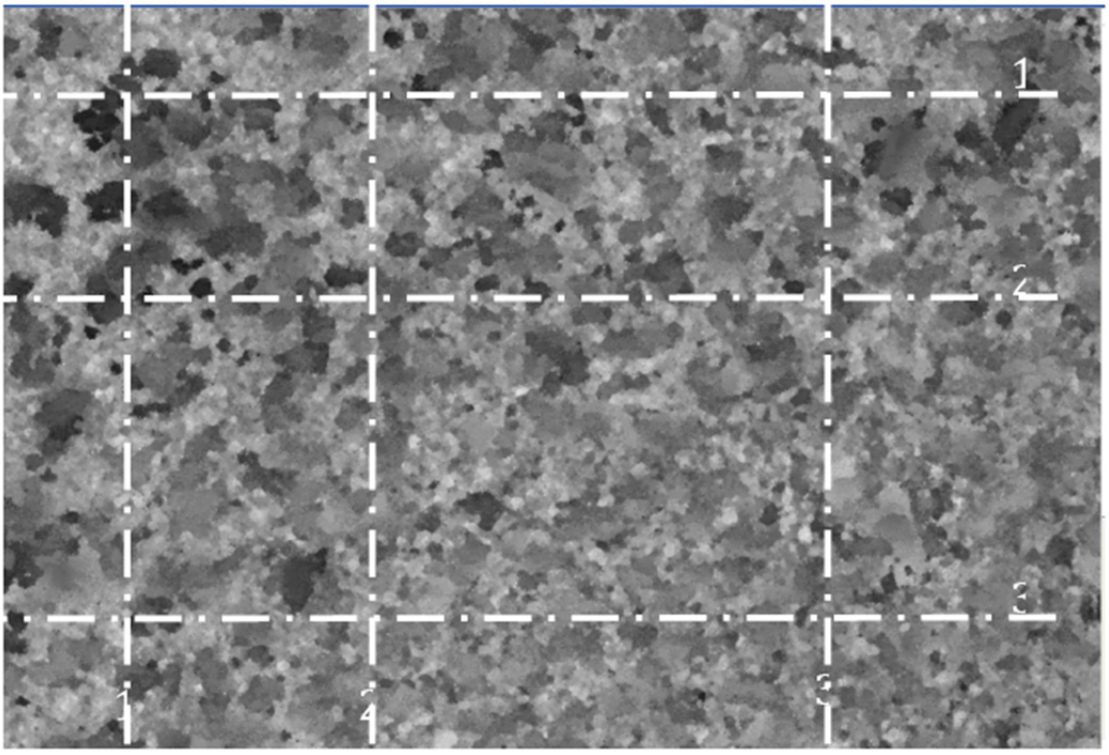

Figure 3-10: A representative image showing how, what a drop may see on a topography as, contact line are selected for calculating line contact angles according to eq. (1). The lines are selected randomly on the surface and are one pixel wide.

Figure 3-11: Inset circles show the pixels which will be in contact with the water drop, considering a fixed penetration, but do not contribute towards line parameters as they are less than 5 conjoined pixels.

On each sample the data from three individual horizontal and vertical lines were used to calculate CAs using equation (1). These three were then averaged to find one individual horizontal and vertical CA for the particular sample. Out of three sets of individual horizontal and vertical CAs (as there are three CSM data sets for one particular wear interval) one individual CA is found for each sample by averaging vertical and horizontal parameters individually; and averaging both of the groups, one combined CA is found.

For this set of data for sample 27-1; 10% and 15% penetration depth CAs on the line basis are calculated; since penetration of 5% produces significant numbers of <5 conjoined pixels. As previously noted, line CAs on the basis of the original Cassie equation (1) cannot be predicted as the *cos (θ)* term is indeterminate for values greater than -1.

Comparing f_1, and f_2 parameters obtained from analysis of vertical and horizontal lines, there is no considerable difference between them and they follow each other nicely except varying at wear time of 6 and 9 minutes as plotted in Figure 3-13 and Figure 3-14. One critical parameter affecting these values is the line selected on the image on which these parameters are calculated, as surface area and areas vary too much across a line profile on a random topography. Figure 3-12 amply proves this point, where the horizontal f_1 parameter is taken across a line on a sample. Individual f_1 parameters are plotted for a line position on a sample, and done so for all three lines. The variation between them is quite large and hence cannot be ignored. Thus these line parameters are location dependent. To find if the line parameters are direction independent, T-tests were done as shown in Table 3-3. It can be seen that they are direction dependent too. The random geometry of the samples is a factor. So horizontal and vertical measurements must be used, but the number of readings must be increased in order to reduce the standard deviation.

To see if the inability of the Cassie equation to properly predict the wetting characteristics of a SHS, is due to the particular case of the Teflon surfaces above, SHS produced by spray techniques in the previous chapter were used. Figure 3-18 depicts the SEM of the topography present on the sample. This random topography presents curved tops and not pointed microstructures and hence is a good alternative to verify equation (1) and equation (2). Contact angles were found by using equation (1) and equation (2) on both area density and line density basis. As can be seen from Fig. 3-19, equation (1) remains indeterminate for various levels of liquid penetration depths into toughs of the surface. As the penetration depth is changed, the *f* parameter changes and hence equation (2) behaves as a "fitting equation" giving Cassie CA

values. On an area and linear density basis, 15% penetration is successful in predicting CAs within a reasonable error range of ±5°.

Hence, equation (1) does not predict advancing CAs and remains indeterminate for random geometries. On the other hand, equation (2) if used as a fitting parameter is successful in predicting CAs for varying liquid penetration levels and can help in predicting the repellency of a drop on a SHS.

3.2.3 Prediction of wetting for worn surfaces

Wearing down a surface changes surface topography, changing wetting characteristics too. Motivation of this research is to predict both advancing and receding CAs as a surface wears down. The wearing down of plasma etched PTFE surfaces is shown in Figure 3-21 (part of the data are from the previous reporting period, but they are processed using the newly developed noise filtering technique in this reporting period). As can be seen, the peaks have flattened out after wearing down for 30 minutes and hence it has lost it superhydrophobicity i.e. ability of a drop to roll off. The wetting characteristics as a surface wears down are shown in Figure 3-22. It can be seen that contact angle hysteresis jumps sharply after a surface has been worn down for 6 minutes indicating that peaks have started to flatten, and hence giving rise to pinning sites for the drop. Cassie CAs are predicted for each interval of wearing down using eq. (1) and eq. (2) on an area density basis as shown in Figure 3-23. Equation (1) returns indeterminate value of CA for all of the wearing down duration. Equation (2) is able to predict advancing CAs at an assumed 10% liquid penetration. Receding CAs will not be predicted by either eq. (1) or eq. (2), as they are bounded between 120° and 180° and receding CAs are on the range of 90°. Hence it is possible to predict repellency (advancing CA) of the drop with help of eq. (2), but predicting mobility (receding CA) still remains elusive as shown in Figure 3-23.

Seeing as how eq. (2) is successful in predicting advancing CAs, the question was asked, can intermediate advancing CAs be predicted based on a function of characteristics of unworn and long term worn down surface? It was decided to see if a correlation can be found on the basis of interpolating either f values or simply doing a linear fit between advancing CAs, shown in Figure 3-24. Interpolating f values gives results with a large CA error. Error ratio for predicting CAs ±3°, is 60%; linear fit is successful in predicting CAs, 70% of the time. Based on this, linear fit is a viable method which can be used for predicting intermediate advancing CAs, simply based upon advancing CAs of unworn and long-time worn down surface. This brings up a question about whether eq. (2), has been rendered redundant by this simple linear fitting of two end points of wetting behaviour? Figure 3-25 shows the comparison between advancing CAs predicted by eq. (2) and linear fit between two end points. It can be clearly seen that linear fit has more probability of predicting CAs close to the measured CAs than by using eq. (2). This is valid for all other data sets of the same sample. Hence, tentatively, it is concluded that just by having wetting characteristic at unworn plasma etched PTFE surface and long-time worn down surface, one may predict repellency of the drop (advancing CAs) at any intermediate wear time within reasonable error limits of the CA. It is noted that this is somewhat of a naive correlation, and as mentioned above further investigation is needed.

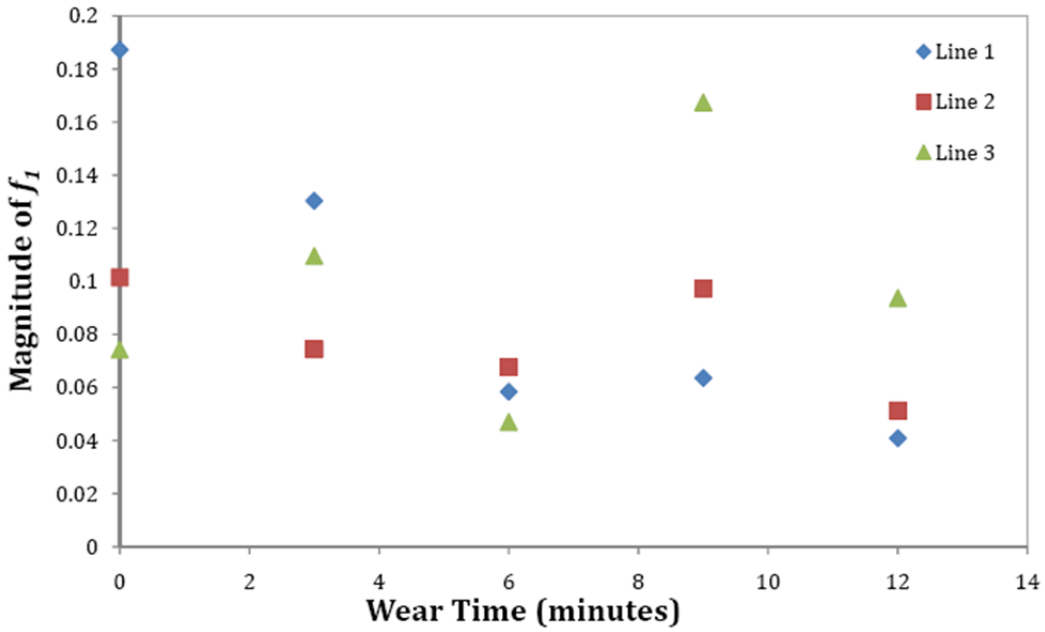

Figure 3-12: Variation of f1 over three horizontal lines 1, 2 and 3 taken on a PTFE sample 27-1. Each line signifies a different position on the same sample, as schematically shown in Figure 3-11. The high deviation between the parameter over different lines on same sample show location dependency of parameters.

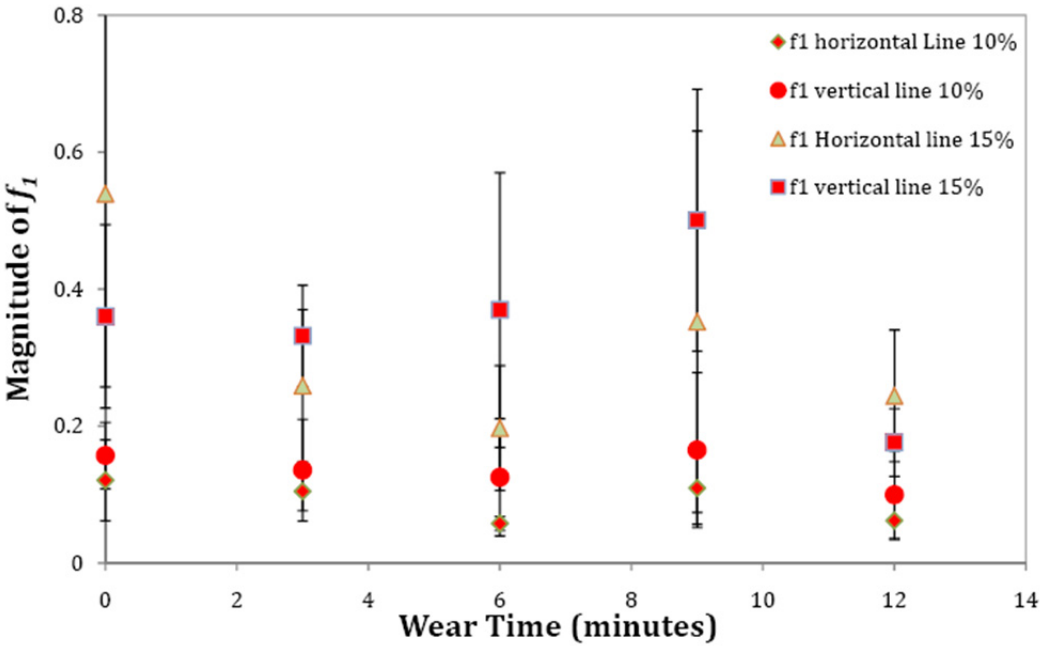

Figure 3-13: Graph showing f_1 values and comparison considering vertical and horizontal lines on a sample and whole area of the PTFE sample.

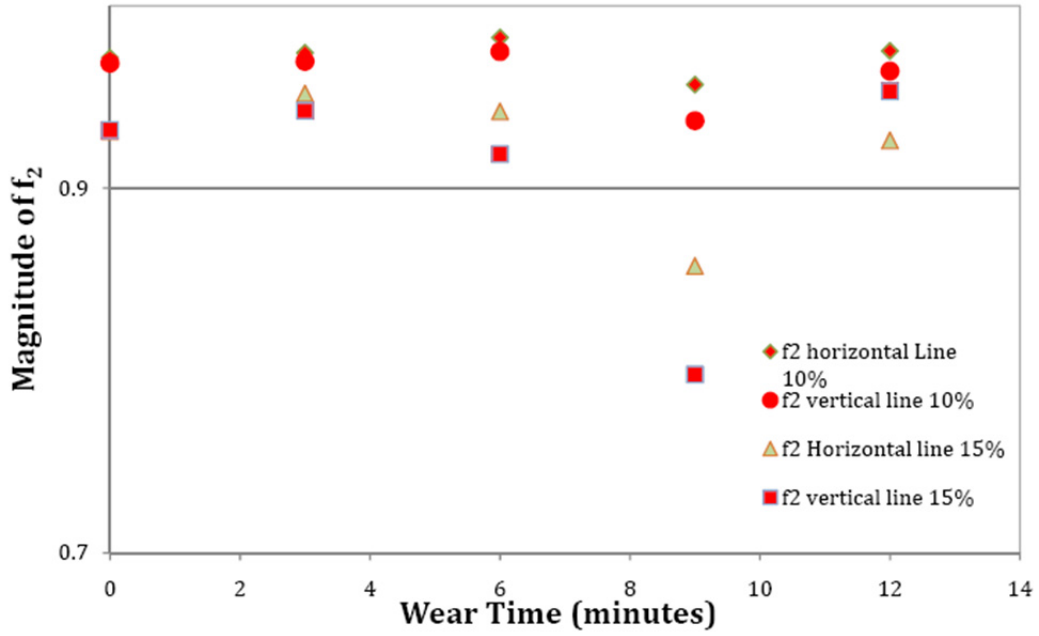

Figure 3-14: Graph showing f_2 values and comparison considering vertical and horizontal lines on a sample and whole area of the PTFE sample.

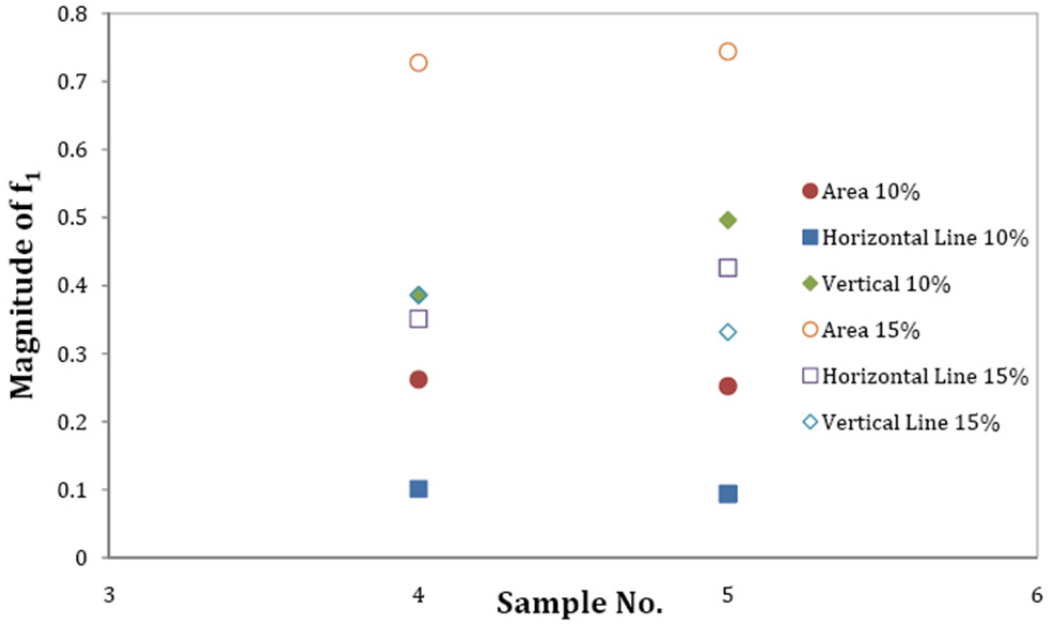

Figure 3-15: f_1 parameter on two powder samples (David). X-axis shows two different samples 4 and 5. Variation between horizontal and vertical line parameter; while 15% penetration is relatively direction immune but area parameter is twice the average of line parameters..

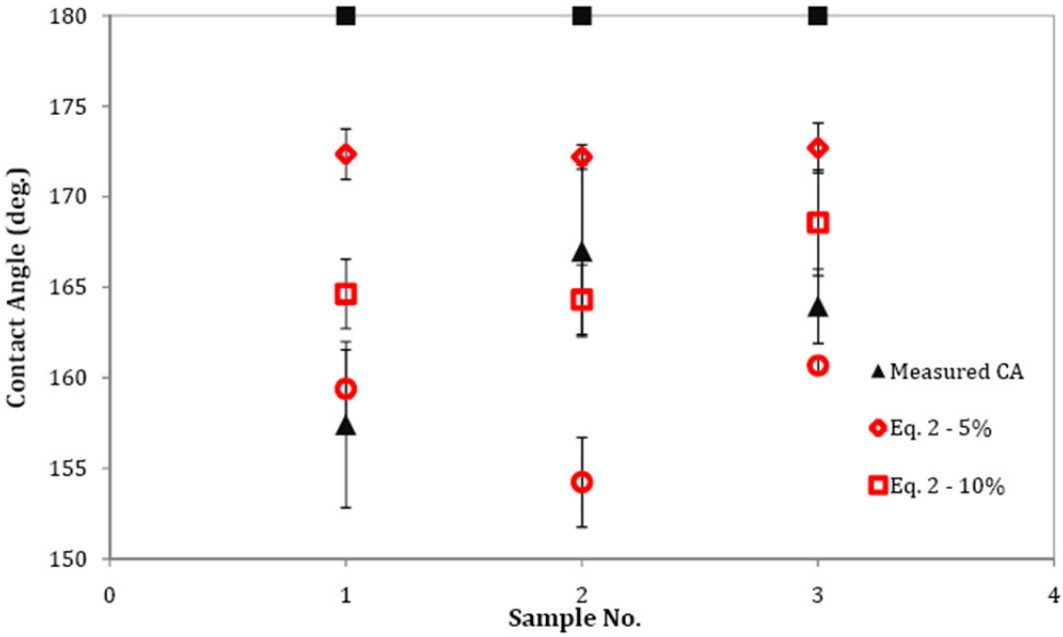

Figure 3-16: Predicted Cassie advancing CAs for PTFE Needle-like geometry surfaces on an area density basis. Equation (1) remains indeterminate for any amount of penetration, while equation (2) is able to predict advancing CA for an unworn surface.

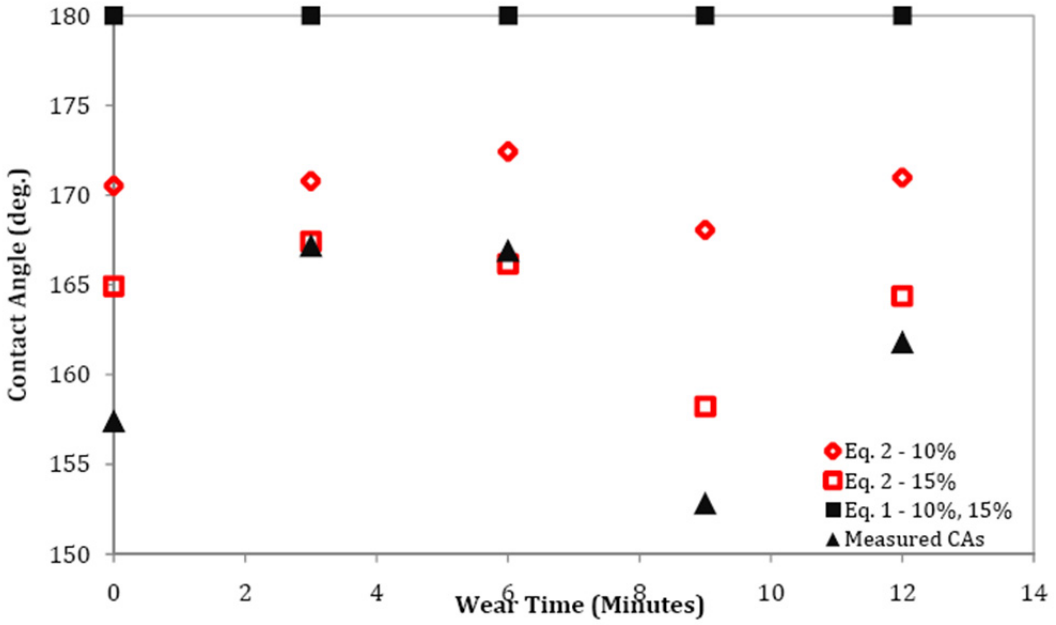

Figure 3-17: Cassie CAs on linear density basis as a surface wears down for PTFE surfaces. As can be seen 15% penetration with equation (2) is able to predict CA.

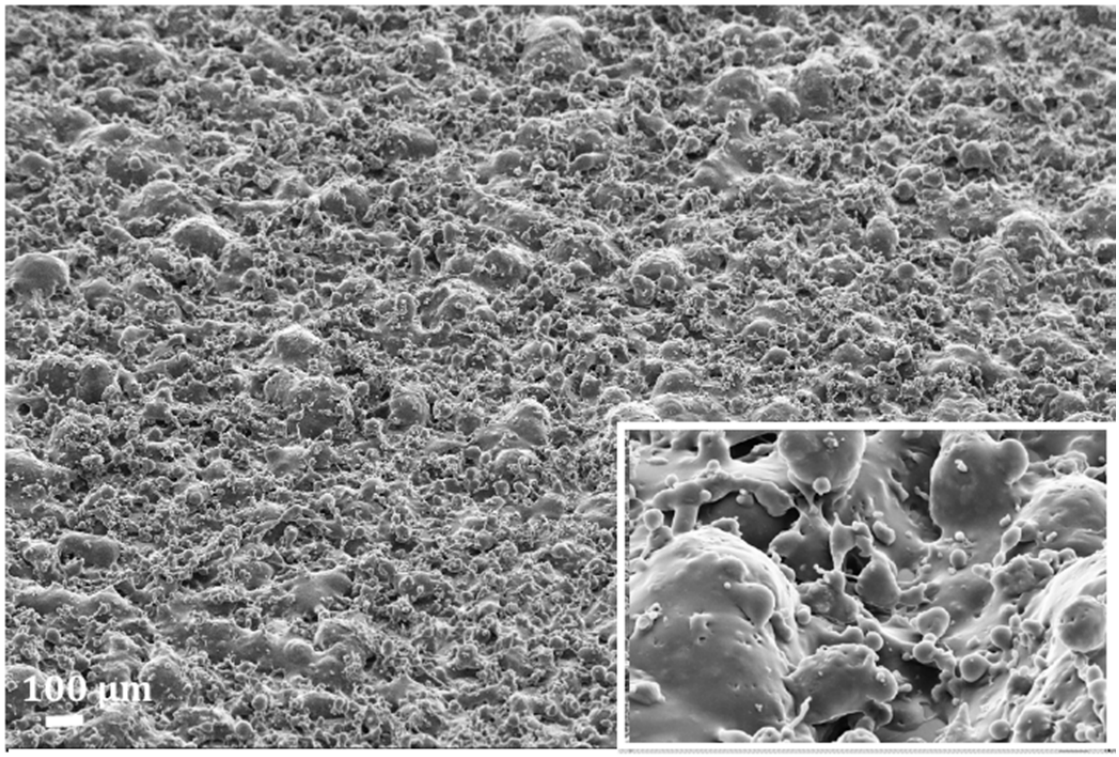

Figure 3-18: SEM of Teflon®-Nanoclay spray coated sample. Inset shows a zoomed in view

Table 3-3: T-test showing that the means of the sample 27-1 are significantly different, owing to the small probability for each set.

Sample	f_1 - horizontal	f_1 - vertical	T-test probability of result	f_2 – horizontal	f_2- vertical	T-test probability of result
Unworn	0.1872	0.1717	0.46	0.9570	0.9657	0.75
	0.1015	0.1967		0.9753	0.9631	
	0.0742	0.1030		0.9823	0.9768	
3 mins	0.1303	0.2085	0.54	0.9628	0.9467	0.75
	0.0744	0.1386		0.9865	0.9725	
	0.1095	0.0601		0.9734	0.9892	
6 mins	0.0584	0.2220	0.24	0.9833	0.9668	0.34
	0.0677	0.0602		0.9862	0.9882	
	0.0470	0.0938		0.9781	0.9696	
9 mins	0.0636	0.0690	0.48	0.9794	0.9761	0.54
	0.0972	0.1365		0.9682	0.9412	
	0.1674	0.2897		0.9226	0.8935	

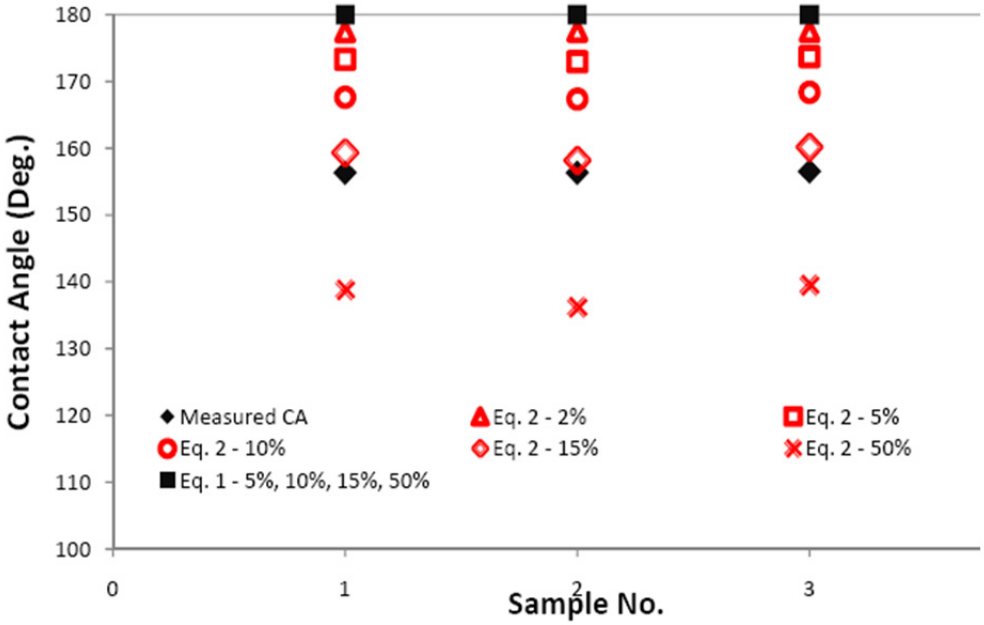

Figure 3-19: Predicted Cassie CAs on area density basis for different penetration percentages by equation (1) and equation (2) on Teflon®-Nanoclay spray coated sample.

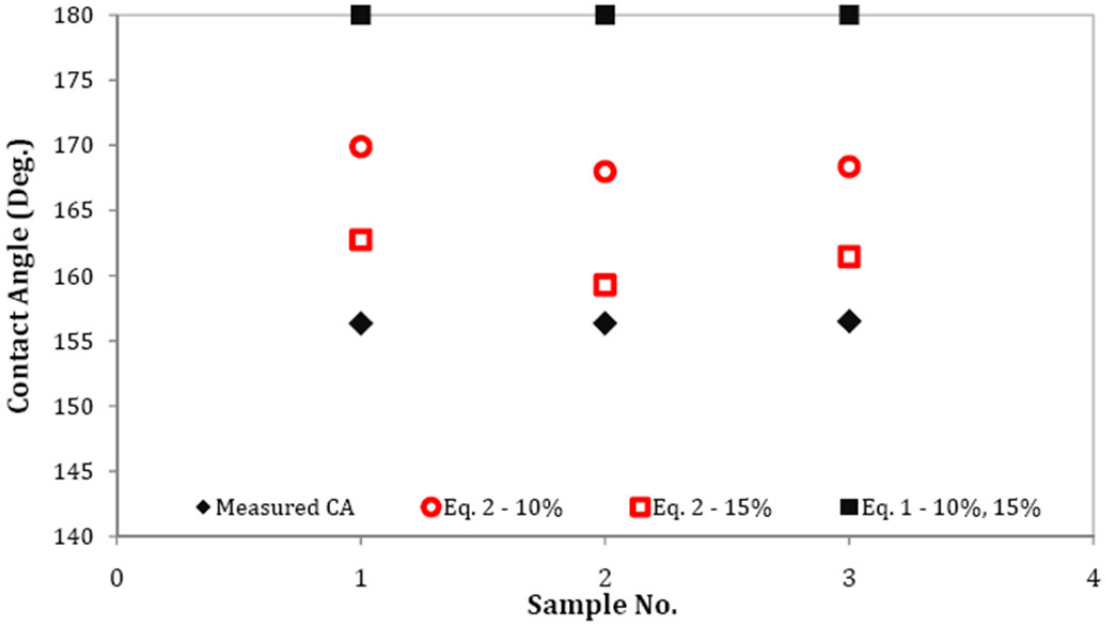

Figure 3-20: Predicted Cassie CAs on linear density basis for different penetration percentages by equation (1) and equation (2) on Teflon®-Nanoclay spray coated sample.

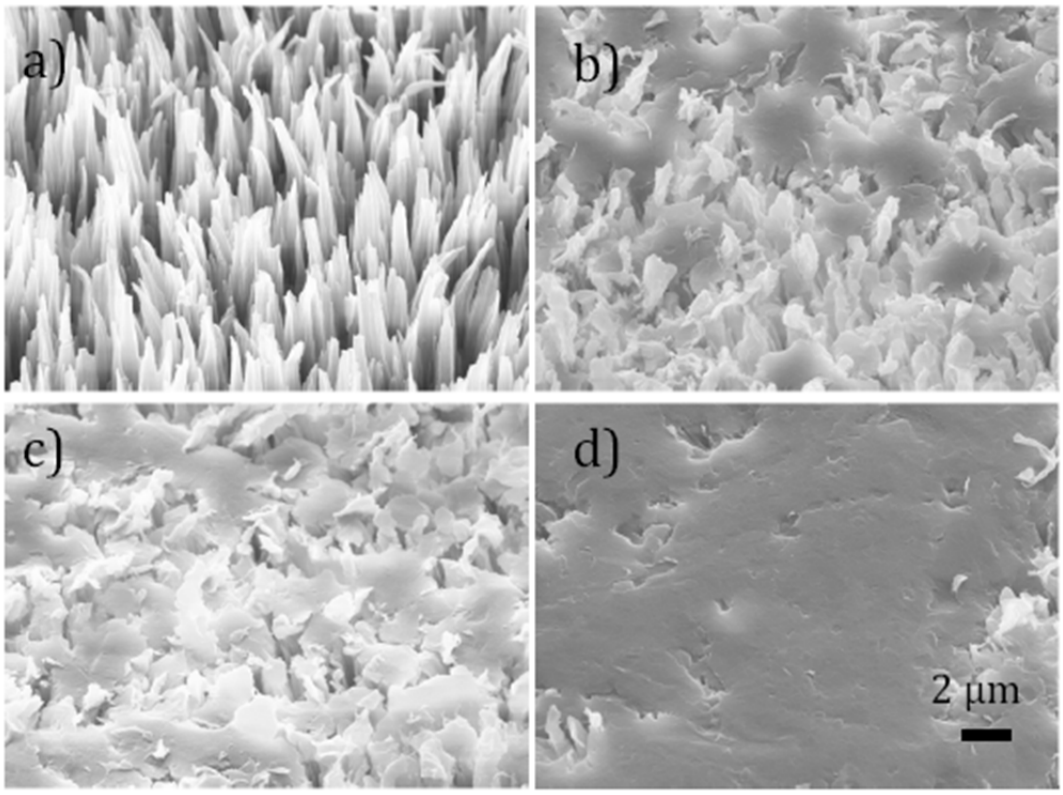

Figure 3-21: SEM of wearing PTFE plasma etched sample with glass beads on a gyratory shaker at 250rpm. Unworn surface (a), worn down for 12 minutes (b), 18 minutes (c), and 30 minutes (d).

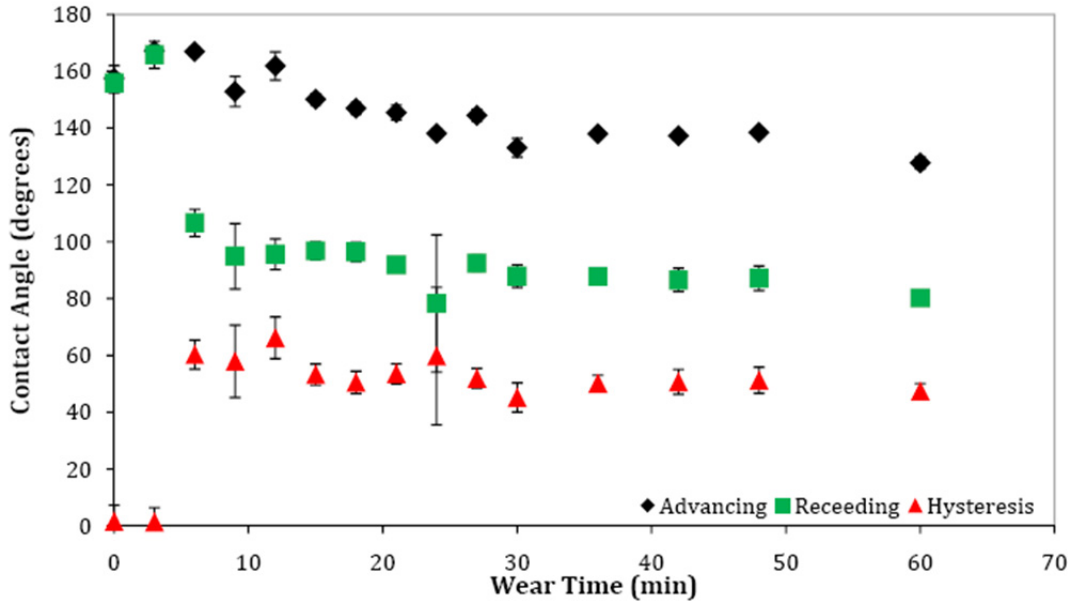

Figure 3-22: Wetting characteristic of plasma etched PTFE sample as it wears down. It can be seen superhydrophobicity is lost after 6 minutes of wearing down

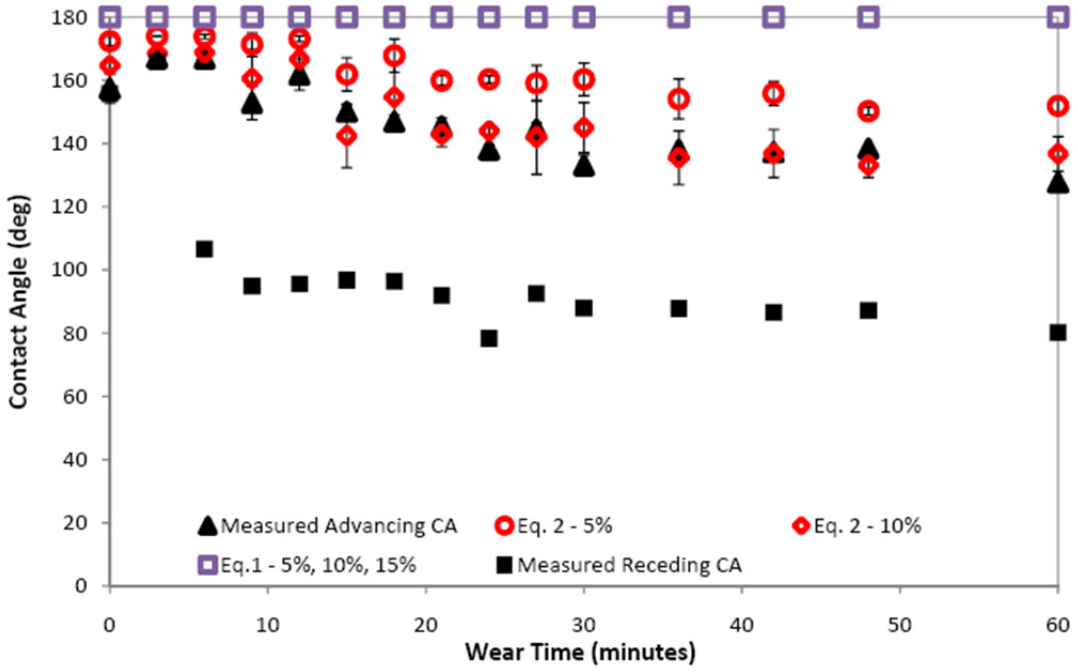

Figure 3-23: Prediction of CA behaviour with equation (1) and equation (2) for plasma etched PTFE samples. Advancing CA, hence adhesion can be predicted by fitting equation (2). Receding CA cannot be predicted by any of the two equations. Equation (1) remains indeterminate for all values of percentage penetration.

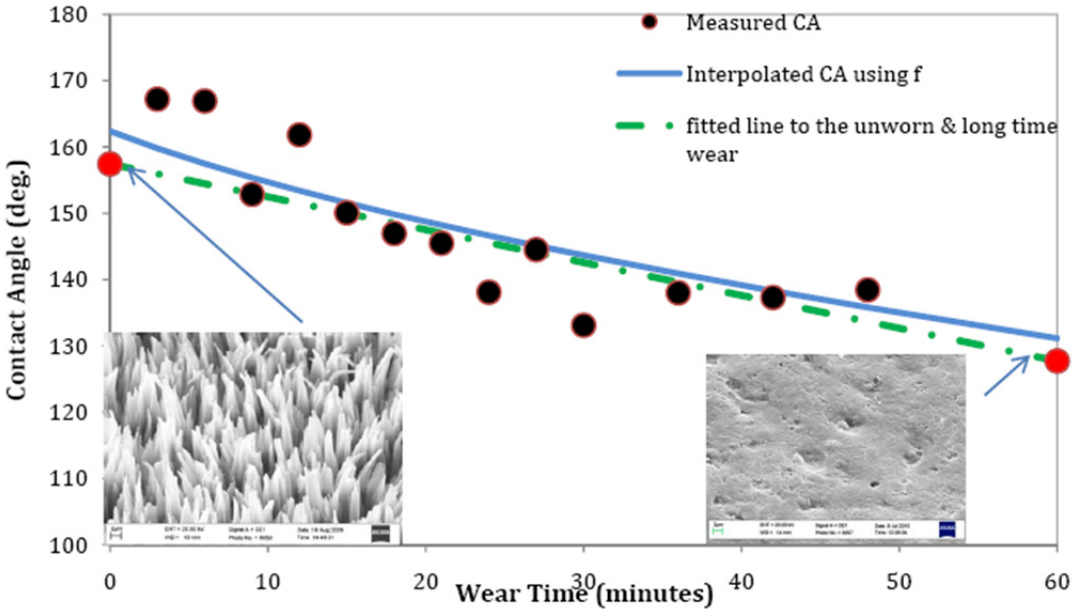

Figure 3-24: Predicting intermediate wetting behaviour of plasma etched PTFE surface by using unworn and long term behaviour characteristics. Advancing CAs are calculated by interpolating f parameter based on values of f at unworn and long term wear. Linear fit between unworn and long term wear is also shown. With respect to interpolation, linear fit is consistently giving good with predicting intermediate advancing CAs.

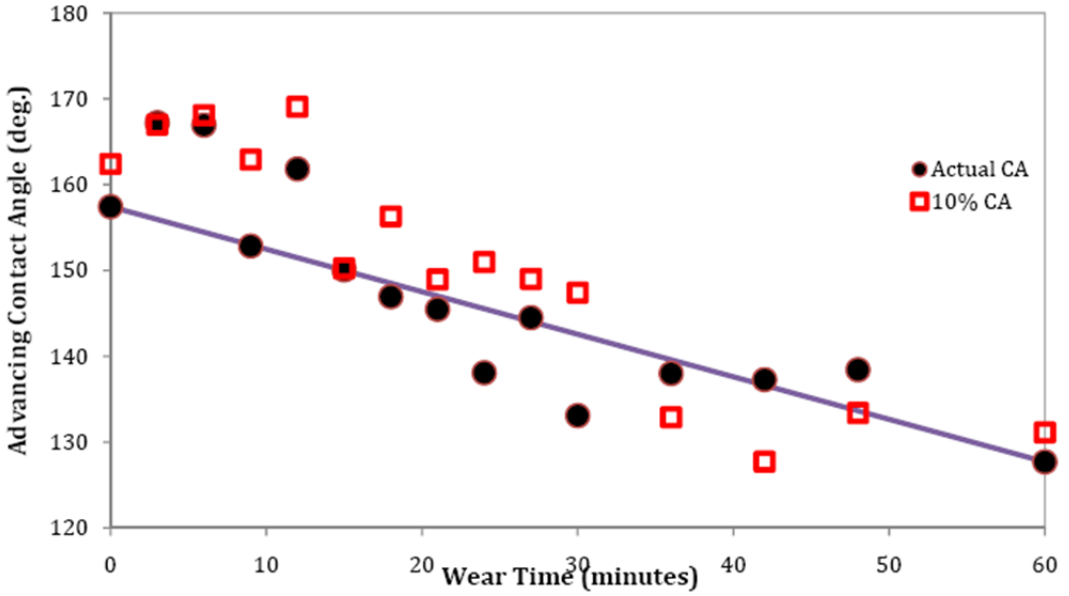

Figure 3-25: Co-relating Wetting and wear of plasma etched PTFE surfaces by comparing the linear fit with 10% penetration CAs predicted by eq. (2). With comparison to eq. (2), linear fit is consistently better at predicting intermediate advancing CAs.

3.3 Future work

The original Cassie equation (1) cannot predict either advancing or receding contact angles. Equation (2) is able to predict advancing contact angles, which is useful as a model, or an equation, for predicting CAs. Keeping this fact in mind, work will be continued on developing a new equation or model using various surface parameters to help predict advancing and receding CAs on a surface. Eq. (1) has only been tested with random geometries; work is underway to validate the feasibility of using this equation for fixed regular geometries, where one can easily deduce Cassie parameters f, f_1 and f_2.

4 A Thermodynamic Approach for Understanding the EdgeEffect on Wetting

4.1 Introduction

A drop placed on top of a pedestal/pillar (cylindrical, upright frustum, and inverted frustum geometries) away from edges will take its equilibrium contact angle. However, growing such drop causes the contact line to arrive at the edge of a pillar. The edge is known to hinder the drop from further spreading and spilling over to the sides of the pillar even if the apparent contact angle would exceed the advancing contact angle value.[14-16]

Such an effect is called the edge effect in wetting (or pinning effect at the solid edge). It plays an important role in many wetting phenomena in practical applications. For example, the preference of attaching at edges for frothing bubbles in the mineral floatation and the propensity for water to resist overflowing at the edge of a container.[17, 18] As it is known, solid edges (sharp or round corners, depending on the view from different scale, would form a solid edge) will necessarily exist when there is the surface roughness. Accordingly, the edge effect can play an important role in the wetting behaviour on roughened surfaces with various micro-geometries.

The diversity of surface micro-geometries allows nature to develop a large variety of multi-functional biological surfaces.[19-21] In particular, many efforts have been devoted into the investigation of the effect of surface roughness or micro-geometry (as opposed to the surface chemistry) on surface wettability. As an example, superhydrophobicity[22-32] is one of the most attractive roughness-induced wetting properties studied in recent years. On superhydrophobic surfaces (SHS), a water drop exhibits a quasi-spherical shape because it remains suspended on top of the micro-geometries and air is entrapped at the interface between liquid and solid (a so-called composite state). With a large static contact angle (CA) and low contact angle hysteresis (CAH, i.e., the difference between advancing or maximum and receding or minimum contact angles[33]), natural SHS will show interesting surface properties, e.g., the self-cleaning property of some plant's leaves[34-37] and animal's wings,[38, 39] the super-floating ability of water-strider[40-42] and the anti-fogging property of mosquito compound eyes.[43] Motivated by many applications of SHS, researchers are trying to gain a comprehensive understanding of superhydrophobicity and find robust SHS.

Studies[44-47] have shown that the edge effect would play an important role in the pinning and de-pinning behaviours of the three-phase contact line (TPCL) of drops on SHS and thus affect the advancing and receding CAs, particularly for SHS consisting of pillar structures.

For instance, on parallel grooved or wrinkled surfaces, the drop contact line shows a larger pinning effect or CAH in the orthogonal direction to the grooves, where the contact line meets the solid edge, than it is in the parallel direction to the grooves, where the contact line meets no solid edge.[48-50] On the other hand, drops on SHS may easily experience a transition from composite state to noncomposite state[51-53] (i.e., the TPCL may cross over the solid edges of the micro-structure and result in a liquid penetration into the troughs of a rough surface), resulting in a loss of the superhydrophobicity, see Figure 4-1. A re-entrant structure design[54-64] for the edge of microgeometries of SHS would inhibit the TPCL of a liquid drop from crossing the solid edges

and ensure drop suspension even for low surface tension liquids. Understanding the edge effect is important for design of robust superhydrophobic or superoleophobic surfaces.

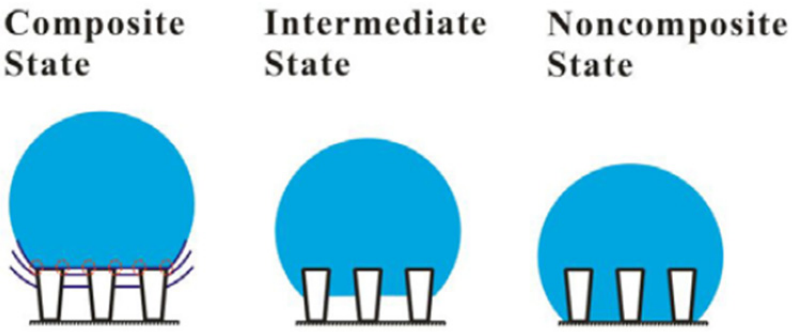

Figure 4-1: Schematic showing the transition of drop from composite state to noncomposite state. Note that the edges of the pillars play an important role for inhibiting the transition.

There are many studies[14, 65-74] dealing with the edge effect on wetting, but few of them have advanced the understanding beyond Gibbs'[75] inequality condition analysis for drop contact line at a sharp solid edge. Oliver *et al.*[14] first examined Gibbs' results by studying water drop spreading behaviour on one single pedestal with different kinds of sharp edges (defined by an angle subtended by the two surfaces forming the solid edge – "edge angle") theoretically and experimentally. They indicated that Gibbs' conclusion is mainly a geometrical consequence immaterial to the intrinsic nature of the edge (e.g. the selective adsorption of impurities on the edge). Later, though it is indicated that Gibbs made a mistake in his argument,[70] Gibbs' principle has been widely employed to explain the wetting phenomena taking place on micro-structured surfaces,[72,76–78] e.g., the origin of CAH on rough surfaces.[74, 79] Recently, with the increasing interest in SHS, researchers realized a fundamental influence of edge effect in superhydrophobicity, especially in the stability of the composite drop state on SHS. Kurogi et al.[44] found a remarkable deviation of measured CA from the expected theoretical values on SHS. Hence, they suggested that the pinning effect of wetting at the solid edges of the micro-geometries (or edge effect) should be taken into consideration as an important mechanism for SHS, though their demonstration was somewhat crude and some speculative statements were involved. By pressing a conical frustum into liquid, Sheng et al.[73] observed a strong restricting ability, to water drop spreading around the edges of the frustum, which was closely related to the geometric morphology of the edges and the intrinsic CA. Inspired by this, they have gained superhydrophobicity of the materials with lower hydrophobicity by constructing close micro-edges on the flat surfaces.

Moreover, to further reveal the pinning effect of wetting at edges (or edge effect) of micro-geometries on SHS, model SHS with regularly distributed pillars were prepared.[46, 47] However, it is still relatively complex due to the complexity of the solid-liquid-air composite interface for a drop sitting on top of large numbers of pillars. Therefore, efforts have been made to study the edge effect for a water drop sitting on a single pillar,[15, 16, 80] focusing on discussing the water drop suspension ability caused by the pinning effect of the pillar edge. In fact, this simplified model is still of practical use, for the water drop may grow from a small-size drop sitting on top of one single pillar during a condensation process.[81] Extrand[15] proposed a model analysis to predict the

critical suspension volume of a drop on a single pillar based on Gibbs' inequality condition. The model accounts for both capillary forces and gravity and is only valid where the liquid surface tension at the contact line is directed upward (the CA of a drop on the pillar may show a value above 180°). Du et al.[80] investigated the profiles of liquid drops at the tip of one cylindrical fibre after drop collapse. They observed, and theoretically demonstrated, the formation of a spherical cap on the fiber tip and a full, symmetrical liquid bell on the fibre body adjacent to the fibre tip. Tóth et al.[16] reported the suspension of water drops deposited on vertical single pillar with both circular and square cross sections by experimental and numerical studies. They have attributed the observed drop shapes to the geometric pinning of the contact line to the pillar edge and found a good consistence with Gibbs' inequality condition. Nevertheless, the above studies for drops on single pillars are limited, because none of them included a discussion of all the parameters affecting the edge effect, e.g., the edge angle, intrinsic CA and drop volume.

Despite a number of experimental and theoretical studies, the underlying thermodynamic mechanisms responsible for the edge effect have not been fully revealed. In addition, there is still a lack of systematic investigation of all the parameters (e.g., the edge angle, intrinsic CA and drop volume) affecting the edge effect. In this study, a 3-D free energy model for water drop on top of a pedestal/pillar (cylindrical, upright frustum, and inverted frustum geometries) has been proposed. By providing the detailed free energy information around the edge, the thermodynamic origin of the edge effect can be well understood. Results show good consistence with the work of Oliver *et al.*[14] which is based on volume condition analysis. In the end, universal wetting graphics have been obtained for a drop on a single pillar, providing specific guidelines for the design of microstructures of robust superhydrophobic and superoleophobic surfaces.

4.2 Theoretical Section

4.2.1 Edge effect theories

The edge effect is usually described by the model[14–16] given schematically in Figure 4-2a. By changing the edge angle Φ, the model pillar with circular cross-section varies from upright frustum to inverted frustum shapes. For a drop placed on top of the pillar away from the pillar edge (the radius of drop contact circle r < the radius of the pillar top R), an equilibrium CA will be shown. If the pillar surface (top and side surfaces) is smooth and homogeneous, the equilibrium CA (θ_Y) is the intrinsic CA which can be predicted by Young's equation:

$$\gamma^{la}\cos\theta_Y = \gamma^{sa} - \gamma^{ls} \tag{3}$$

where γ^{la}, γ^{sa} and γ^{ls} are interfacial tension at liquid-air, solid-air and liquid-solid interfaces, respectively. As the drop volume increases, the TPCL advanced and is finally pinned at the pillar edge ($r = R$); that is, the position of the contact line remains unchanged at the edge, but the equilibrium CA increases from θ_Y to a critical maximum value $\theta_C = \theta_Y + (180° - \Phi)$, which is referred to as Gibbs' inequality condition. Oliver *et al.*[14] illustrated that three wetting states may take place after the contact line reaches the pillar edge (the gravity is absent), depending on the relationship between θ_Y and Φ:

- For case A, $\Phi <= \theta_Y$: as the drop volume increases, the TPCL will be always pinned at the edge while the drop equilibrium CA approaches but never reaches θ_C (>= 180°).
- For case B, $\Phi > \theta_Y$ & $\Phi > \theta_Y + 2atan(0.5cot\ \theta_Y)$: as the drop volume increases, the TPCL will first be pinned at the edge and the equilibrium CA then approaches θ_C; after the drop's equilibrium CA reaches θ_C, further increase of the drop volume will allow the TPCL to steadily move over the edge.
- When $\theta_Y < \Phi < \theta_Y + 2atan(0.5cot\ \theta_Y)$: as the drop volume increases, the wetting behaviour is the same as case B before the drop CA reaches θ_C; however, unlike case B, after it reaches θ_C, the TPCL jumps suddenly and spreads spontaneously down the side of the pillar. This will be called case C. Case C has been studied by Du et al.[80] experimentally and theoretically (e.g., θ_Y=17° and Φ=90°), showing a spherical cap on the fibre tip and a symmetrical bell-shaped meniscus on the fibre body adjacent to the fibre tip (after the drop collapse). However, it is still difficult to get a full physical picture for such wetting behaviour. A clear explanation will be given in our thermodynamic analysis (see Section 4.3.2).

It is worth pointing out that Oliver's conclusions were based on a volume condition analysis. Thus, although it gives a description for the wetting behaviour of the drop TPCL at the edge with increasing volume, the drop wetting state on a single pillar with a constant volume is still unclear. For instance, if a drop with the same volume is deposited on top of a single pillar varying from upright frustum to inverted frustum geometries (see Figure 4-2b), it is difficult to use Oliver's[14] results to explain the difference between them.

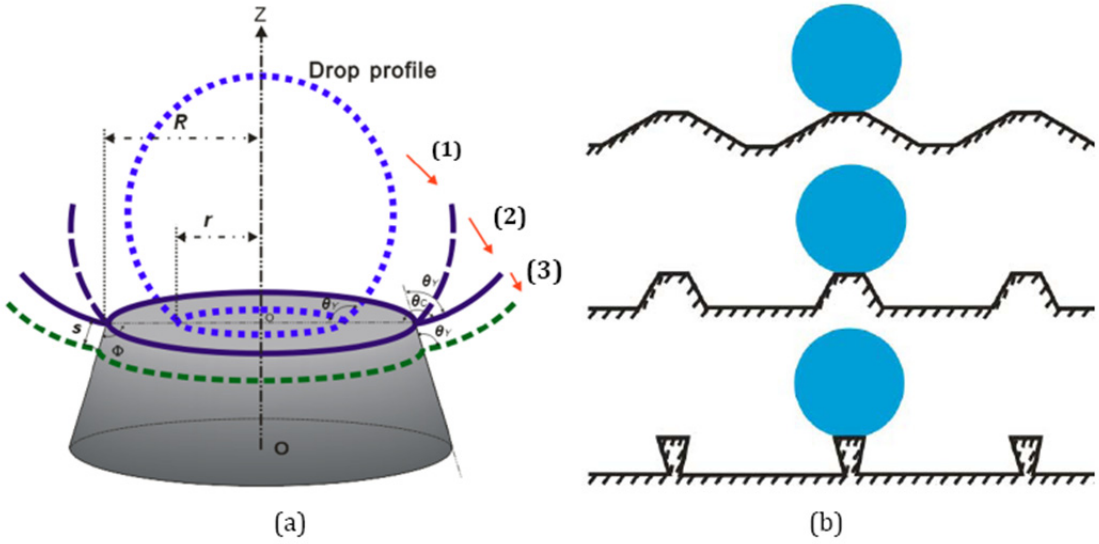

Figure 4-2: (a) Schematic depiction of the motion of the drop TPCL on a single pillar with increasing the volume: the TPCL is approaching the pillar edge (1), pinned at the pillar edge (2) and after crossing over the pillar edge. (b) Schematic showing drops with constant volume sitting on one single pillar from upright frustum to inverted frustum geometries. Note that the single pillar can be one of the periodically aligned pillars for the model SHS.

4.2.2 Thermodynamic Model

A 3-D free energy model is proposed to obtain a detailed knowledge of free energy (FE) states for a drop deposited on top of a single pillar, see Figure 4-3. Some assumptions were made as follows: (1) gravity and line tension are ignored in order to simplify the model and focus on the basic factors (edge angle, intrinsic CA and drop volume) affecting the edge effect; (2) drop profile can be assumed to be spherical when the displacement is beyond the edge $s << R$; (3) the solid surface is isotropic and homogeneous.

When the drop TPCL recedes from the pillar edge A (the radius of the drop contact line $L_A = R$) with an apparent CA (θ_A) to an arbitrary position B (L_B) with θ_B (see Figure 4-3a), the system FE will change due to the changes of liquid-air, solid-air and liquid-solid interfacial areas. Note that the apparent CA (θ_A or θ_B) is not necessarily an equilibrium CA. The system FE for the drop at A and B can be represented as:

$$F_A = \gamma^{la} A_A^{la} + \gamma^{sa} A_A^{sa} + \gamma^{ls} A_A^{ls} + C \tag{4}$$

$$F_B = \gamma^{la} A_B^{la} + \gamma^{sa} A_B^{sa} + \gamma^{ls} A_B^{ls} + C \tag{5}$$

where A^{la}, A^{sa} and A^{ls} are the liquid-air, solid-air and liquid-solid interfacial area, respectively; C denotes the FE of the portion of the system that remains unchanged.

Young's equation (eq 3) is locally valid and as such, the corresponding change of FE for a drop receding from position A to B can be expressed by:

$$\frac{\Delta F_{A\to B}}{\gamma^{la}} = \frac{(F_B - F_A)}{\gamma^{la}} = \frac{\pi L_B^2 (1 - \cos\theta_B)}{sin^2\theta_B} - \frac{\pi L_A^2 (1 - \cos\theta_A)}{sin^2\theta_A} + 0.5\pi (L_A^2 - L_B^2) cos\theta_Y \tag{6}$$

note that the unit of energy (J/m^2) has been normalized with respect to γ (J/m^2). In addition, according to the constant drop volume (V) condition, eq 7 is derived from geometrical analysis:

$$V_B = \frac{\pi L_B^3 (1 - cos\theta_B)^2 (2 + cos\theta_B)}{3 sin^3\theta_B} = \frac{\pi L_A^3 (1 - cos\theta_A)^2 (2 + cos\theta_A)}{3 sin^3\theta_A} = V_A \tag{7}$$

Here, the FE state for the drop at position A, which is right at the pillar edge, is selected to be the reference FE state and assigned an arbitrary value of zero, $F_A = 0$. As a result, the relative FE for the drop at any arbitrary position B for $L_B < L_A$ (it is an edge if Φ is smaller than 180°) can be determined by solving eqs 6 and 7 via successive approximations. Note that the drop volume (V) at the reference position A (V_A) is determined by the value of L_A and θ_A. Thus, any of the three parameters (V, L_A and θ_A) can be easily gained if two of them are known.

Similarly, when the drop TPCL crosses over the pillar edge, $L_B > L_A$, and sits at an arbitrary position C (on the sidewall of the pillar if Φ is smaller than 180°, see Figure 4-3b), the FE equations and constant volume condition can be derived as follows:

$$\frac{\Delta F_{A\to C}}{\gamma^{la}} = \frac{(F_C - F_A)}{\gamma^{la}} = \frac{\pi L_C^2(1-cos\theta_C)}{sin^2\theta_C} - \frac{\pi L_A^2(1-cos\theta_A)}{sin^2\theta_A} - 0.5\pi(L_A + L_C)L_{AC}cos\theta_Y \quad (8)$$

$$V_C = \frac{\pi L_C^3(1-cos\theta_C)^2(2+cos\theta_C)}{3sin^3\theta_C} - \frac{1}{3}\pi L_{AC}(L_A^2 + L_A L_C + L_C^2)sin\Phi = V_A \quad (9)$$

L_{AC} is defined as the distance between point A and C on the side wall of the pillar. Note that the apparent CA for the drop at the arbitrary position C (θ_C) is defined as the angle between the tangent to the drop at the three-phase contact line and the horizon (see Figure 4-3b). Thus, the relative FE for a drop at any arbitrary position C can also be obtained.

Attention should be paid to the judgment of the existence for a spherical drop cap when the TPCL has passed over the pillar edge, as the pillar edge may touch the drop cap if the edge angle Φ is too small or the displacement of TPCL over the edge is too large. The criterion can be written as:

$$L_{C'} = \sqrt{\frac{L_C^2}{sin^2\theta_c} - \left(\frac{L_C}{tan\theta_C} + L_{AC}sin\Phi\right)^2} > L_A \quad (10)$$

As it is seen in Figure 4-3b, if $L_{C'} > L_A$, a spherical drop profile can be satisfied; if $L_{C'} \leq L_A$, the pillar edge touches the drop cap.

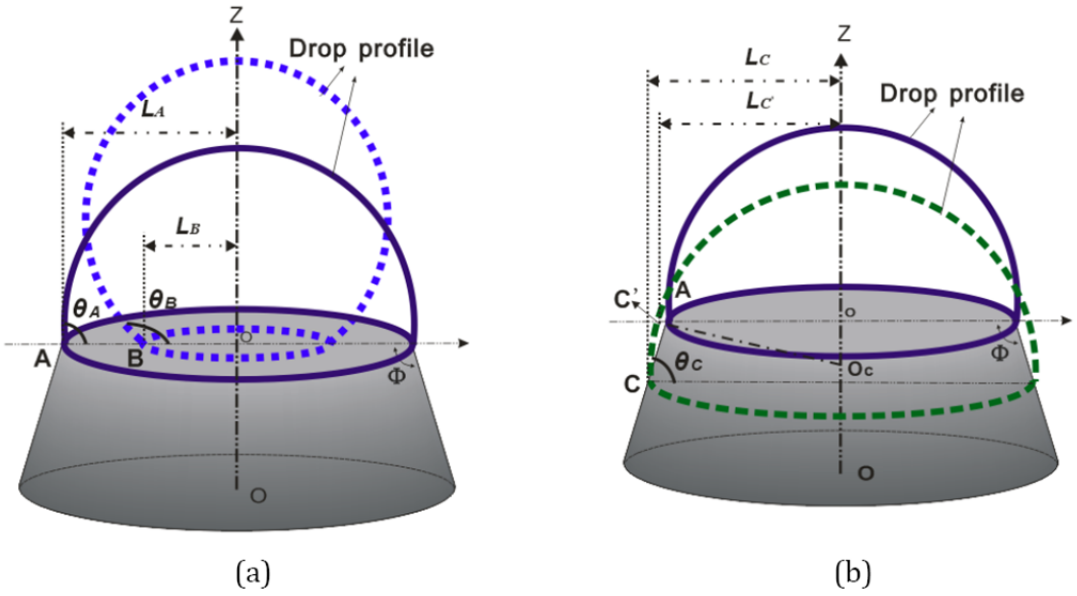

Figure 4-3: Illustration of FE analysis for a drop on a single pillar. (a) For drops sitting at the reference position A and an arbitrary position B before crossing over the edge. (b) For drops sitting at the reference point A and an arbitrary position C after crossing over the edge. Note that the apparent CA is defined as the angle between the tangent to the drop at the three-phase contact line and the horizon. If Φ = 180°, the model becomes a flat surface; if Φ < 90°, the model pillar becomes inverse-trapezoidal or re-entrant structure.

4.3 Results and Discussion

4.3.1 Thermodynamic Origin of the Edge Effect

Before proceeding with the model analysis, a typical FE curve is given for a drop ($V = 2.8 \times 10^{-4}$ μL) deposited on a flat model surface ($\theta_Y = 60°$, $L_A = 4.6 \times 10^{-5}$ m, $\theta_A = 100°$, $\Phi = 180°$) as an example (see Figure 4-4), to make our results and discussion clear. Note that if the edge angle Φ is set to be 180°, the pillar model shown in Figure 4-3 will become a flat model surface. One can see that a minimum (bowl-shaped) FE curve contains a solid line part representing the drop FE states at positions C (positions for drop after crossing over the reference position A, $L_C > L_A$) and a dotted line part representing the drop FE states at positions B (positions for drop before crossing the reference position A, $L_B < L_A$). In this case, one global minimum FE state is observed which is on the solid line part (a position C), with the corresponding CA showing 60°. In other words, when a drop ($V = 2.8 \times 10^{-4}$ μL) is deposited on the flat model surface, it will spread to a position C to reach an equilibrium drop state and exhibit an equilibrium CA of 60°. This is easily understandable because the equilibrium CA of the most stable state for a drop on an ideally smooth surface is naturally expected to be the intrinsic CA ($\theta_Y = 60°$ in this case). The result shows good agreement with statements of some previous models[82, 83] for the thermodynamic analysis of smooth, homogeneous solid surfaces. Furthermore, FE curves illustrating wetting

case A, case B and case C (Oliver et al.[14]) mentioned in the section 4.2.1 are given and explained in the supporting information. The agreement shows the validation of the thermodynamic model.

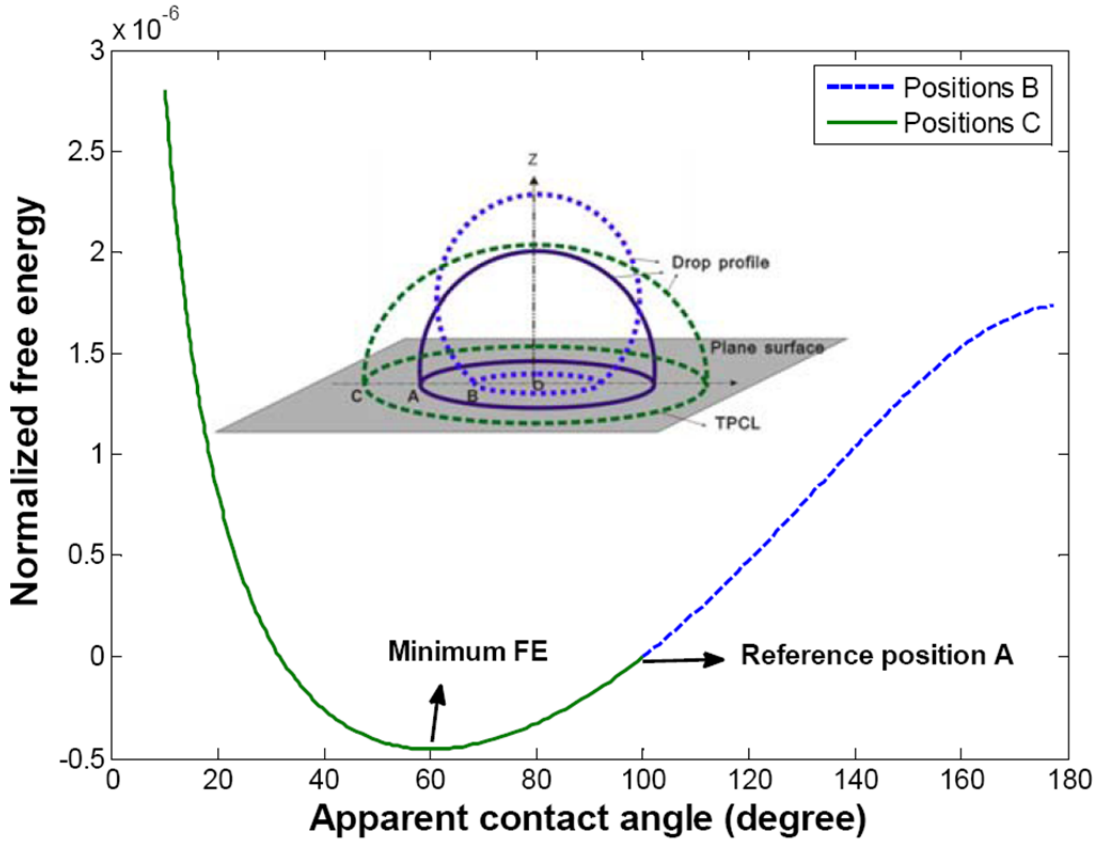

Figure 4-4: Normalized free energy as a function of the apparent CA on a flat model surface (θ_Y = 60º, $L_A = 4.6\times10^{-5}$ m, θ_A = 100º, Φ = 180º, $V = 2.8\times10^{-4}$ µl).

In order to understand the edge effect, the thermodynamic model described above is applied to obtain the FE curves for drops ($V = 2.8\times10^{-4}$ µL) placed on model surfaces (θ_Y = 60º, $L_A = 4.6\times10^{-5}$ m, θ_A = 100º) with different edge angle Φ (180º, 150º and 120º), see Figure 4-5. As illustrated in Figure 4-5b, the dotted line parts (the drop FE states at positions B, $L_B < L_A$) of the FE curves for the three model surfaces overlap with each other; that is, the FE states for the drop TPCL at positions B are insensitive to the edge angle Φ. In contrast, the solid line parts (the drop FE states at positions C, $L_C > L_A$) of the FE curves for the three model surfaces show an obvious difference. Compared to the FE curve for the drop on the flat model surface (Φ = 180º), the minimum FE state rises (from -45 x 10^{-8} to -4 x 10^{-8}) and the equilibrium apparent CA shifts up (from 60º to 90º) for the drop on the model surface with a smaller edge angle (Φ = 150º). Meanwhile, the most stable drop TPCL on the model surface with Φ = 150º is located at a position closer to the reference position A than that with Φ = 180º, see the schematic illustration in Figure 4-5a. Because there is an edge existing for the model pillar with Φ = 150º as compared to the flat model surface with Φ = 180º, the conclusion can be made here that the difference between the FE states and wetting behaviour for the two models is caused by the edge effect.

This is the first time that an explanation of thermodynamic origin of the edge effect has been given. Moreover, further decrease of the edge angle will finally increase the apparent equilibrium CA to 100º (note that θ_A = 100º in this case) and thus the most stable TPCL is just at the edge (the reference position A), see Figure 4-5. In conclusion, an edge angle small enough can make the most stable drop TPCL be at the edge, without risking a drop collapse onto the sidewall of the pillar; i.e., the decrease of edge angle will increase the ability for a pillar to suspend a drop.

This explains the reason that re-entrant micro-pillars[54-64] (Φ < 90º) are preferred to construct robust-SHS or superoleophobic surfaces.

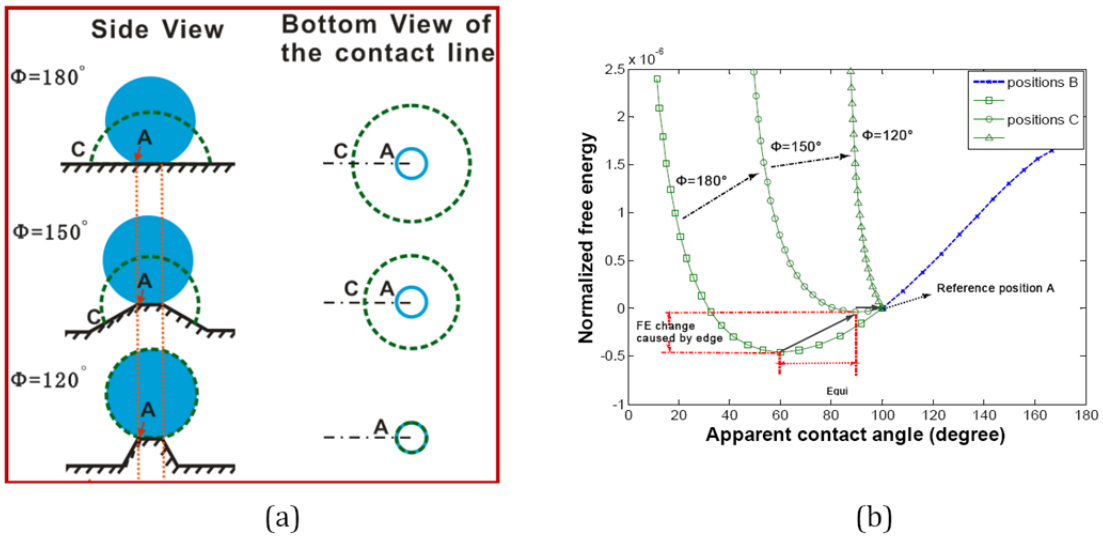

(a) (b)

Figure 4-5: (a) Schematic showing drops placed on model surfaces with different edge angle Φ (180º, 150º and 120º). (b) Normalized FE curves as a function of the apparent CA for the cases shown in (a) (θ_Y = 60º, L_A = 4.6×10^{-5}m, θ_A = 100º, Φ = 120º, 150º and 180º, V = 2.8×10^{-4}µl).

4.3.2 Four Typical Drop Wetting States

On the basis of the above discussion, the drop FE states at positions B (before crossing over the edge, $L_B < L_A$) will not be affected by the edge angle Φ. Hence, in the following discussion, only the drop FE states at positions C (after crossing over the edge, $L_C > L_A$) will be kept in the FE graph and discussed. In order to find the effect of the edge angle Φ on the drop wetting behaviour, the normalized FE as a function of the apparent CA and edge angle Φ are obtained for a drop (V = 0.01µl) on a single pillar (θ_Y = 60º, L_A = 4.6×10^{-5} m, θ_A = 160º), see Figure 4-6a. The same FE graph, but from a different observation direction, has been given to get a general idea of the 3-D FE surface, as shown in Figure 4-6b. Note that for a fixed edge angle, a FE curve is obtained as it is shown in Figure 4-5. One can see that by increasing the edge angle from 20º to 130º, the FE curve gradually drops down and finally flips over to the other direction, with the reference position A being the rotation axis.

Consequently, there must be a critical point (marked as the collapse point Φ_T in the figure, Φ_T = 80º in this case) before which, the drop's minimum FE state will be at the reference position A;

but after which, the drop's minimum FE states will no longer be at the reference position A. This will be discussed in further detail below.

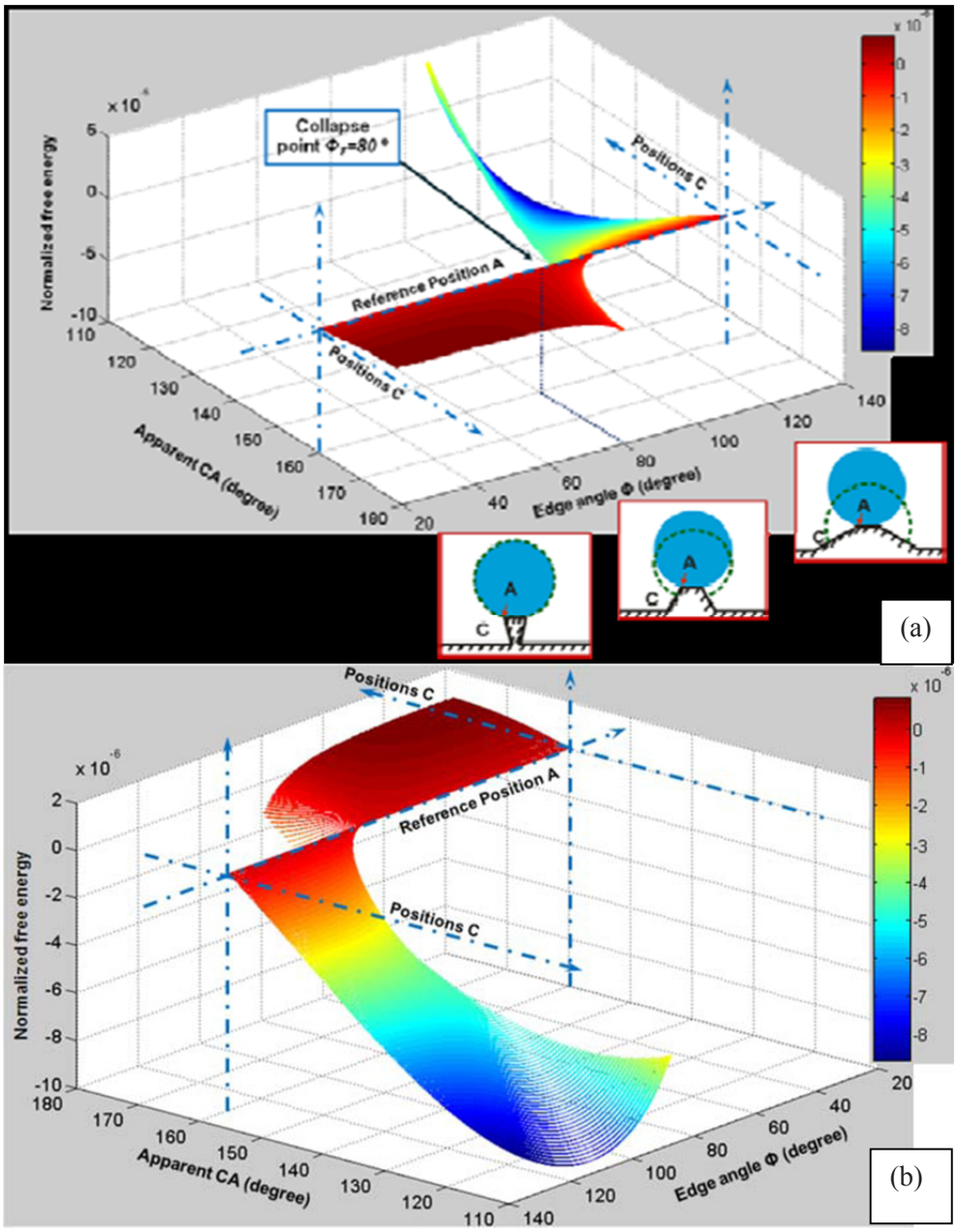

Figure 4-6: (a) The normalized FE of a drop sitting on single pillar as a function of apparent CA and edge angle Φ (θ_Y = 60°, $L_A = 4.6\times10^{-5}$m, θ_A = 160°, V = 0.01μl). (b) The same FE graph as (a) from another observation direction.

Through a closer look at the FE graph of Figure 4-6a, four specific wetting cases (case 1-4) are noted, showing different FE change characteristics (see Figures 4-7, 4-8 and 4-9). Figure 4-7 shows the part of FE graph for edge angle ranged from 40° to 60°. One can see that the FE

increases monotonously as the apparent CA increases. This indicates that the drop's minimum FE state for a single pillar with edge angle between 40° to 60° is always at the reference position A (the pillar edge), implying a stable drop suspension on the top of the pillar, without risking a drop collapse onto the pillar sidewall. This wetting behaviour is referred to as wetting case 1.

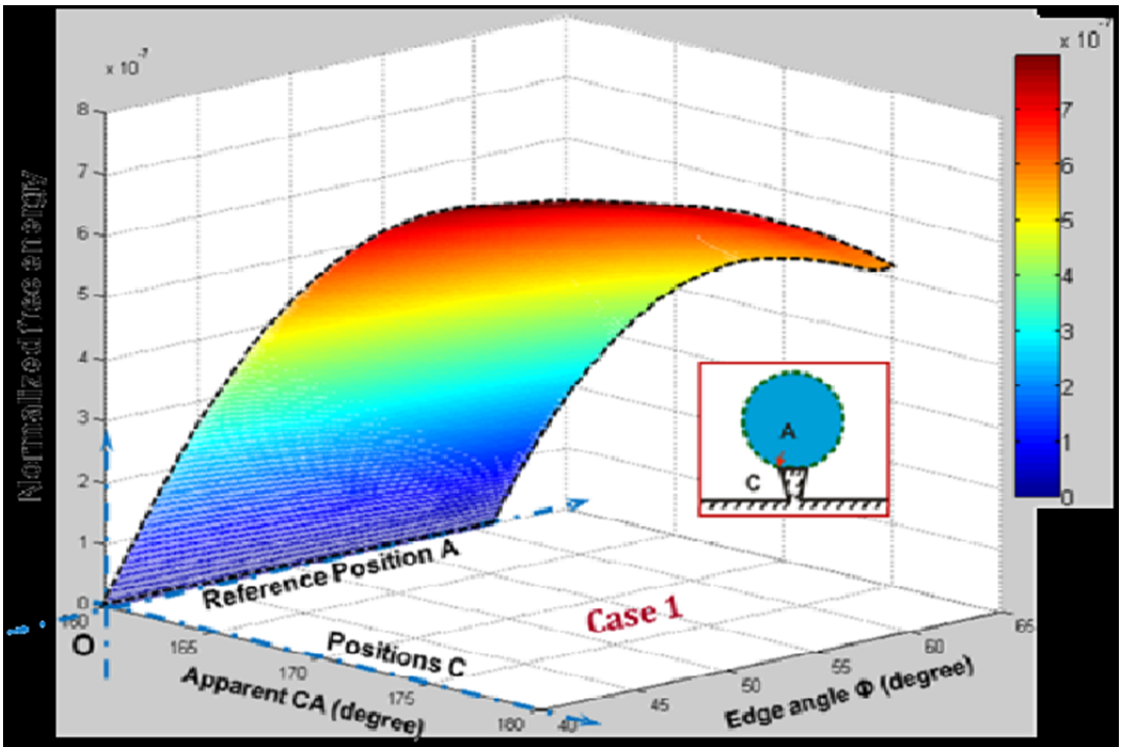

Figure 4-7: A part of FE graph (Figure 4-6) for edge angle Φ ranged from 40° to 60°, which is defined as wetting case 1. (θ_Y = 60°, $L_A = 4.6\times10^{-5}$m, θ_A = 160°, V = 0.01μl).

Figure 4-8 presents the part of the FE graph for edge angles ranging from 60° to 95°. Two wetting states can be determined. For the FE states of drops on single pillar with edge angle Φ = 60°~80°, the FE curve for each fixed edge angle Φ shows a convex shape; in other words, a free energy barrier (FEB) can be found in the FE curve (see the enlargement in Figure 4-8). As seen, there is a minimum FE state at the reference position A, indicating that the drop can be suspended stably on top of the pillar. However, if the FEB is overcome by an external energy provided from extra sources such as mechanical vibration, the drop will collapse onto the sidewall. Such FEB can be important for drop suspension on top of microstructures of SHS, preventing the transition from a composite state to a non-composite state. This wetting behaviour is referred to as case 2. For the part of FE graph with edge angle Φ = 80°~95°, the drop's FE, at the reference position A, is no longer the global minimum state. As a result, drops suspended on pillars with edge angle Φ > 80° are not stable, this is referred to as wetting case 3. As mentioned above, the critical point Φ_T (= 80° in this case) is considered as the collapse point, after which the drop collapse takes place. Interestingly, it is found that the collapse point Φ_T corresponds to a relationship $\Phi_T = 180°-\theta_A+\theta_Y$, allowing it to be easily found. Note that for both case 2, after the FEB, and case 3 the normalized FE decreases as the apparent CA approaches 180°, and stops at a position where the criterion (Eq 8) for forming a spherical drop cap is violated. In this case when the drop

collapses down, the pillar edge will finally touch the drop cap (see the criterion Eq 8), and then the drop may be split into two parts as stated by Du et al.[80] (see Section 4.2.1 and Figure B-3 in Annex B).

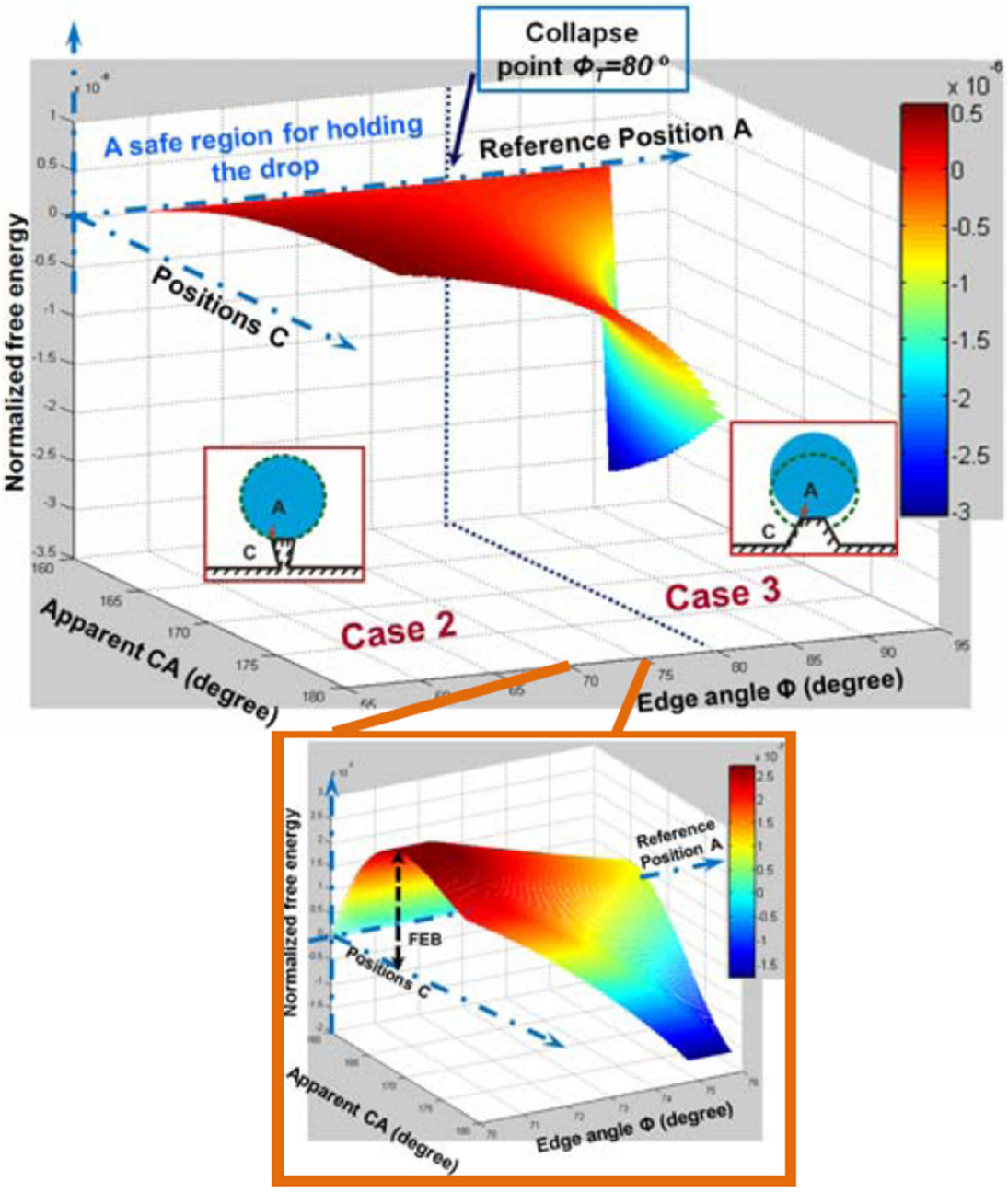

Figure 4-8: A part of FE graph (Figure 4-6) for edge angle Φ ranged from 60° to 95°, which is defined as wetting case 2 (Φ = 60°~80°) and case 3 (Φ = 80°~95°). The enlargement is given for edge angle Φ ranged from 70° to 75°. (θ_Y = 60°, $L_A = 4.6\times10^{-5}$ m, θ_A = 160°, V = 0.01μl).

Figure 4-9 presents the part of the FE graph for edge angles ranging from 100° to 150°. In this range the FE decreases from reference position A, with minima observed at each edge angle Φ. This indicates that the drop (V = 0.01μL) will not be stable on top of the pillar. But unlike case 2 and case 3, the most stable drop TPCL can stay on the pillar sidewall. This wetting state is referred to as case 4.

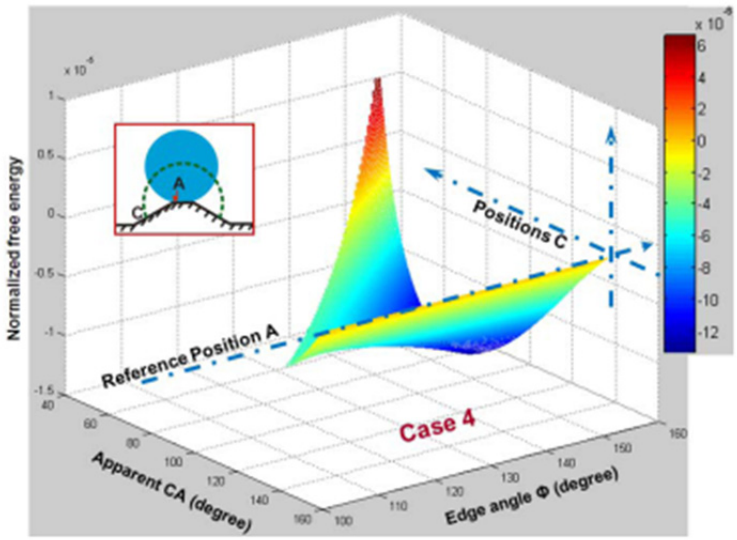

Figure 4-9: A part of FE graph (Figure 4-6) for edge angle Φ ranged from 100 to 150°, which is defined as wetting case 4. (θ_Y = 60°, L_A = 4.6×10^{-5} m, θ_A = 160°, V = 0.01μl).

4.3.3 Drop Wetting Graphics on Single Pillar

Based on the above analysis, four different wetting cases (cases 1-4) have been shown. In particular, by defining the different FE change characteristics, the boundaries for the four wetting cases can be easily determined. Accordingly, a wetting graphics for describing the four wetting cases can be obtained as a relationship between edge angle (Φ) and intrinsic CA (θ_Y). Taking the case (θ_Y = 60°, L_A = 4.6×10^{-5} m, θ_A = 160°, V = 0.01μl) as illustrated in section 4.3.2, for a fixed intrinsic CA (= 60°), three critical edge angles (60°, 80° and 100°, see the red arrows marked in Figure 4-10) can be found to separate the four wetting cases; note that Φ = 80° is on the collapse transition line Φ_T = 180°-θ_A+θ_Y. Similarly, the other critical edge angles for separating the four wetting cases can also be determined at various intrinsic CA. As a result, the wetting graphics for defining the four wetting regions of a drop (V = 0.01μl) placed on top of a pillar (L_A = 4.6× 10^{-5} m) is obtained, see Figure 4-10. Note that the collapse transition line is dependent on the drop volume.

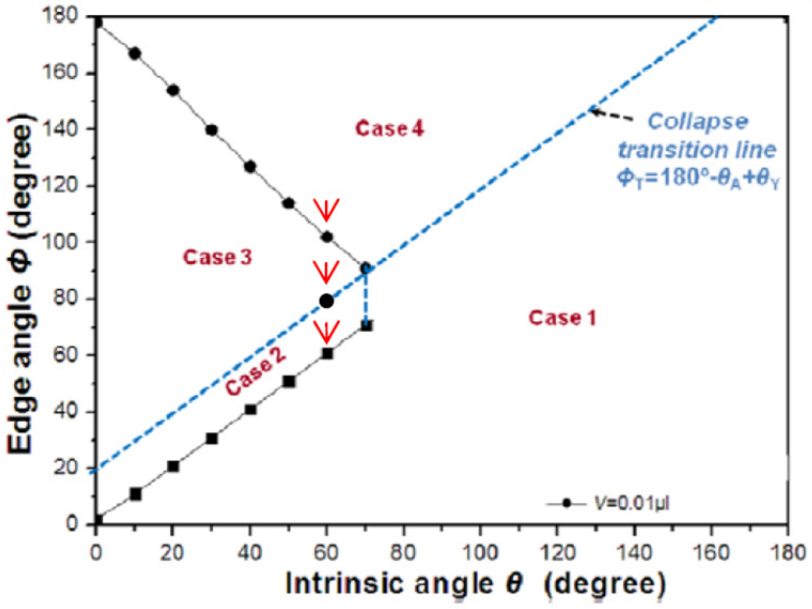

Figure 4-10: Wetting graphics for drop with fixed volume ($V = 0.01\mu l$ if $L_A = 4.6\times10^{-5}$ m) on single pillars with the relationship between edge angle (Φ) and intrinsic CA (θ_Y).

In a similar way, the wetting graphics for a drop as a function of its volume can also be determined; see Figure 4-11a. One can see that as the drop volume decreases from an infinitely large value to a small value (θ_A decreases from 180º to a small value), the collapse transition line (Φ_T = 180º-θ_A+θ_Y) defining the boundaries between cases 2 and 3, and cases 1 and 4 is shifting up; the boundaries for cases 3 and 4, and cases 2 and 1 are also changing correspondingly, see Figure 4-11a and Figure 4-11b. Interestingly, it is noted that the areas of wetting cases 3 and 4 decrease with decreasing drop volume. This is understandable because a drop with a small volume will have a lower probability of collapsing than a larger drop when deposited on top of a single pillar. This wetting graphic provides a framework for choosing pillar parameter settings, in order to gain maximum drop suspension, which is significant for designing robust superhydrophobic and superoleophobic surfaces.

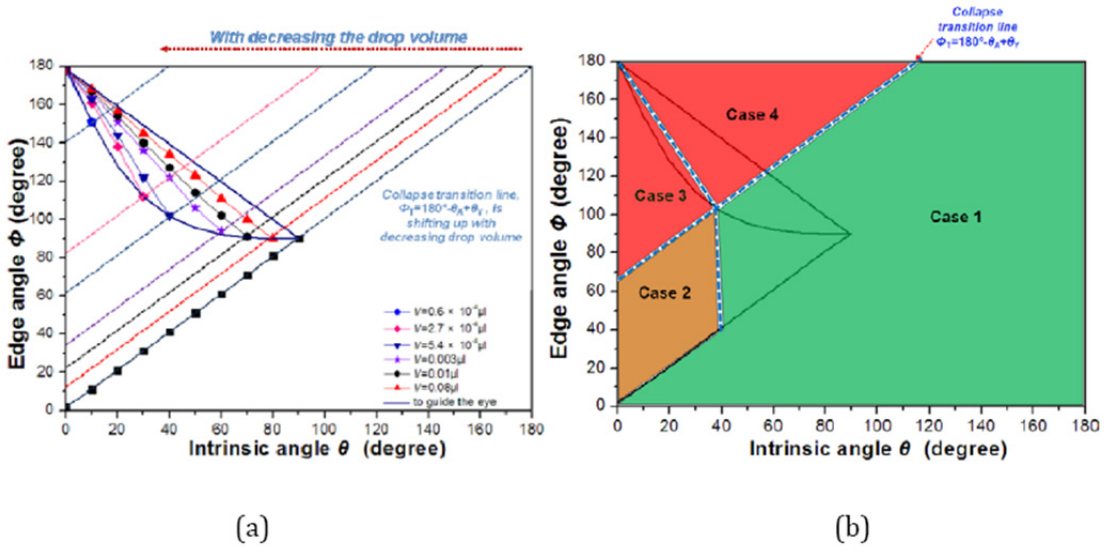

Figure 4-11: (a) Wetting graphics for drop on single pillars with varying drop volume in the relationship between edge angle (Φ) and intrinsic CA (θ_Y). (b) The same wetting graphics as shown in (a), taking $\theta_A = 115°$ as an example.

4.4 Conclusions

The edge effect has been applied to many applications though people may have not realized. For example, pillar microstructures with designed edge shapes (including inverse trapezoidal structures, re-entrant textures, nail-head-shaped pillars, etc.) have been experimentally applied to construct superhydrophobic surfaces, improving the robustness of superhydrophobicity or superoleophobicity. However, the thermodynamic mechanism responsible for the edge effect is still incompletely understood. In this study, a 3-D free energy analysis method was proposed to investigate the energetic states of drops on a single pillar as a function of edge angle and intrinsic CA. A clear thermodynamic depiction of the origin of the edge effect has been given by the analysis of drop FE levels before and after crossing the edge. Results show good consistence with previous work which are mainly based on Gibbs' inequality condition. In particular, four wetting cases for drops on single pillars have been observed: case 1, where a drop exists in a stable state on top of the pillar without risking the drop collapsing onto the pillar sidewall; case 2, where a drop exists in a meta-stable state on top of the pillar, and may experience collapse onto the sidewalls if the FEB is overcome by externally provided energy; case 3, where drop collapse onto the pillar sidewall is energetically favourable and the drop may split into two parts (a spherical cap on the fiber tip and a full, symmetrical bell on the sidewall[80]); and case 4, where drop collapse is energetically favourable and will result in a stable TPCL on the pillar sidewall. Finally, a universal wetting graphic is obtained for describing the four wetting regions as described by from the relationship between edge angle (Φ) and intrinsic CA (θ_Y). These results have provided fundamental rules for the design of robust superhydrophobic and superoleophobic surfaces by controlling the edge effect.

4.5 Associated Content

Supporting Information included in Annex B. FE curves illustrating wetting case A, case B and case C mentioned in the paper of Oliver et al.[14] are given and explained, showing the validation of the thermodynamic model.

5 Superhydrophobic and Superoleophobic Behaviour on Variant Geometry Micropillar Arrays

5.1 Introduction

Over the past ten months eight unique silicon wafers have been designed and fabricated with the intention of studying the effects of repellence and mobility of fluids of varying surface tensions on the textured surfaces. These eight surfaces used two different photomask designs and variations of lithographic techniques to produce a variety of different behaviours. Both of these photomasks had a variety of subsections with different cross-sectional geometries, so for the purposes of nomenclature and clarity the surfaces from the first photomask design shall have their different sections referred to as Settings, while those from the second design shall be referred to as Cases. This naming convention follows the physical labelling on the masks and helps differentiate between designs that have the same numerical designation but completely different geometries. Of these eight different wafers, all demonstrated behaviour consistent with superhydrophobic surfaces (SHS), (some are also oleophobic) but each had different behaviours with regards to their advancing contact angles (CA) and contact angle hysteresis (CAH), indicators of repellence and mobility, respectively. It should be noted that for consistency of thought and better comprehension of data some of the data presented in this chapter are passed the year two.

5.2 Photomask Design

The first photomask design features 21 Settings, divided evenly amongst arrays of microscopic square, triangular, and circular cross sectional areas arranged in a square packing arrangement. Of the 7 different Settings for each shape, 3 are both unique and useful while another 3 are slightly smaller copies of the first 3 and the final Setting for each shape has dimensions too large to demonstrate behaviour consistent with SHS. The reason for nearly half of the Settings on the first design being somewhat smaller variations of the other half is due to uncertainty in the fabrication parameters at the time of design leading to two different designs being used in order to ensure that one of them comes in at the correct size. This design was originally conceived for a different project but remained useful and viable for the current project as well.

The second photomask design features 8 different Cases, all featuring circular cross sectional areas of different diameters and spacing arranged in a close packed hexagonal pattern so as to produce the greatest degree of symmetry possible. Using data obtained from the fabrication parameters of the first design, each Case features unique geometry with no redundant copies. These geometries were designed larger than the needed feature size on the surface to compensate for reductions encountered between the values entered in the photomask CAD software and the final fabricated surface, a tactic that was largely but not entirely successful in producing the correct geometries. In addition to the textured portions, each Case also includes an attendant smooth section used to ensure that the intrinsic CA for the Case is as accurate as possible, rather than relying on a similarly treated but not identical unpatterned silicon wafer to determine the intrinsic CA behaviour. Due to a tendency observed when using the first photomask for Settings along the exterior of the wafer to have a greater incidence of fabrication defects, the textured

portions of the Cases were kept as close to the interior of the wafer as possible. Unlike the first design, the second was not for studying the effects of pillar geometry but the effects of high roughness on the transition from the Cassie to Wenzel states, with a secondary objective to observe the differences in contact angle as a function of the size and spacing of micro-pillars of the same cross sectional shape.

5.3 Fabrication Process

While the details of the fabrication process varied for each wafer at the etch step, the initial steps remained consistent for each wafer and for both photomask designs.

Fabrication began with the acquisition of silicon wafers from the University of Alberta's NanoFab. These wafers were cleaned of trace organic molecules by immersion in a hot piranha bath for 15 minutes. Piranha is a mixture of 97% sulphuric acid and 30% hydrogen peroxide at a 3:1 ratio and is the standard chemistry used in the semiconductor industry for the cleaning of silicon substrates. Once cleaned the wafers were given a layer of silicon dioxide by thermal oxidation in an oven at 1000°C while exposed to heated water vapour, for an exposure time of 25 minutes plus the oven ramp time and the subsequent cool down period with no exposure to water vapour. This produced a layer thickness between 200 and 300nm, depending upon the exact conditions within the oven at the time of oxidation.

Wafers with 500nm of silicon dioxide already prepared by NanoFab staff were also available and used when a specific layer thickness was unnecessary.

Once the wafers were oxidized, they were photolithographically patterned. The process began by applying a monolayer of hexamethyldisilazane (HDMS) to promote adhesion between the silicon dioxide and photoresist. A layer of HPR 504 photoresist approximately 1.25μm thick was applied via spin coating and then soft baked on a hot plate at 115°C for 90s before being allowed to sit for 15 minutes to reabsorb moisture from the surrounding air. Once the photoresist had finished stabilizing it was patterned with UV light and a mask aligner to transfer the pattern from the photomask to the photoresist. The developed photoresist was dissolved via 354 Developer. With the pattern from the mask properly transferred, the exposed silicon dioxide was etched using fluoroform (CHF_3) plasma in the NanoFab's STS RIE etcher.

From there the process flow varies between the different wafers, but two different deep reactive ion etching (DRIE) processes were used. The first process is cryo-etching, where the wafer being etched is first cooled to -110°C and then exposed to plasma formed from sulphur hexafluoride (SF_6) and oxygen (O_2) gases. The SF_6 gas decomposes into its constituent atoms when ignited as plasma and the fluorine ions etch away at any exposed silicon but not silicon dioxide. In the Oxford Instruments ICP-RIE, used in the NanoFab, the O_2 plasma and the cryogenic conditions cause the primary direction of etching to be along the direction of plasma bombardment, with a ratio between vertical and horizontal etching rates being approximately 150:1. Because of the cryogenic conditions, a layer of silicon dioxide must be used and the photoresist cannot remain in place or it will fracture and flake off in the cold, producing a large number of defects. The second DRIE process used in the fabrication of these wafers is the Bosch etch. In the standard Bosch etch SF_6 and octafluorocyclobutane (C_4F_8) plasmas are alternated, with the SF_6 serving as an isotropic silicon etchant while the C_4F_8 deposits and forms a passivation layer on the sidewalls of

the substrate being etched, preventing etching except for in the direction of plasma bombardment. This creates vertical sidewalls but with scallops. The precision Bosch etch is a variation of this process that applies both forms of plasma simultaneously, producing smoother sidewalls at a cost of a slower etch rate and defects forming for etches greater than approximately 10μm in depth. Because of the non-cryogenic conditions of the Bosch etch silicon dioxide is also etched along with silicon so the photoresist must remain on to prevent the silicon dioxide layer from being removed during the process and the silicon beneath it being etched as well. However, since the silicon dioxide etches at an approximate ratio of 20:1 in the STS ICP-RIE in the NanoFab, this can be exploited to produce novel surface and sidewall geometries, as was done for two of the wafers.

For all wafers, the photoresist removal process involved a bath in acetone followed by a rinse with isopropyl alcohol (IPA) and de-ionised (DI) water and a final descum by oxygen plasma using the NanoFab's Branson 3000 barrel etcher.

5.4 Specific Fabrication and Results

The first study done sought to examine the relationship between the undercut angle of a micro-pillar array and the wettability characteristics produced. Previous research[54, 61] showed that micro-pillar arrays with a silicon dioxide cap on top of columns of silicon of significantly smaller diameter produced greater stability of the Cassie state than pillars with vertical sidewalls. These arrays could allow for superoleophobic surface (SOS) as well as SHS behaviour. To this end four wafers were produced with varying undercut geometries: vertical sidewalls (90°), slightly inwardly sloped sidewalls (80°), complete undercut (CU) capped pillars, and hybrid undercut (HU) capped pillars that featured both undercutting on the caps and vertical sidewalls in line with the caps. A fifth variation was also serendipitously discovered, and studied, featuring pillars with silicon grass present on the sidewalls and tops. Silicon grass is associated with the DRIE processes whereby small defects result in the formation of vertical pillars of silicon with diameters less than 100nm.[84] This fifth wafer is referred to as the lesser silicon grass (LSG) wafer, due to later experimentation improving upon the process. Of these five wafers, only Settings 5, 11, and 15 were studied due to these all being unique settings, featuring circular pillar cross sections. The dimensions for these Settings for all five wafers can be found in Table 5-1 and the top down scanning electron microscope (SEM) images in Figure 5-1.

Table 5-1: Dimensions of Settings studied for the first five wafers and the ideal dimensions, with Setting 5 on the left, Setting 11 in the centre, and Setting 15 on the right.

		Setting 5		Setting 11		Setting 15	
	Pillar Height	**Circle Diameter**	**Separ-ation**	**Circle Diameter**	**Separ-ation**	**Circle Diameter**	**Separ-ation**
Ideal	10	18.0	12.0	9.0	6.0	9.0	21.0
90° Pillars	9.6±0.2	17.8±0.2	12.2±0.2	9.6±0.1	5.4±0.1	9.1±0.1	20.9±0.1
80° Pillars	9.2±0.3	18.0±0.1	12.0±0.1	8.9±0.1	6.1±0.1	N/A	N/A
CU Pillars	8.7±0.5	19.3±0.1	10.7±0.1	8.8±0.2	6.2±0.2	8.6±0.3	21.4±0.3
HU Pillars	10.0±0.6	17.3±0.1	12.7±0.1	8.9±0.1	6.1±0.1	8.7±0.2	21.3±0.2
LSG Pillars	8.8±0.3	18.8±0.2	11.2±0.2	9.1±0.1	5.9±0.1	9.0±0.1	21±0.1

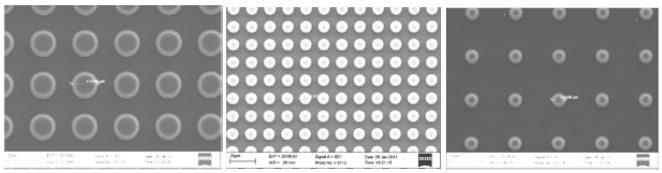

Figure 5-1: SEM images of the Settings studied, with Setting 5 on the left, Setting 11 in the centre, and Setting 15 on the right, with the images taken from the HU pillars. 3000X magnification for all images.

The 90° pillar wafer was the first wafer fabricated and served as the control against which the others were compared. It followed the standard fabrication process and was cryo-etched using the standard recipe, resulting in pillars with smooth, vertical sidewalls, as can be seen in Figure 5-2.

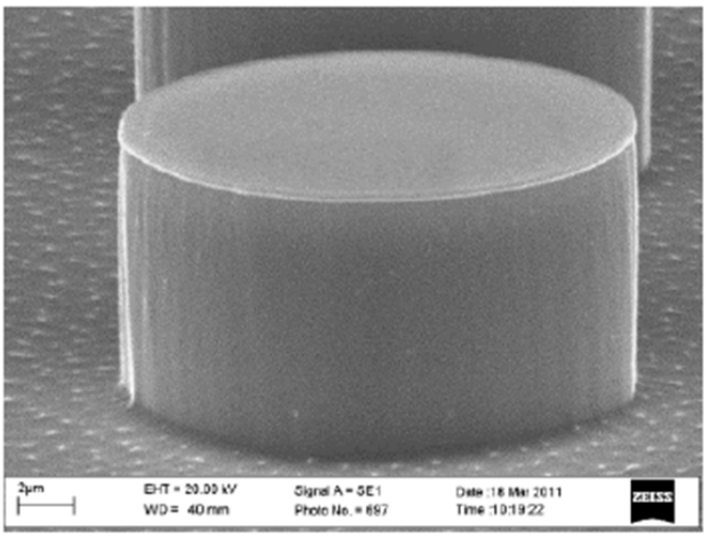

Figure 5-2: SEM image of a 90° pillar taken from Setting 5. 7000X magnification.

For the 80° pillar wafer a variation on the standard cryo-etch was used, whereby the amount of oxygen was reduced by a third, producing a more isotropic etch than normal, generating a slope that trends towards the centre of the pillars, which can be seen in Figure 5-3.

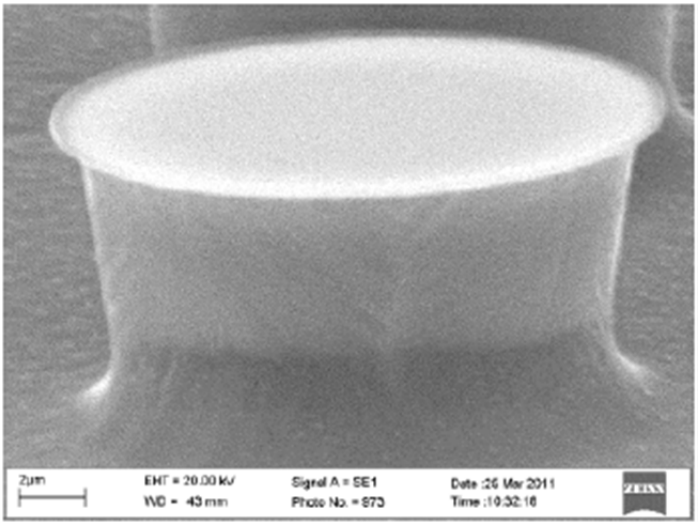

Figure 5-3: SEM image of a 80° pillar taken from Setting 5. 7000X magnification.

The CU pillars were produced using a third variation of the cryo-etch, whereby the oxygen was removed from the process entirely, generating a nearly isotropic etch that removed the silicon beneath the oxide cap except for a thin interior column that supported the cap, as can be seen in Figure 5-4.

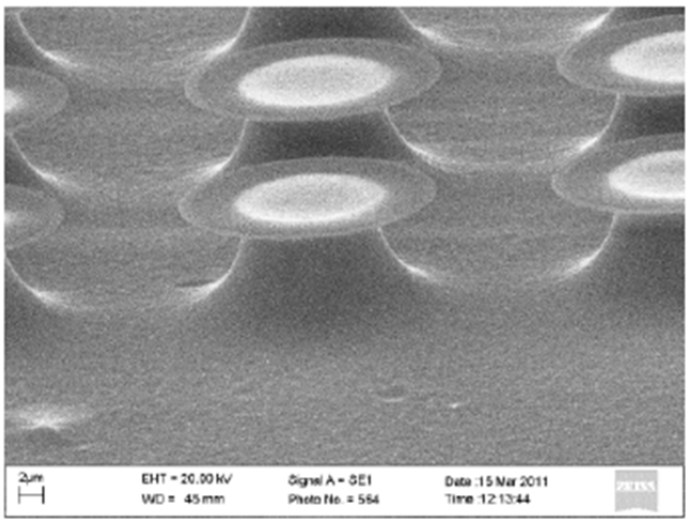

Figure 5-4: SEM image of CU pillars from Setting 5. 7000X magnification.

The HU pillars were an attempt to produce CU pillars using the Bosch process that yielded an interesting undercut geometry. Using a variation on the precision Bosch etch, the C_4F_8 gas was removed for three minutes to generate an isotropic etch before performing seven minutes of standard precision Bosch etching. Instead of generating interior columns that were uniformly less than the top cap, the sidewalls sloped away from the centre before reaching the same diameter as the caps on top, as can be seen in Figure 5-5.

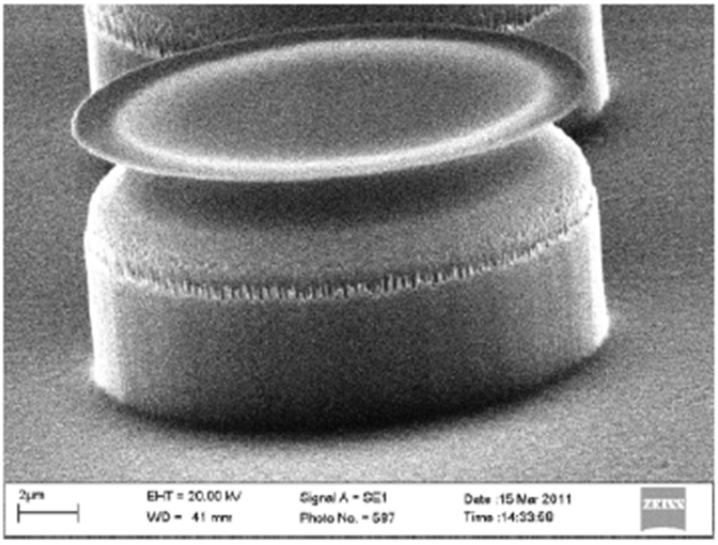

Figure 5-5: SEM image of a HU pillar from Setting 5. 7000X magnification.

After observing the HU pillars under SEM, it was decided to perform a second run of the same process but to remove the silicon dioxide cap afterward so as to produce a pillar with sidewalls at the top of a slope greater than 90°. As the oxide was expected to be removed after, the

photoresist was removed after patterning the oxide layer instead of after etching the silicon as is usual for Bosch processes. Instead of producing smooth pillars as expected, the process generated silicon grass on the tops and sidewalls of the pillars, leading to the structures seen in Figure 5-6.

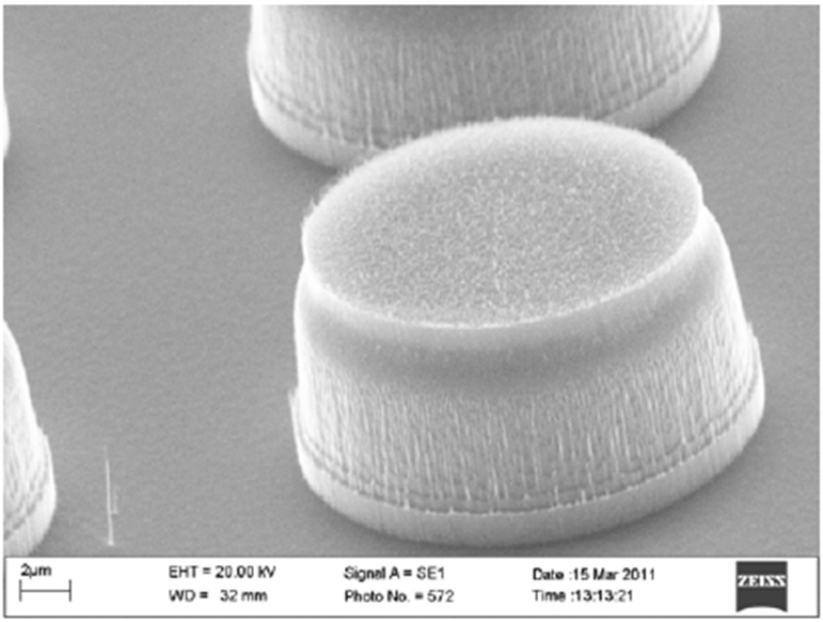

Figure 5-6: SEM image of LSG pillars from Setting 5. 7000X magnification.

Once all of these surfaces were fabricated they were drilled with a diamond tipped bit to produce holes from which a needle could be inserted from the bottom and drops of water could then be grown and receded, giving both advancing and receding CAs. Once the holes were drilled the wafers were given uniform hydrophobicity by exposing them to C_4F_8 plasma in the STS ICP-RIE for 20s, producing a carbon-fluorine polymer similar to Teflon® that was approximately 80 nm thick. When chemically passivated, CA testing proceeded with DI water. The data obtained in these experiments is summarized in Tables 5-2 through 5-6. For comparison, smooth, untextured silicon, coated in the same polymer had an advancing CA of 123±0° and a CAH of 24±1°.

Table 5-2: Contact angle measurements for the 90° pillars with water.

Setting	Advancing CA (°)	Receding CA (°)	CA Hysteresis (°)
5	162±5	142±5	20±7
11	161±3	141±10	20±10
15	155±4	134±4	21±6

Table 5-3: Contact angle measurements for the 80° pillars with water.

Setting	Advancing CA (°)	Receding CA (°)	CA Hysteresis (°)
5	161±3	147±8	14±9
11	162±3	150±6	12±7
15	N/A	N/A	N/A

Table 5-4: Contact angle measurements for the CU pillars with water.

Setting	Advancing CA (°)	Receding CA (°)	CA Hysteresis (°)
5	156±4	150±8	6±9
11	158±5	150±8	8±9
15	133±4	119±8	14±9

Table 5-5: Contact angle measurements for the HU pillars with water.

Setting	Advancing CA (°)	Receding CA (°)	CA Hysteresis (°)
5	164±3	143±4	21±5
11	162±2	148±7	14±10
15	152±6	137±7	15±9

Table 5-6: Contact angle measurements for the LSG pillars with water.

Setting	Advancing CA (°)	Receding CA (°)	CA Hysteresis (°)
5	163±4	152±5	11±6
11	164±3	164±3	0±6
15	155±4	144±5	11±6

As can be seen, all of the wafers exhibited increased water repellency compared to smooth, untextured silicon. The various undercut geometries did not offer a great deal of improved repellence in comparison to the standard 90° pillars. Where the novel designs did show improvement was in the mobility of the water on the surfaces, particularly the LSG wafer where almost no CAH was observed for Setting 11.

Once CA measurement with water was complete, a test with drops of hexadecane (HDEC) was performed. Due to the HDEC's lower surface tension of 27.47mN/m in comparison to water, 72.8mN/m, the drops could not be studied dynamically from a bottom-up orientation, as it would wick back through the hole drilled for the needle instead of forming a drop on the surface. HDEC is also thermodynamically less likely to be in the Cassie state instead of the Wenzel state because of this lowered surface tension, but it was predicted that structures like the CU and HU pillars should have improved repellency. Figure 5-7 and Figure 5-8 show the results of placing HDEC drops on the various surfaces.

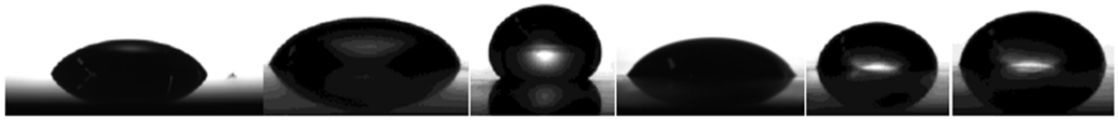

Figure 5-7: From left to right hexadecane drops on coated silicon, 90° Pillars, 80° Pillars, CU Pillars, HU Pillars, and SG Pillars. All pictures taken for Setting 5.

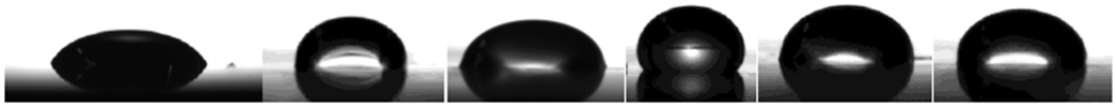

Figure 5-8: From left to right hexadecane drops on coated silicon, 90° Pillars, 80° Pillars, CU Pillars, HU Pillars, and SG Pillars. All pictures taken for Setting 11.

Against expectations the HDEC did not enter into a Cassie state for the majority of the surfaces. However previous observation of HDEC on a surface fabricated with vertical sidewall pillars and a depth of 20 μm, instead of 10 μm, showed that it was possible to produce drops of HDEC that were in the Cassie state. This indicated the possibility that the height of the pillars plays a role.

The extremely high mobility for the LSG was noted and a new wafer was fabricated with the intent to produce silicon grass on the sidewalls. Repeating the removal of photoresist from the wafer, the etching process began with a three minute anisotropic etch, which put a slope on the pillars at the top so that later silicon grass would form on the sidewalls of pillars. Once the anisotropic etch was complete, the wafer was then exposed to a twenty-two minute precision Bosch etch, etching down approximately twenty-two microns, in addition to the initial three. SEM imaging demonstrated that silicon grass had indeed formed, and thus the major silicon grass (MSG) wafer was successfully fabricated. Figure 5-9 shows the various ways in which the silicon was etched, with hollowed out 'crowns' forming at the tops of Settings 1, 3 and 5 while Setting 7 came to a needle sharp point with silicon grass and additional roughness along the sides of all the Settings.

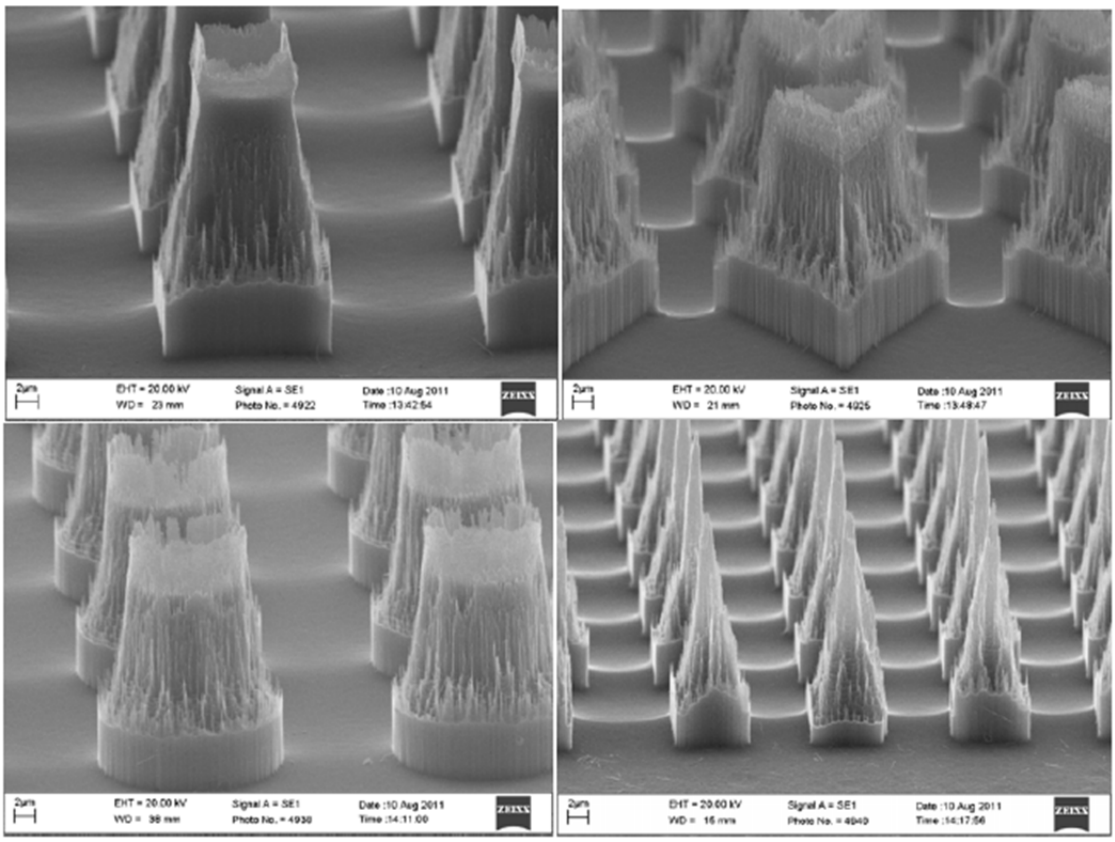

Figure 5-9: Representative SEM images from the MSG wafer. The upper left image is from Setting 1, the upper right from Setting 3, the lower left from Setting 5, and the lower right from setting 7, demonstrating the various ways the silicon was etched. 7000X magnification for all images.

Because of the small size of the silicon grass features, the wafer was chemically passivated using vapour phase trichloro(1H,1H,2H,2H-perfluorooctyl) silane, applied under vacuum in a bell jar. Unlike the previous study, no holes were drilled in this wafer and instead the drops were applied from a top down position. While this prevented the water from pinning on the holes and allowed for the dynamic application of low surface tension liquids, it also made defining the receding angle and the analysis more difficult as the needle was included in any images taken. In the problem of the receding CA, for the MSG wafer, contact line pinning was observed for Setting 1, whereby the contact line never moved and all drop volume change resulted in the CA decreasing. Table 5-7 summarizes the dimensions of the various Settings studied along with their CA behaviour. A smooth silicon surface treated to the same silanization process demonstrated an intrinsic CA with water of 127.2 ± 0.9° with an average CAH of 29.2 ± 12.4°.

Table 5-7: Summary of dynamic CAs for the MSG wafer.

Setting	Shape	Size (μm)	Original Cassie Fraction	Advancing CA (°)	Average Receding CA (°)	Minimum Receding CA (°)	Average CA Hysteresis (°)	Contact Line Pinning
1	Square	16	0.28	128.8±1.1	94.9±20.9	60.3	33.9±20.9	Yes
3	Triangle	24.3	0.28	170.3±1.7	164.2±4.6	156.8	6.0±4.9	No
5	Circle	18	0.28	174.3±1.0	138.4±15.1	121.9	36.0±15.1	No
6	Circle	17	0.25	174.1±1.0	173.3±1.9	166.9	0.7±2.1	No
7	Square	8	0.28	170.7±2.6	142.0±10.2	127.7	28.6±10.5	No
9	Triangle	12.2	0.28	171.2±1.2	169.8±2.1	166.3	1.4±2.4	No
11	Circle	9	0.28	170.7±0.7	169.6±1.9	163.9	1.2±2.1	No

As can be seen, there were two general behaviours, with the water either exhibiting high repellency and low mobility, or high repellency and high mobility. The distinction between the two, appears to be subtle changes in the formation of the silicon grass that can either strongly repel water and allow it to roll off, or can entrap it while still maintaining a high advancing CA.

Due to the extremely high roughness presented by the silicon grass formations, the MSG wafer was also examined for its behaviour with surfactants, with the expectation that it would produce a highly pronounced transition from the Cassie to Wenzel state with increasing surfactant concentration. Testing with surfactants then began, whereby a 20uL droplet was deposited from a top down needle and then the needle was removed. However, it was immediately found that Settings 3, 6, 7, 9, and 11 had such high mobility that the smallest perturbation, such as the removal of the needle from the droplet, was sufficient to send the drops rolling off. This however presented an interesting opportunity in that instead of looking at a surfactant sensor based purely upon contact angle behaviour, there was the possibility that mobility would decrease with increasing surfactant concentration. Solutions of 0, 2, 4, 6, and 8mM sodium dodecyl sulfate (SDS) were applied to the Settings in increasing order of concentration, with the surfaces being cleaned with acetone, ethanol, and DI water in between changing the surfactant solutions. As predicted, increasing concentrations of SDS caused a decrease in contact angle for the cases that did not exhibit roll-off behaviour, while those that did roll off had an abrupt change to droplet pinning at the highest concentration. The initial trial showed two interesting behaviours. The first was that drops, that did not immediately roll off, had a tendency to collapse into the roughness when light mechanical vibration was applied, such as from repositioning the camera. From previous experimentation it was known that the initial drop shape could be metastable in nature, requiring time to reach a lower and more stable contact angle. The second interesting feature was that drops, with lower concentrations of SDS, when applied to the Setting 7 surface, could simultaneously exhibit high mobility and area pinning. In essence, the drop could move around freely within a confined area on the surface but would rebound if it tried to leave this region, unless excessive force was applied, sufficient to eject the drop from the entire region of the Setting. With this information and to confirm the first trial, a second trial was run that included light vibration of pinned drops via manually tapping the edges of the wafer to induce the drops to settle down into a lower energy state. Unfortunately, during application of a drop to

Case 7 the wafer slipped while the needle was in close proximity and the area of interest on the Case was badly scratched, changing the wetting behaviour such that it was excluded from further testing. Figure 5-10 and Figure 5-11 show the contact angle behaviour of the various cases during the two tests. In order to show the transition from roll off behaviour to pinning, if a drop could not remain still on a surface its contact angle was listed as 180°. All concentrations were normalized to the critical micelle concentration (CMC) for SDS of 8mM.

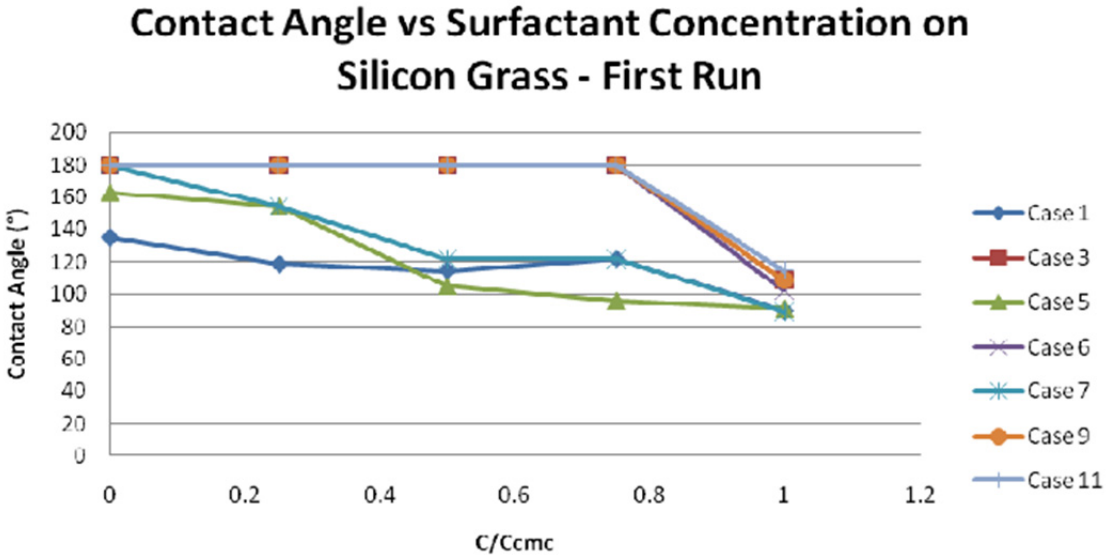

Figure 5-10: The first study of contact angle behaviour for the studied cases in comparison to increasing surfactant concentration. Mechanical agitation was not intentionally applied.

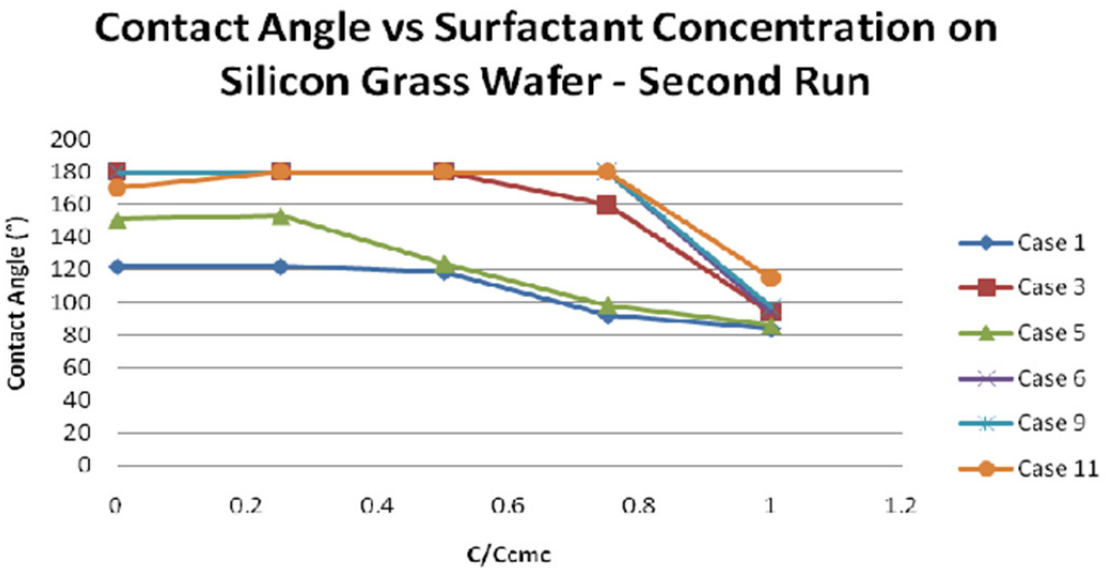

Figure 5-11: The second study of contact angle behaviour for the studied cases in comparison to increasing surfactant concentration. Mechanical agitation was intentionally applied.

While the behaviour is promising, it shows a delay in transition from Cassie to Wenzel with surfactant concentration that falls outside predictions, limiting the ability to tailor behaviour appropriately.

Concurrently with the MSG wafer the surfactant sensor (SS) wafer was also fabricated. This is unrelated to the core of the proposal, but it is thought to share with DND as an interesting off shoot project from the funding provided by DND. Designed with high roughness in mind, it used the second photomask instead of the first. Using standard photolithography processes, it was then cryo-etched using the standard recipe down to a depth of approximately 33µm. Because the cryo-etch is not totally anisotropic, the silicon dioxide mask used formed a cap with a small lip so the silicon dioxide was subsequently etched away and a new uniform layer was grown over the entire surface via standard thermal oxidation process. This oxide layer was formed to allow for better adhesion with octadecyltrichlorosilane (OTS), a chemical chosen for having an intrinsic CA of approximately 105°. However, fabrication did not proceed entirely correctly for some of the Cases due to the photomask not fabricating as originally expected. Case 6, which was intended to have pillar diameters of 5µm and a Cassie fraction of 0.56 completely failed to fabricate as the circles on the mask were too close together, forming the structures seen in Figure 5-12.

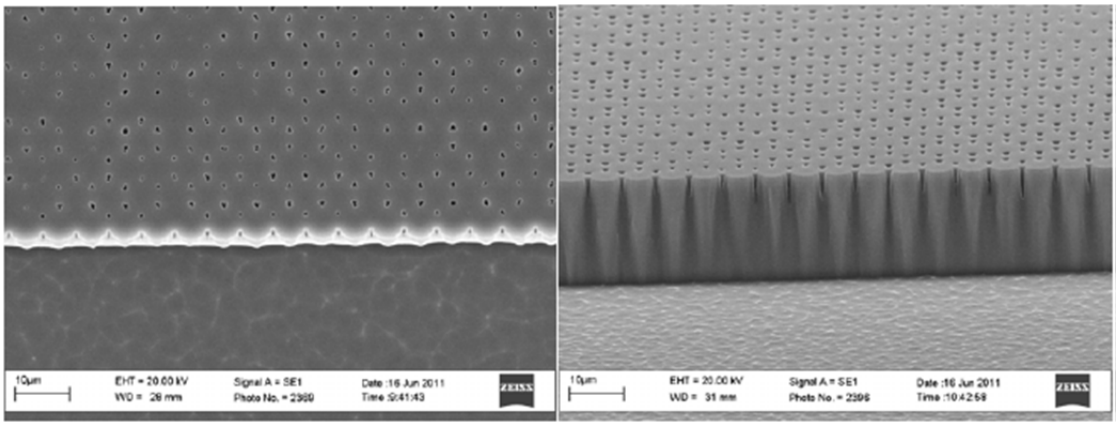

Figure 5-12: SEM images taken of Case 6 and how the pillars failed to form. The left side is a top down view, while the right side is taken from a 70° angle. 5000X magnification

Further inspection by SEM showed that the other patterns had successfully fabricated, but not entirely without difficulty. In particular, the f = 0.56 and d = 10µm pattern has linked pillars present, which can be seen in Figure 5-13, and the 5µm and 10µm pillars for both specified Cassie fractions are larger than desired, also producing larger Cassie fractions than desired. The remaining cases however came in at the correct sizes, and a summary of the expected sizes and Cassie fractions for each case is detailed in Table 5-8. An SEM image of correctly fabricated pillars showing smooth sidewalls is seen in Figure 5-14.

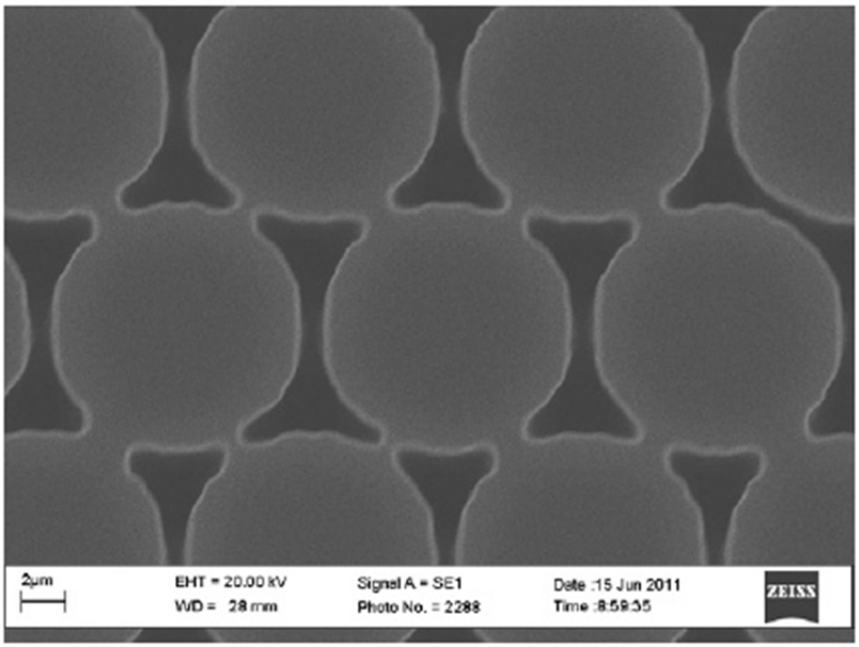

Figure 5-13: Top down SEM image of Case 7 showing how the pillars are linked together. 7000X magnification.

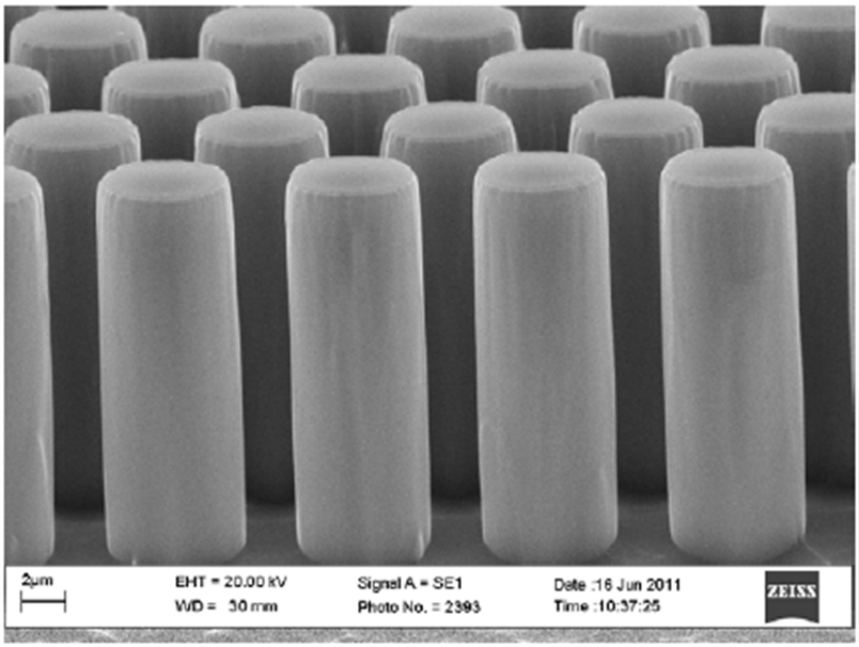

Figure 5-14: SEM image of Case 2 taken at a 70° angle. 7000X magnification.

Table 5-8: Comparison of desired dimensions and measured dimensions for the SS wafer.

	Desired Diameter (µm)	Measured Diameter (µm)	Desired Pillar Spacing (µm)	Measured Pillar Spacing (µm)	Desired Cassie Fraction	Measured Cassie Fraction
Case 1	20	20.0	16	16	0.280	0.280
Case 2	5	6.1	4	2.9	0.280	0.417
Case 3	10	11.6	8	6.4	0.280	0.377
Case 4	15	14.9	12	12.1	0.280	0.276
Case 5	20	20.1	5.35	5.45	0.560	0.566
Case 6	5	N/A	0.56	N/A	0.560	N/A
Case 7	10	11.2	2.73	1.53	0.560	0.702
Case 8	25	25.1	20	19.9	0.280	0.282

After SEM measurements were taken the SS wafer was silanized using OTS and then 30µL samples of 0, 2, 4, 6 and 8mM SDS were then deposited upon all the cases of the sensor, with the exception of Case 6. Figure 5-15 shows the change in contact angle with change in surfactant concentration for the textured cases, while the change in contact angle on the smooth portions of the cases can be seen in Figure 5-16.

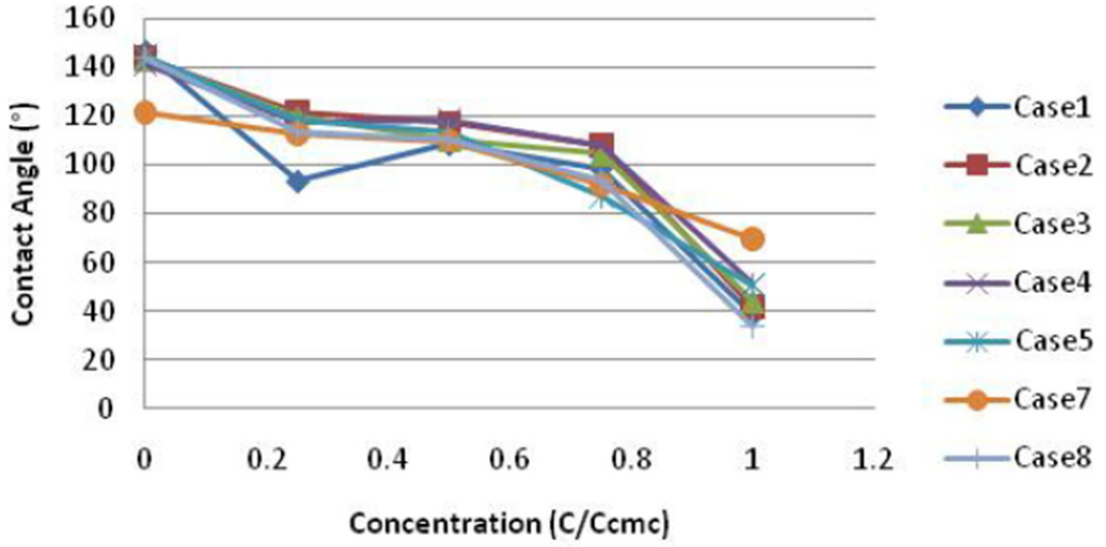

Figure 5-15: All textured cases and the contact angle response to increasing surfactant concentration, with the concentrations normalized to the critical micelle concentration of 8mM.

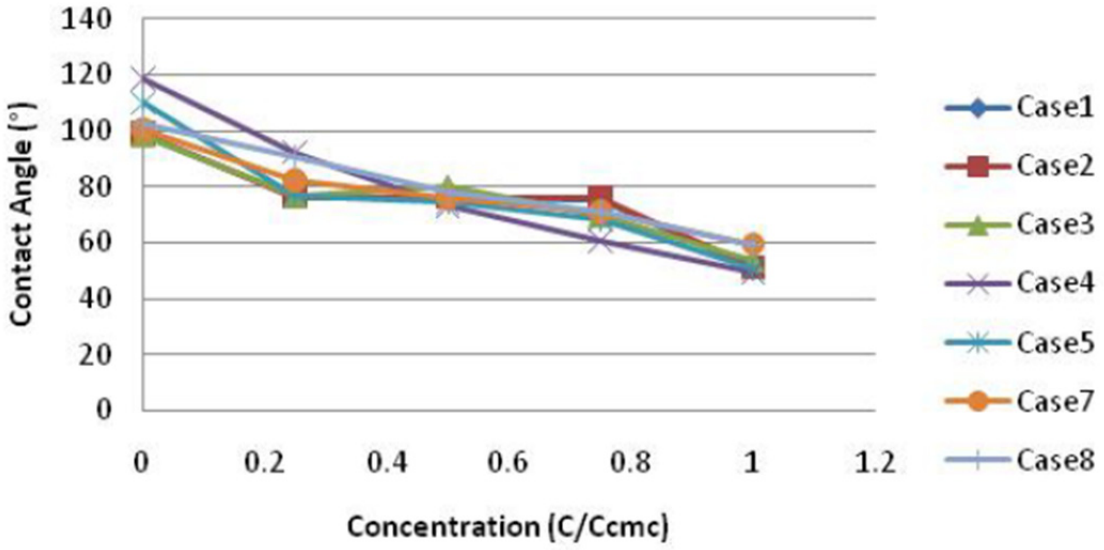

Figure 5-16: All smooth cases and the contact angle response to increasing surfactant concentration, with the concentrations normalized to the critical micelle concentration of 8mM.

While the change in CA demonstrates that there can be a large change in CA as the concentration increases, the majority of the change happened between 6mM and 8mM when the largest change was expected at lower concentrations and the CA never reached 0° as was expected. However, the OTS coating was deemed poor as large formations of undesirable polymer had accumulated and were seen as a possible point of failure. The OTS was removed with an extended oxygen bath in the Branson 3000 Barrel Etcher in the NanoFab and then a layer of fluoro-carbon polymer deposited using the STS ICP-RIE and the experiment repeated, yielding similar results as before but with higher contact angles.

Using the lessons learned in the first study and the second photomask design, a new wafer was fabricated, this one designed to be oleophobic where prior attempts had failed to do so. The variation used for this study applied a precision Bosch etch for 10 minutes, followed by a pure SF_6 plasma for 3 minutes, followed by another 10 minutes of precision Bosch etch. This created micropillar arrays of approximately 23μm in depth with a noticeable undercut geometry. Figure 5-17 shows representative undercut geometries of the pillars fabricated and the fact that there are four identifiable etching regimes. At the top, beneath the silicon dioxide caps the silicon is uneven and slopes inward, towards the centres of the pillars. There is then an abrupt pinch forming a 'waist' followed by smooth sidewalls that slope away from the centres of the pillars. This eventually transitions into another rough section of sidewall with vertically orientated jags while still sloping away from the centre. The final etching regime visible on the pillars is that of smooth, vertical sidewalls aligned with the caps on the pillars. The jagged features in the third etching regime are suspected to be related to silicon grass. Because of its high repellence of oils, this wafer was dubbed the oleophobic (OP) wafer.

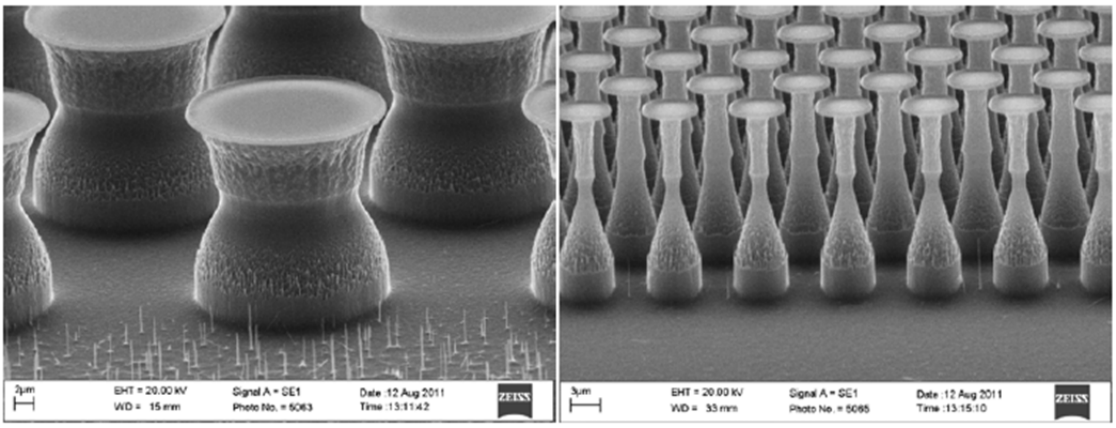

Figure 5-17: SEM images representative of the pillar geometries for the OP wafer. The left side is from Case 1 while the right side is from Case 2. Both images are taken at a 70° angle. 7000X magnification.

Top down observations allowed for the dimensions of the caps on the pillars to be obtained and thus for their Cassie fraction to be calculated. A summary of the measured dimensions is found in Table 5-9.

Table 5-9: Measured dimensions of the tops of the pillars for the OP wafer.

	Desired Diameter (µm)	Measured Diameter (µm)	Desired Pillar Spacing (µm)	Measured Pillar Spacing (µm)	Desired Cassie Fraction	Measured Cassie Fraction
Case 1	20	20.6	16	15.4	0.280	0.297
Case 2	5	6.0	4	3.0	0.280	0.403
Case 3	10	11.1	8	6.9	0.280	0.345
Case 4	15	15.3	12	11.7	0.280	0.291
Case 5	20	20.2	5.35	5.15	0.560	0.571
Case 6	5	N/A	0.56	N/A	0.560	N/A
Case 7	10	10.8	2.73	1.93	0.560	0.653
Case 8	25	25.6	20	19.4	0.280	0.294

Once the SEM work was completed the wafer underwent initial examination for oleophobic behaviour by placing drops of hexadecane (HDEC) and observing general contact angle behaviour. As seen in Figure 5-18, HDEC drops show elevated contact angles and thus the surface can be considered oleophobic. Of note however is the fact that when rolling off the surface the HDEC drops left noticeable trails on the textured portions demonstrating some collapse into the micro-pillar arrays, but after rolling off the textured portions they did not return to those areas despite the liquid being able to make contact with the bottoms and sides of the pillars.

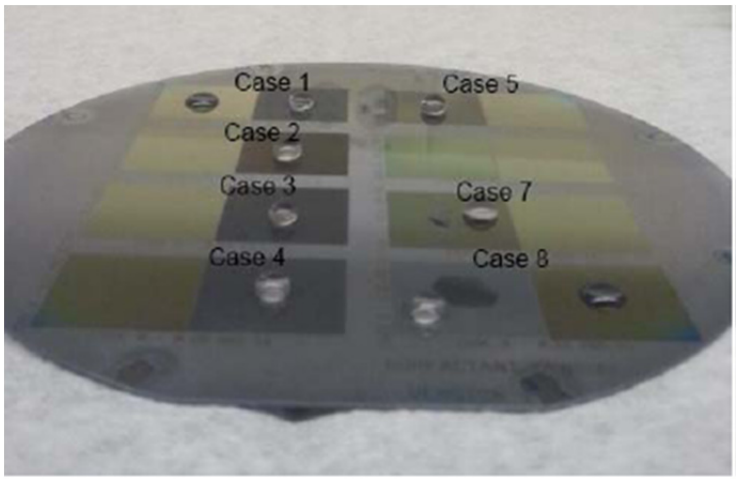

Figure 5-18: Hexadecane drops on the various textured cases of the water, showing their elevated contact angle in comparison to the smooth sections of the surface on the outer portions of the wafer.

With the wafer confirmed to be repellent to HDEC, its contact angle behaviour was examined using water, ethylene glycol (EG) (surface tension 47.7mN/m),[85] and HDEC. The procedure was consistent for all three liquids, with a drop being deposited from a top down position onto the surfaces. For the advancing contact angles this technique obtained consistent results as the drops quickly came to stable values for their contact angle when their volume was increasing, but this was not the case for the receding contact angles where two different behaviours were observed. In the first behaviour the contact angle would decrease while the contact line remained the same until a minimum contact angle was reached, at which point the contact line began to decrease. For the second behaviour the contact line and contact angle decreased continuously and simultaneously throughout the entire process. While the first results in well-defined receding contact angles, the second type of behaviour produces no such well-defined contact angle. The intrinsic contact angle behaviour for the three studied liquids is summarized in Table 5-10.

Table 5-10: Dynamic contact angle measurements for three liquids on smooth surface of the OP wafer.

Liquid	Advancing Contact Angle (°)	Receding Contact Angle (°)	Contact Angle Hysteresis (°)	Receding Well Defined
Water	128.3±1.1	93.0±1.9	35.4±2.2	Yes
Ethylene Glycol	97.7±2.3	63.9±2.2	33.8±3.2	Yes
Hexadecane	79.8±1.0	46.0±4.2	33.8±4.2	Yes

At this point Case 1, 2, and 3 have been fully analyzed and characterized and the contact angle behaviour is summarized in Tables 5-11 through 5-13. While the receding values have a broad distribution, their minimums are also all above 100° and the advancing contact angles of the intrinsic values for their respective liquids.

Table 5-11: Dynamic contact angle measurements for three liquids on Case 1 of the OP wafer.

Liquid	Advancing Contact Angle (°)	Receding Contact Angle (°)	Contact Angle Hysteresis (°)	Receding Well Defined
Water	171.9±2.7	146.5±16.7	25.4±16.9	No
Ethylene Glycol	167.0±1.8	133.4±17.0	33.6±17.0	No
Hexadecane	168.2±2.7	140.1±17.9	28.0±18.1	No

Table 5-12: Dynamic contact angle measurements for three liquids on Case 2 of the OP wafer.

Liquid	Advancing Contact Angle (°)	Receding Contact Angle (°)	Contact Angle Hysteresis (°)	Receding Well Defined
Water	169.3±2.6	122.8±1.5	46.5±3.0	Yes
Ethylene Glycol	158.1±3.1	126.0±16.1	32.0±16.4	No
Hexadecane	158.2±2.2	129±16.9	29.3±17.1	No

Table 5-13: Dynamic contact angle measurements for three liquids on Case 3 of the OP wafer.

Liquid	Advancing Contact Angle (°)	Receding Contact Angle (°)	Contact Angle Hysteresis (°)	Receding Well Defined
Water	170.5±0.8	123.8±1.4	46.8±1.6	Yes
Ethylene Glycol	161.1±1.7	128.9±15.5	32.2±15.5	No
Hexadecane	166.3±1.6	136.6±17.6	29.7±17.6	No

To better illustrate the relationship between contact angle and surface tension, Figure 5-19 graphs the change in the contact angle plotted against the change in surface tension for smooth surfaces and Figures 5-20 through 5-22 show the same relationship for the textured Cases. As can be seen, over the surface tensions studied the intrinsic contact angles behave in a nearly linear fashion while for Case 1 the behaviour is essentially constant, while for Cases 2 and 3 there is a small but significant drop in advancing CA from water to EG, but the CA remains stable from EG to HDEC. However when ethanol with a surface tension of 22.1mN/m[85] is applied to any textured surface on the wafer, total collapse is observed, indicating that there is a steep decline or even switch-like behaviour for at some point for liquids with surface tensions lower than HDEC.

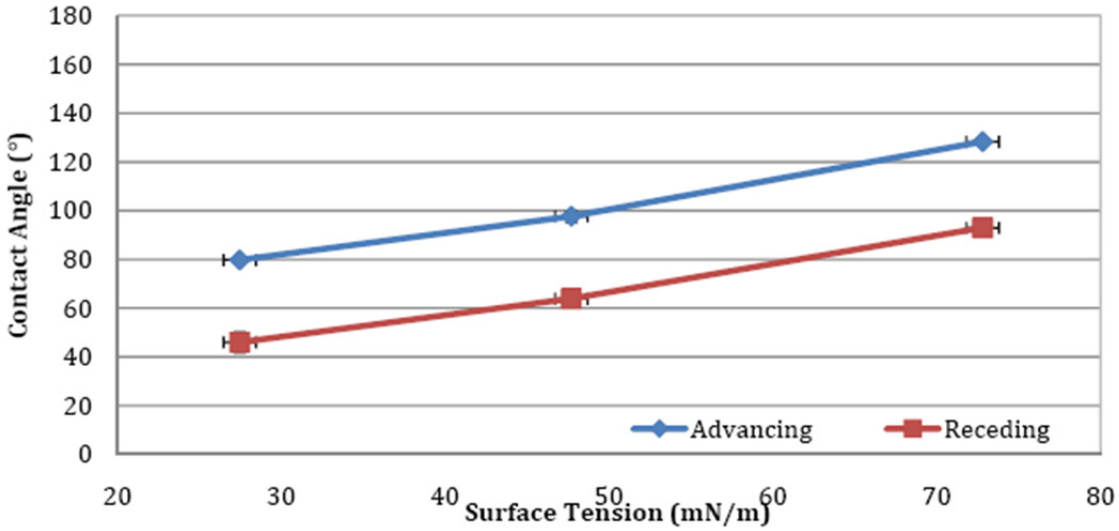

Figure 5-19: Change in contact angle with surface tension on smooth surfaces.

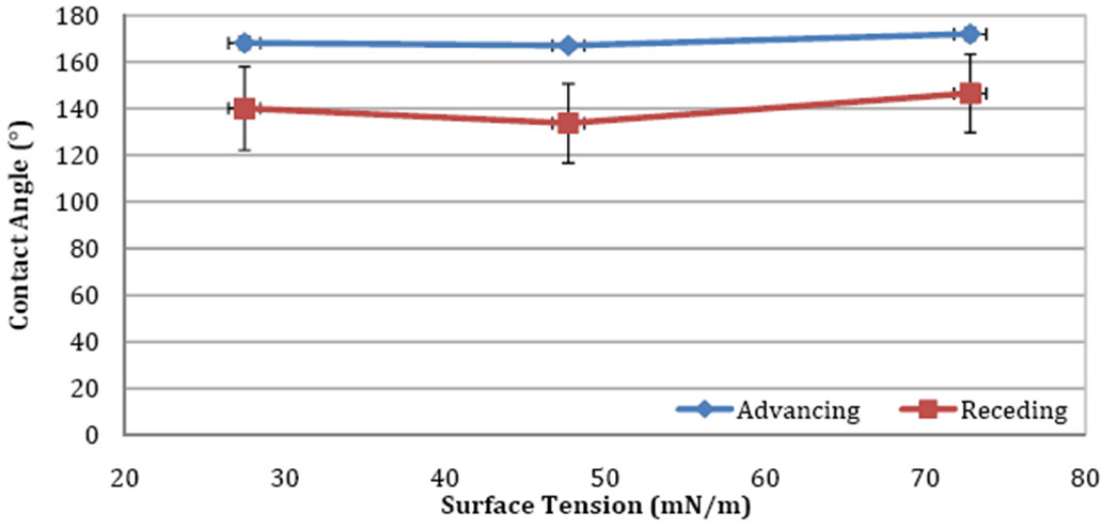

Figure 5-20: Change in contact angle with surface tension on Case 1 of OP wafer.

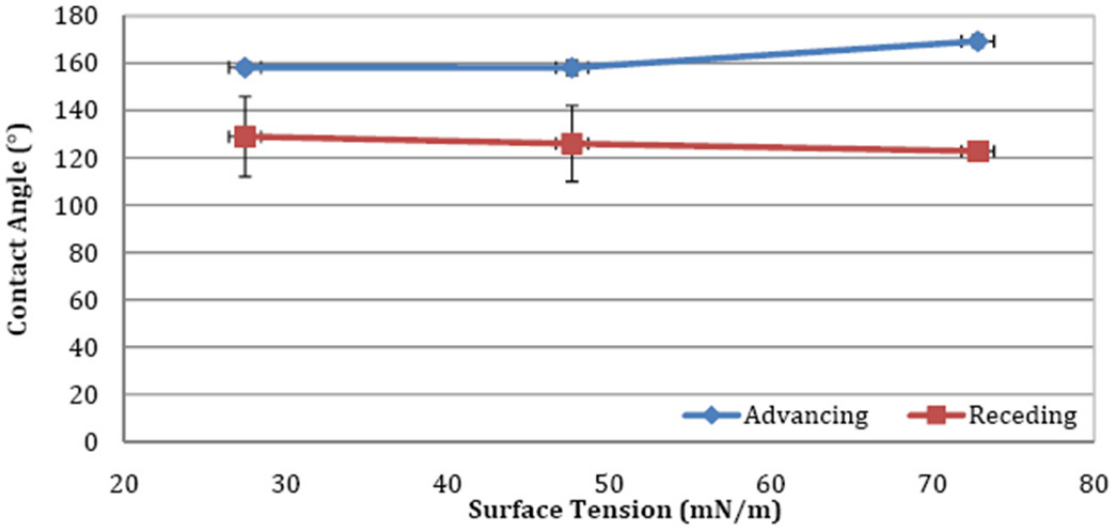

Figure 5-21: Change in contact angle with surface tension on Case 2 of OP wafer.

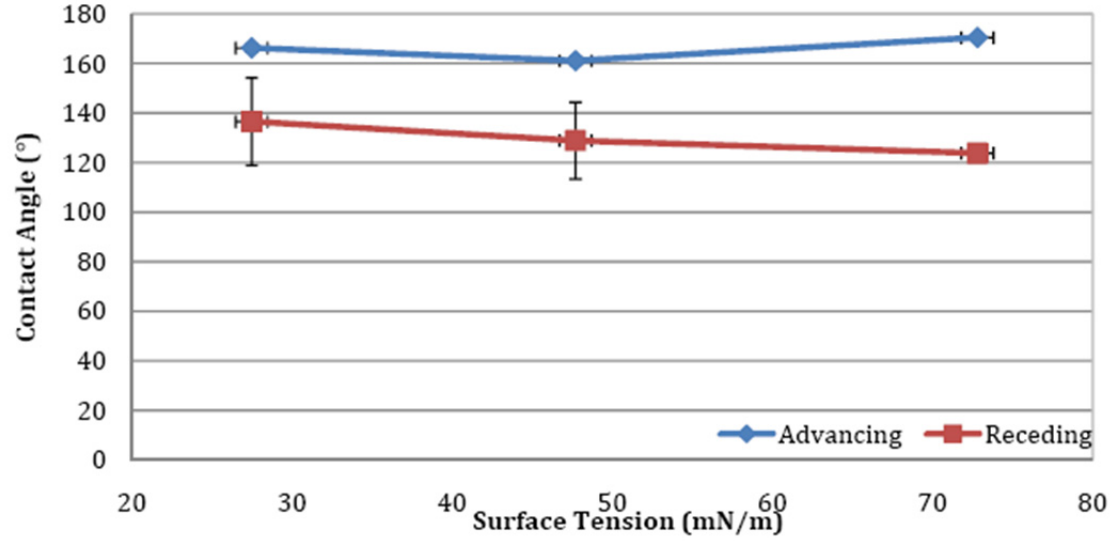

Figure 5-22: Change in contact angle with surface tension on Case 3 of OP wafer.

5.5 Future Work

With the recipes for the MSG wafer and the OP showing that they produce the results expected, further work can be done to refine these processes to produce better quality oleophobic surfaces and silicon grass. Use of silicon on insulator type wafers also allows for the possibility of combining the MSG and OP geometries in an attempt to combine the high repellency against oils of the OP wafer with the high mobility of the LSG and MSG wafer. A new generation of photomask design is also needed to correct the errors present in the mask used for the SS and OP

wafers. Multilayer photomask design and exploitation of the same etch selectivity between silicon and silicon dioxide used to produce the LSG and MSG could be used to produce 'cup' pillars featuring a pillar with an interior depression etched to a lesser depth than the exterior of the pillar that could feature high repellency but extremely low mobility, pinning fluids or microscopic particles on the tops of the pillars.

Publications

The work performed during the course of the current reporting period (year two), has also lead to the publication and presentation of the following work:

Journal Publications

- D. Barona and A. Amirfazli, "Producing a superhydrophobic paper and altering its repellency through ink-jet printing," Lab on a Chip, vol. 11, no. 5, p. 936-940, Jan. 2011.

Conference Papers

- D. Barona, A. Amirfazli "A robust Superhydrophobic Surface for Digital Microfluidics", ASME- ICNMM2011, Jun 19-22, Edmonton, Canada, 2011.

Conference Presentations

- M. Singh, D. Barona, A. Amirfazli, "Wetting Performance of Worn Superhydrophobic Surfaces" ASME Applied Mechanics and Materials Conference, McMAT-2011, Chicago, USA, May 31 to June 2, 2011.
- G. Fang, A. Amirfazli, "Contact Angle Phenomenon at Sharp Edges: A Thermodynamic Approach", 241st ACS Nat. Meeting, Anaheim, USA, Mar. 27-31, 2011.
- D. Barona and A. Amirfazli, "Enabling Lab-on-paper Devices Through Producing a Superhydrophobic Paper and Altering its Wetting Properties Using Ink-jet Printing" SIS 2010, Melbourne, Australia, Nov 14-19, 2010. INVITED TALK

References

[1] Emerson, W. W. Journal of Soil Science 1962, 13, 31-39.

[2] Ravina, I.; Low, P. Clays and Clay Minerals 1977, 25, 201.

[3] Soundararajah, Q. Y.; Karunaratne, B. S. B.; Rajapakse, R. M. G. Materials Chemistry and Physics 2009, 113, 850-855.

[4] Ravina, I.; Low, P. F. Clays and Clay Minerals 1972, 20, 109–123.

[5] Lyons, W. Standard handbook of petroleum & natural gas engineering; Gulf Professional Pub.: Burlington, MA ; Oxford, UK :, 2005.

[6] Lee, W.; Yang, L. Journal of Applied Polymer Science 2004, 92, 3422-3429.

[7] Zimmermann, J.; Reifler, F. A.; Fortunato, G.; Gerhardt, L.; Seeger, S. Advanced Functional Materials 2008, 18, 3662-3669.

[8] Xiu, Y.; Liu, Y.; Hess, D. W.; Wong, C. P. Nanotechnology 2010, 21, 155705.

[9] Yanagisawa, T.; Nakajima, A.; Sakai, M.; Kameshima, Y.; Okada, K. Materials Science and Engineering: B 2009, 161, 36-39.

[10] Hansson, P. M.; Skedung, L.; Claesson, P. M.; Swerin, A.; Schoelkopf, J.; Gane, P. A. C.; Rutland, M. W.; Thormann, E. Langmuir 2011, 27, 8153-8159.

[11] Deng, X.; Mammen, L.; Zhao, Y.; Lellig, P.; Müllen, K.; Li, C.; Butt, H.; Vollmer, D. Advanced Materials 2011, 23, 2962-2965.

[12] Minko, S.; Müller, M.; Motornov, M.; Nitschke, M.; Grundke, K.; Stamm, M. Journal of the American Chemical Society 2003, 125, 3896-3900.

[13] ASTM International ASTM Standard F735-06, 2003 - Standard Test Method for Abrasion Resistance of Transparent Plastics and Coatings Using the Oscillating Sand Method 2003.

[14] Oliver, J. F.; Huh, C.; Mason, S. G. Journal of Colloid and Interface Science 1977, 59, 568-581.

[15] Extrand, C. W. Langmuir 2005, 21, 10370-10374.

[16] Tóth, T.; Ferraro, D.; Chiarello, E.; Pierno, M.; Mistura, G.; Bissacco, G.; Semprebon, C. Langmuir 2011, 27, 4742-4748.

[17] Pan, Q.; Wang, M. ACS Applied Materials & Interfaces 2009, 1, 420-423.

[18] Zhang, J.; Wang, J.; Zhao, Y.; Xu, L.; Gao, X.; Zheng, Y.; Jiang, L. Soft Matter 2008, 4, 2232.

[19] Genzer, J.; Efimenko, K. Biofouling 2006, 22, 339-360.

[20] Koch, K.; Bhushan, B.; Barthlott, W. Progress in Materials Science 2009, 54, 137-178.

[21] Koch, K.; Bhushan, B.; Barthlott, W. Soft Matter 2008, 4, 1943.

[22] Zhao, Y.; Lu, Q.; Li, M.; Li, X. Langmuir 2007, 23, 6212-6217.

[23] Chen, Y.; He, B.; Lee, J.; Patankar, N. A. Journal of Colloid and Interface Science 2005, 281, 458-464.

[24] Sandre, O.; Gorre-Talini, L.; Ajdari, A.; Prost, J.; Silberzan, P. Phys. Rev. E 1999, 60, 2964.

[25] Zhu, L.; Feng, Y.; Ye, X.; Zhou, Z. Sensors and Actuators A: Physical 2006, 130-131, 595-600.

[26] Shastry, A.; Case, M. J.; Böhringer, K. F. Langmuir 2006, 22, 6161-6167.

[27] Su, Y.; Ji, B.; Zhang, K.; Gao, H.; Huang, Y.; Hwang, K. Langmuir 2010, 26, 4984-4989.

[28] Cheng, Z.; Gao, J.; Jiang, L. Langmuir 2010, 26, 8233-8238.

[29] Lai, Y.; Gao, X.; Zhuang, H.; Huang, J.; Lin, C.; Jiang, L. Advanced Materials 2009, 21, 3799-3803.

[30] Liu, K.; Yao, X.; Jiang, L. Chemical Society Reviews 2010, 39, 3240.

[31] Roach, P.; Shirtcliffe, N. J.; Newton, M. I. Soft Matter 2008, 4, 224.

[32] Quéré, D. Annual Review of Materials Research 2008, 38, 71-99.

[33] Pierce, E.; Carmona, F.; Amirfazli, A. Colloids and Surfaces A: Physicochemical and Engineering Aspects 2008, 323, 73-82.

[34] Barthlott, W.; Neinhuis, C. Planta 1997, 202, 1-8.

[35] NEINHUIS, C.; BARTHLOTT, W. Annals of Botany 1997, 79, 667 -677.

[36] Koch, K.; Bhushan, B.; Jung, Y. C.; Barthlott, W. Soft Matter 2009, 5, 1386.

[37] Koch, K.; Bohn, H. F.; Barthlott, W. Langmuir 2009, 25, 14116-14120.

[38] Zheng, Y.; Gao, X.; Jiang, L. Soft Matter 2007, 3, 178.

[39] Lee, W.; Jin, M.-K.; Yoo, W.-C.; Lee, J.-K. Langmuir 2004, 20, 7665-7669.

[40] Gao, X.; Jiang, L. Nature 2004, 432, 36.

[41] Hu, D. L.; Chan, B.; Bush, J. W. M. Nature 2003, 424, 663-666.

[42] Feng, X.-Q.; Gao, X.; Wu, Z.; Jiang, L.; Zheng, Q.-S. Langmuir 2007, 23, 4892-4896.

[43] Gao, X.; Yan, X.; Yao, X.; Xu, L.; Zhang, K.; Zhang, J.; Yang, B.; Jiang, L. Advanced Materials 2007, 19, 2213-2217.

[44] Kurogi, K.; Yan, H.; Tsujii, K. Colloids and Surfaces A: Physicochemical and Engineering Aspects 2008, 317, 592-597.

[45] Herminghaus, S.; Brinkmann, M.; Seemann, R. Annual Review of Materials Research 2008, 38, 101-121.

[46] Dorrer, C.; Rühe, J. Langmuir 2006, 22, 7652-7657.

[47] Dorrer, C.; Rühe, J. Langmuir 2007, 23, 3179-3183.

[48] Yoshimitsu, Z.; Nakajima, A.; Watanabe, T.; Hashimoto, K. Langmuir 2002, 18, 5818-5822.

[49] Li, W.; Fang, G.; Li, Y.; Qiao, G. The Journal of Physical Chemistry B 2008, 112, 7234-7243.

[50] Semprebon, C.; Mistura, G.; Orlandini, E.; Bissacco, G.; Segato, A.; Yeomans, J. M. Langmuir 2009, 25, 5619-5625.

[51] Patankar, N. A. Langmuir 2004, 20, 7097-7102.

[52] He, B.; Patankar, N. A.; Lee, J. Langmuir 2003, 19, 4999-5003.

[53] Sbragaglia, M.; Peters, A. M.; Pirat, C.; Borkent, B. M.; Lammertink, R. G. H.; Wessling, M.; Lohse, D. Phys. Rev. Lett. 2007, 99, 156001.

[54] Tuteja, A.; Choi, W.; Ma, M.; Mabry, J. M.; Mazzella, S. A.; Rutledge, G. C.; McKinley, G. H.; Cohen, R. E. Science 2007, 318, 1618 -1622.

[55] Ahuja, A.; Taylor, J. A.; Lifton, V.; Sidorenko, A. A.; Salamon, T. R.; Lobaton, E. J.; Kolodner, P.; Krupenkin, T. N. Langmuir 2008, 24, 9-14.

[56] Marmur, A. Langmuir 2008, 24, 7573-7579.

[57] Im, M.; Im, H.; Lee, J.-H.; Yoon, J.-B.; Choi, Y.-K. Soft Matter 2010, 6, 1401.

[58] Cao, L.; Hu, H.-H.; Gao, D. Langmuir 2007, 23, 4310-4314.

[59] Liu, J.-L.; Feng, X.-Q.; Wang, G.; Yu, S.-W. Journal of Physics: Condensed Matter 2007, 19, 356002.

[60] Ma, Y.; Cao, X.; Feng, X.; Ma, Y.; Zou, H. Polymer 2007, 48, 7455-7460.

[61] Tuteja, A.; Choi, W.; McKinley, G. H.; Cohen, R. E.; Rubner, M. F. MRS Bulletin 2008, 33, 752-758.

[62] Karlsson, M.; Forsberg, P.; Nikolajeff, F. Langmuir 2010, 26, 889-893.

[63] Leng, B.; Shao, Z.; de With, G.; Ming, W. Langmuir 2009, 25, 2456-2460.

[64] Wang, J.; Liu, F.; Chen, H.; Chen, D. Applied Physics Letters 2009, 95, 084104.

[65] Oliver, J. F.; Huh, C.; Mason, S. G. The Journal of Adhesion 1976, 8, 223-234.

[66] Oliver, J.; Mason, S. Journal of Colloid and Interface Science 1977, 60, 480–487.

[67] Oliver, J. P.; Huh, C.; Mason, S. G. Colloids and Surfaces 1980, 1, 79-104.

[68] Bayramli, E.; Mason, S. Journal of Colloid and Interface Science 1978, 66, 200–202.

[69] Mori, Y. H.; van de Ven, T. G. M.; Mason, S. G. Colloids and Surfaces 1982, 4, 1-15.

[70] Dyson, D. C. Physics of Fluids 1988, 31, 229.

[71] Zhang, J.; Gao, X.; Jiang, L. Langmuir 2007, 23, 3230-3235.

[72] Berthier, J.; Loe-Mie, F.; Tran, V.-M.; Schoumacker, S.; Mittler, F.; Marchand, G.; Sarrut, N. Journal of Colloid and Interface Science 2009, 338, 296-303.

[73] Sheng, X.; Zhang, J.; Jiang, L. Langmuir 2009, 25, 9903-9907.

[74] Kalinin, Y. V.; Berejnov, V.; Thorne, R. E. Langmuir 2009, 25, 5391-5397.

[75] Scientific papers: Gibbs, J. Willard (Josiah Willard), 1839-1903 : Free Download & Streaming : Internet Archive.

[76] Wang, J.; Chen, D. Langmuir 2008, 24, 10174-10180.

[77] Ondarçuhu, T.; Piednoir, A. Nano Letters 2005, 5, 1744-1750.

[78] Extrand, C. W.; Moon, S. I. Langmuir 2008, 24, 9470-9473.

[79] Kalinin, Y.; Berejnov, V.; Thorne, R. E. Microfluidics and Nanofluidics 2008, 5, 449-454.

[80] Du, J.; Michielsen, S.; Lee, H. J. Langmuir 2010, 26, 16000-16004.

[81] Nosonovsky, M.; Bhushan, B. Nano Letters 2007, 7, 2633-2637.

[82] Applied surface thermodynamics; M. Dekker: New York, 1996.

[83] Long, J.; Hyder, M. N.; Huang, R. Y. M.; Chen, P. Advances in Colloid and Interface Science 2005, 118, 173-190.

[84] Stubenrauch, M.; Fischer, M.; Kremin, C.; Stoebenau, S.; Albrecht, A.; Nagel, O. Journal of Micromechanics and Microengineering 2006, 16, S82.

[85] Surface tension values of some common test liquids for surface energy analysis http://www.surface-tension.de/.

[86] Amirfazli, A., Superomniphobic Surfaces for Military Applications: Nano- and Micro-Fabrication Methods. Chapter 1: Lithographic Fabrication of Surfaces with Different Microgeometries and Investigation of Their Wetting Behaviour, DRDC Atlantic CR 2010-329, December 2010.

[87] Amirfazli, A., Superomniphobic Surfaces for Military Applications: Nano- and Micro-Fabrication Methods. Chapter 2: Investigation of Wear for Superhydrophobic Surfaces and Development of New Coatings, DRDC Atlantic CR 2010-315, December 2010.

[88] D. Barona and A. Amirfazli, "Producing a Superhydrophobic Paper and Altering its Repellency Through Ink-jet Printing," Lab on a Chip, vol. 11, no. 5, p. 936, Jan. 2011.

[89] D. Barona, A. Amirfazli "A Robust Superhydrophobic Surface for Digital Microfluidics", ASME- ICNMM2011, Jun 19-22, Edmonton, Canada, 2011.

[90] C. Extrand, Langmuir, 20, 5013-5018, 2004

[91] C. Extrand, Langmuir, 18, 7991-7999, 2002.

[92] L. Gao, T.J. McCarthy, Langmuir, 23, 3762-3765, 2007.

Annex A SEM Images for different Curing Techniques

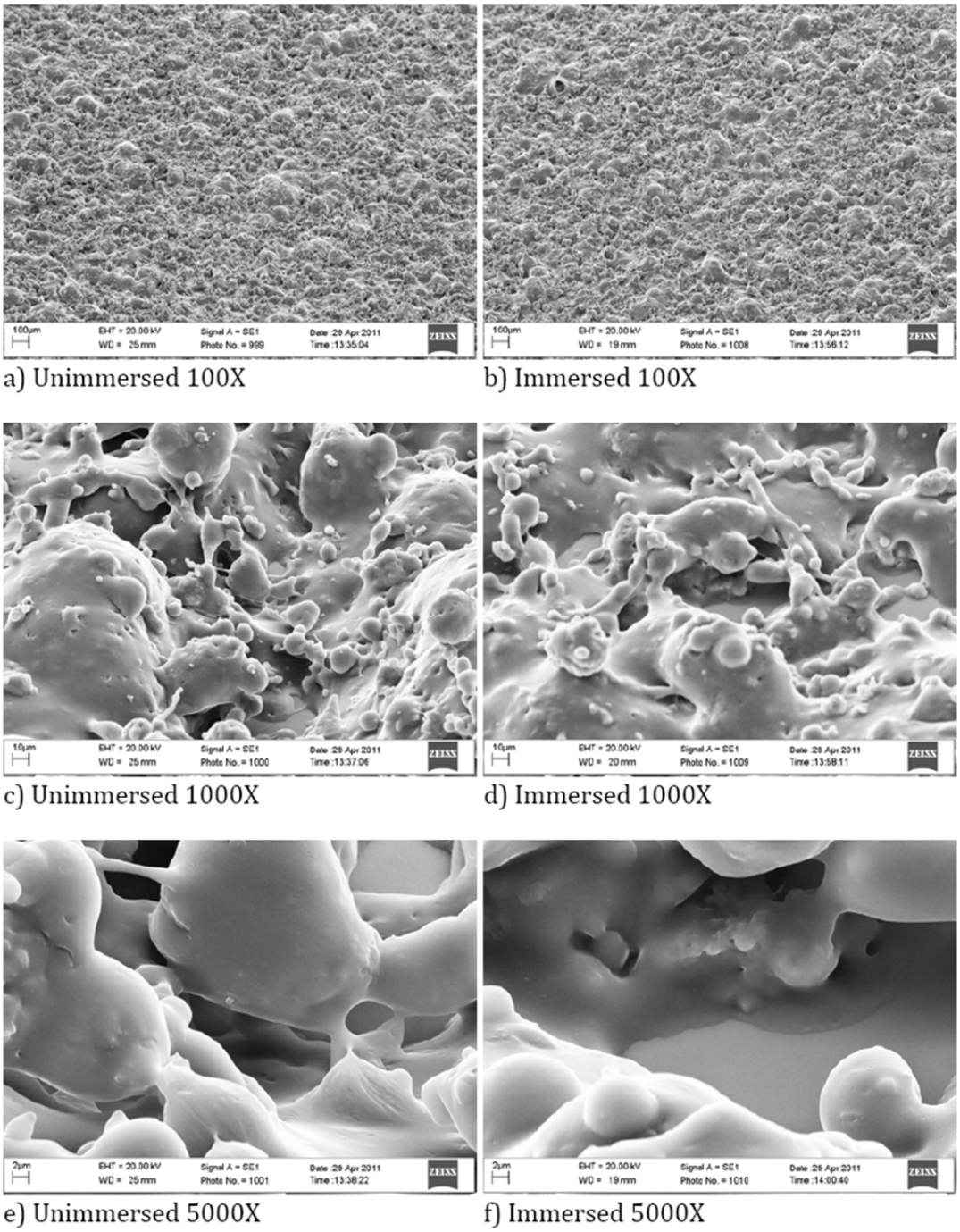

Figure A-1: SEM images of SH coating treated glass samples cured at Room Temperature (21°C) for 17 hours and immersed for 24 hours.

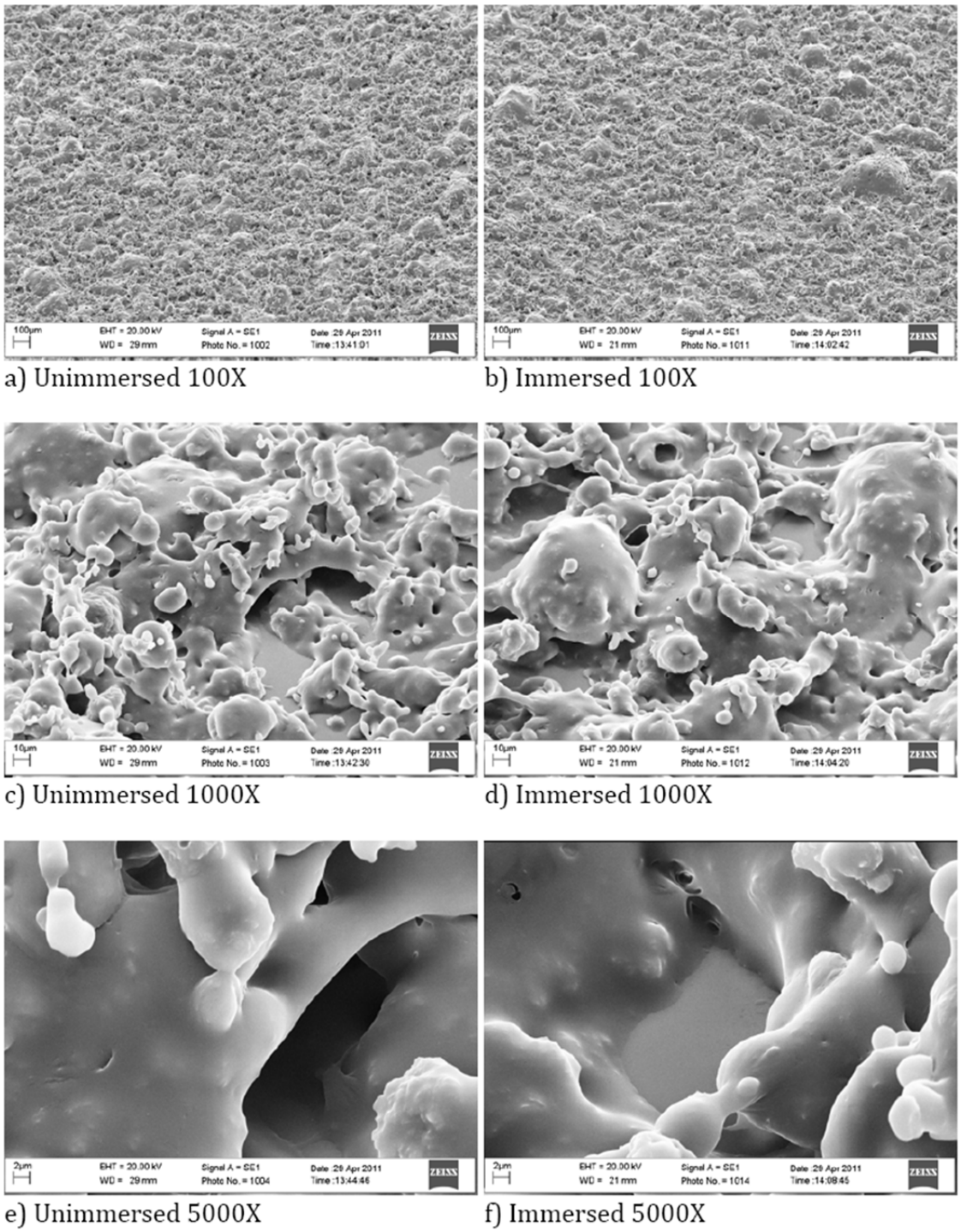

Figure A-2: SEM images of SH coating treated glass samples cured at in vacuum at 75°C for 3 hours followed by curing at ambient pressure and room temperature for 14 hours then immersed for 24 hours.

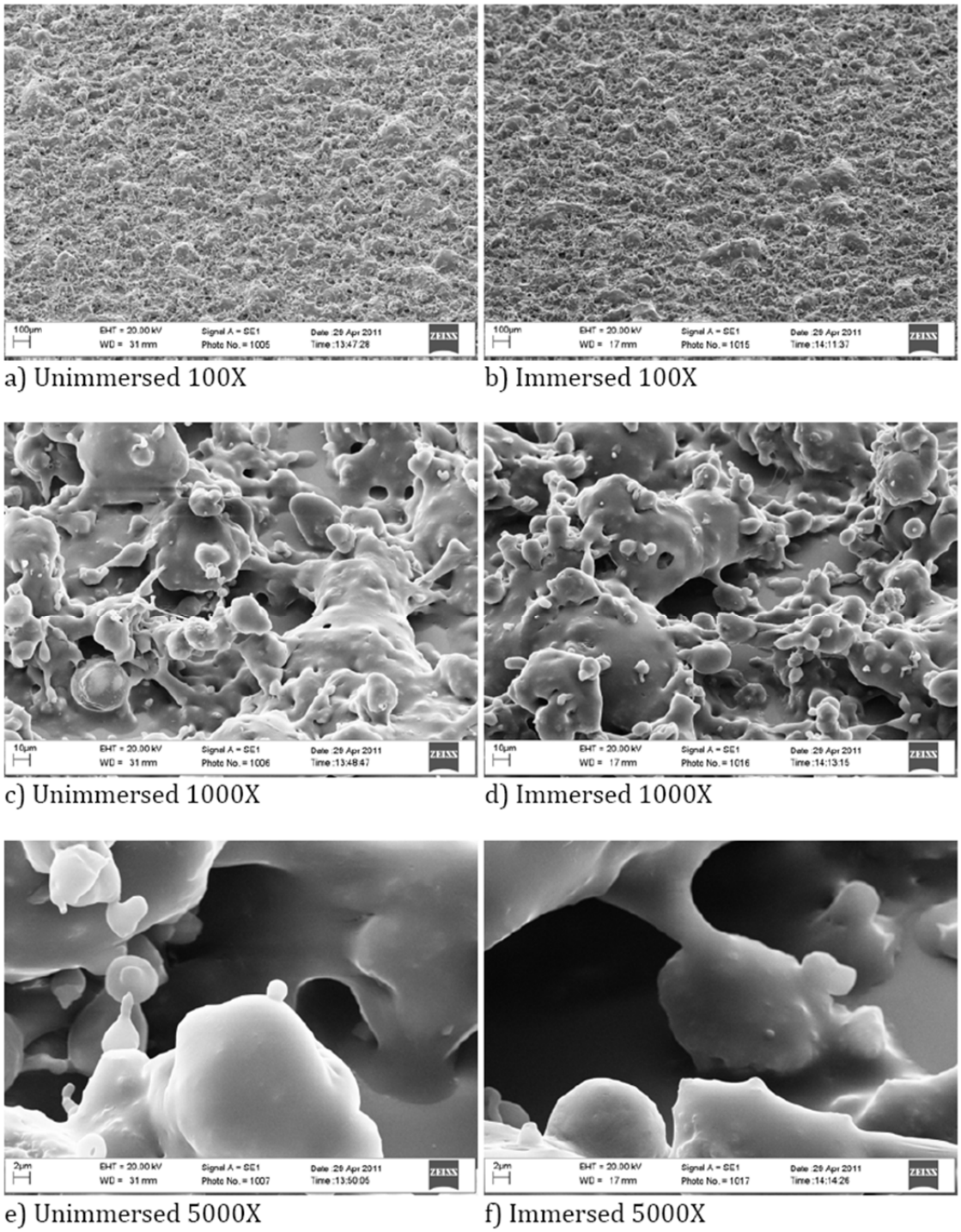

Figure A-3: SEM images of SH coating treated glass samples cured at room temperature (21°C) 3 hours followed by curing at ambient pressure and 75°C for 14 hours then immersed for 24 hours.

This page intentionally left blank.

Annex B A Thermodynamic Approach for Understanding the Edge Effect on Wetting: Supplementary Information for Section 3

To show the validation of the thermodynamic model, FE curves illustrating cases A, B and C, mentioned in the paper of Oliver et al.,[14] are given and explained, correspondingly.

Figure B-1a shows the FE curves for drop with increasing drop volume sitting on a single pillar (θ_Y=80°, L_A=0.001 m) with edge angle Φ = 60° (< θ_Y = 80°) which satisfies the condition of case A ($\Phi \leq \theta_Y$). When the drop volume is small (FE curve 1), the minimum FE state is on the dotted line part (the drop FE states for drops at positions B), indicating that the drop three phase contact line (TPCL) is still away from the pillar edge and thus it looks like that the drop spreading behaviour is happening on an ideally smooth surface with showing an equilibrium CA (= θ_Y = 80°) (see Figure B-1b); note that the solid line part (the drop FE states at positions C) is not available for FE curve 1 because the criterion eq 8 is violated (it is the same for the cases below if the solid line part of the FE curve is not available). If the drop volume increases to a critical value (FE curve 2), the minimum FE state will be at the reference position A (i.e. the pillar edge), indicating that the most stable TPCL has reached the pillar edge. Moreover, the minimum FE state will be staying at the reference position A with further increase of drop volume (FE curve 3 to curve 8), indicating that the most stable drop TPCL will be pinned at the pillar edge while the drop equilibrium CA approaches but never reaches θ_C (>=180°). The result is consistent with the drop spreading behaviour of case A described by Oliver et al..[14]

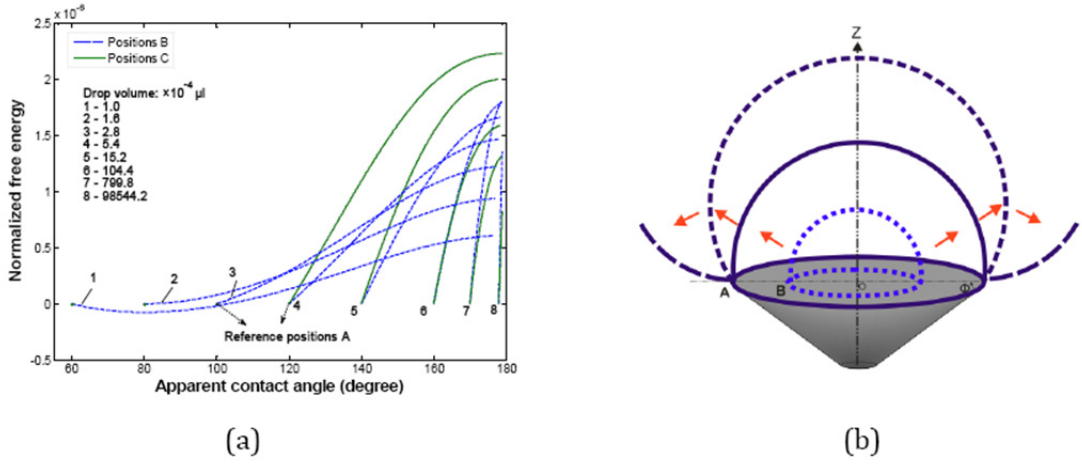

Figure B-1: (a) Comparison of variations of normalized FE with apparent CA for various drop volumes (θ_Y=80°, L_A=0.001m, θ_A=60-160°, Φ=60°). (b) Schematic showing the drop spreading behaviour in wetting case A.

Figure B-2a shows the FE curves for a drop with increasing drop volume sitting on a single pillar (θ_Y=80°, L_A=0.001 m) with edge angle Φ = 120° which satisfies the condition of case B ($\Phi > \theta_Y$ & $\Phi > \theta_Y + 2atan(0.5cot\ \theta_Y)$). Here, the statements for FE curves 1 and 2 are not repeated

because they are similar to the cases in Figure B-1. As the TPCL reaches the pillar edge, the minimum FE state will remain at the reference position A with further increase of drop volume (FE curve 3 to curve 5), indicating that the most stable drop TPCL will be pinned at the pillar edge while the equilibrium CA approaches θ_C *(=* θ_Y *+ (180°-* Φ*) =140°*). After the drop equilibrium CA reaches θ_C (=140°), the minimum FE state will move to the solid line part (FE state for drop at positions C) and the equilibrium CA will keep constant at θ_C (=140°) with further increase of drop volume; i.e., a drop collapse will take place and the TPCL will move steadily over the edge onto the sidewall. The result is consistent with the drop spreading behaviour of case B described by Oliver et al..[14]

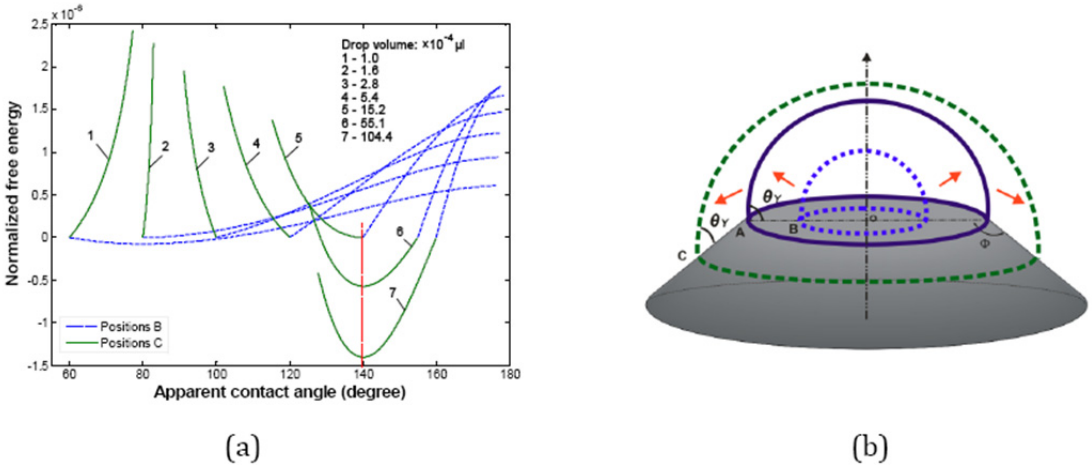

Figure B-2: (a) Comparison of variations of normalized FE with apparent CA for various drop volumes (θ_Y=80°, L_A=0.001 m, θ_A=40-160°, Φ=120°). (b) Schematic showing the drop spreading behaviour in wetting case B.

Figure B-3a shows the FE curves for drop with increasing drop volume sitting on a single pillar (θ_Y=80°, L_A = 0.001m) with edge angle Φ = 85° which satisfies the condition of case C ($\theta_Y < \Phi < \theta_Y + 2atan(0.5cot\ \theta_Y)$). Again, the statement for FE curves 1 and 2 is not repeated. As the TPCL reaches the pillar edge, the minimum FE state remains at the reference position A with further increase of drop volume (FE curve 3 to curve 8), indicating that the most stable drop TPCL will be pinned at the pillar edge while the equilibrium CA approaches θ_C *(=* θ_Y *+ (180°-* Φ*) =175°*). It is noted that the FE curve for the solid line part becomes a convex shape after curve 7, indicating that a FE barrier exists (see the enlargement). It also shows that the increase of the drop volume will decrease the FE barrier. Thus, the drop may collapse if the FE barrier is overcome under the help of external energy from sources such as mechanical vibration. After the equilibrium CA reaches θ_C (=175°), there is no longer a minimum FE state existing, resulting in an immediate drop collapse. However, unlike case B, the TPCL cannot move steadily over the edge, since the pillar edge will touch the drop cap and split it into two parts (one part remaining on top of the pillar while the other part is on the pillar sidewall), see Figure B-3b. The result is consistent with the drop spreading behaviour of case C described by Oliver et al..[14]

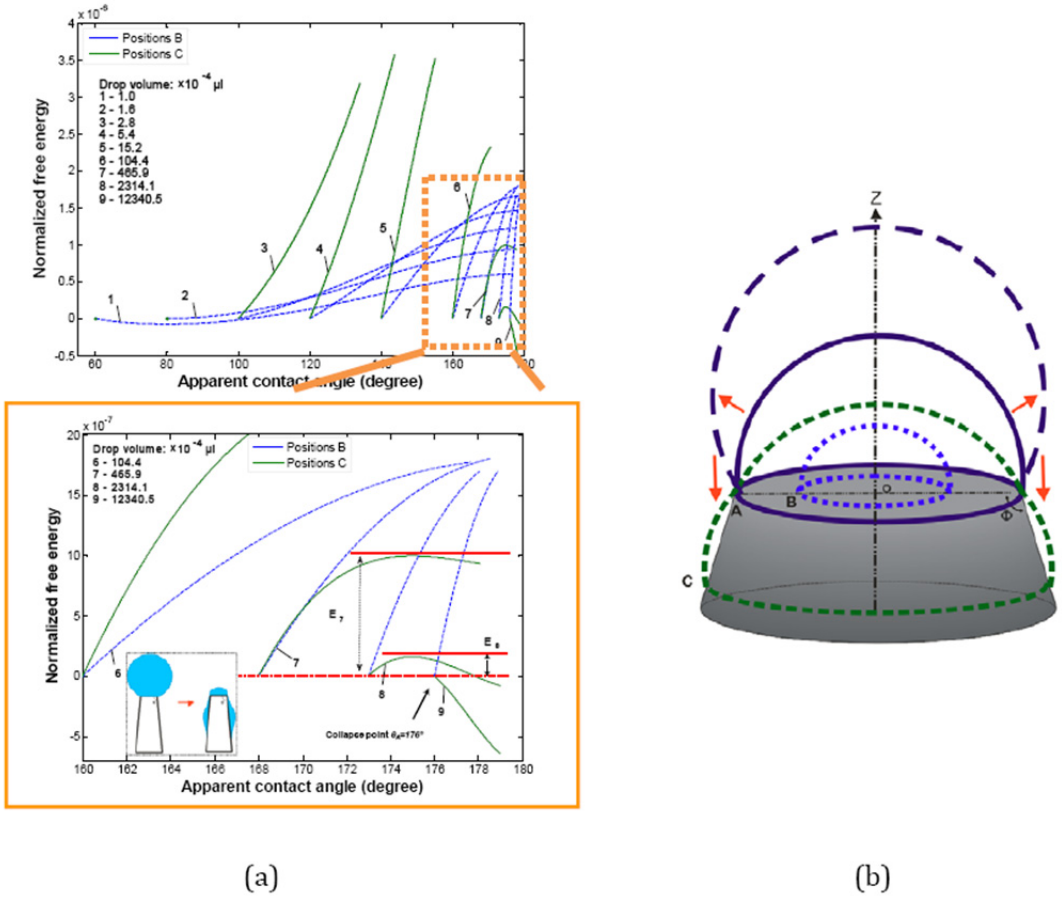

(a) (b)

Figure B-3: (a) Comparison of variations of normalized FE with apparent CA for various drop volumes (θ_Y=80°, L_A=0.001m, θ_A=40-160°, Φ=85°). The enlarged view of the dashed box is also given. (b) Schematic showing the drop spreading behaviour in wetting case C.

List of symbols/abbreviations/acronyms/initialisms

2k-4FVBA	Fluonova's Two-component Fluorinated Polyurethane sealant
3-D	Three-Dimensional
ACS	American Chemical Society
AF	Amorphous Fluoropolymer
ASME	American Society of Mechanical Engineers
ASTM	American Society for Testing and Materials
B#	Superhydrophobic coating Batch Number #
CA	Contact Angle
CAH	Contact Angle Hysteresis
CDF	Cumulative probability Distribution Function
CMC	Critical Micelle Concentration
CSM	Confocal Scanning Microscopy
CU	Complete Undercut
DI	De-Ionized
DMSO	Dimethyl Sulfoxide
DND	Department of National Defence
DRDC	Defence Research & Development Canada
DRDKIM	Director Research and Development Knowledge and Information Management
DRIE	Deep Reactive Ion Etching
EG	Ethylene Glycol
FE	Free Energy
FEB	Free Energy Barrier
HDEC	Hexadecane
HDMS	Hexamethyldisilazane
HU	Hybrid Undercut
ICNMM	International Conference on Nanochannels, Microchannels and Minichannels
IPA	Isopropyl Alcohol
L	Litre
LOC	Lab-On-Chip

LOP	Lab-On-Paper
LSG	Lesser Silicon Grass
McMat	Applied Mechanics and Materials
MSG	Major Silicon Grass
OP	Oleophobic
OTS	Octadecyltrichlorosilane
PMMA	Poly(methyl methacrylate)
POSS	Polyhedral Oligomeric Silsesquioxanes
PTFE	Polytetrafluoroethylene
R&D	Research & Development
rpm	Revolutions per minute
SA	Sliding Angle
SDS	Sodium Dodecyl Sulfate
SEM	Scanning Electron Microscopy
SH	Superhydrophobic
SHS	Superhydrophobic Surface
SIS	International Symposium on Surfactants in Solution
SOS	Superoleophobic Surface
SS	Surfactant Sensor
TFE	Trifluoroethanol
TPCL	Three-Phase Contact Line
V	Volume

This page intentionally left blank.

Distribution list

Document No.: DRDC Atlantic CR 2011-255

LIST PART 1: Internal Distribution by Centre

1 Paul Saville
3 DRDC Atlantic Library (2 CDs, 1 Hard Copy)

4 TOTAL LIST PART 1

LIST PART 2: External Distribution by DRDKIM

1 DRDKIM
1 Scott Duncan (DRDC Suffield, P.O Box 4000 Stn Main, Medicine Hat, Alberta T1A 8K6)
1 Alidad Amirfazli (Department of Mechanical Engineering, University of Alberta, 116 St. and 85 Ave., Edmonton, Alberta T6G 2G8)
1 Library and Archives Canada, Attn: Military Archivist, Government Records Branch

4 TOTAL LIST PART 2

8 TOTAL COPIES REQUIRED

This page intentionally left blank.

DOCUMENT CONTROL DATA

(Security classification of title, body of abstract and indexing annotation must be entered when the overall document is classified)

1. ORIGINATOR (The name and address of the organization preparing the document. Organizations for whom the document was prepared, e.g. Centre sponsoring a contractor's report, or tasking agency, are entered in section 8.)

Alidad Amirfazli
Department of Mechanical Engineering
University of Alberta
Edmonton, Alberta T6G 2G8

2. SECURITY CLASSIFICATION (Overall security classification of the document including special warning terms if applicable.)

UNCLASSIFIED
(NON-CONTROLLED GOODS)
DMC A
REVIEW: GCEC JUNE 2010

3. TITLE (The complete document title as indicated on the title page. Its classification should be indicated by the appropriate abbreviation (S, C or U) in parentheses after the title.)

Superomniphobic Surfaces for Military Applications: Nano- and Micro-Fabrication Methods: Year Two Report

4. AUTHORS (last name, followed by initials – ranks, titles, etc. not to be used)

Amirfazli, A.

5. DATE OF PUBLICATION (Month and year of publication of document.)	6a. NO. OF PAGES (Total containing information, including Annexes, Appendices, etc.)	6b. NO. OF REFS (Total cited in document.)
December 2011	126	92

7. DESCRIPTIVE NOTES (The category of the document, e.g. technical report, technical note or memorandum. If appropriate, enter the type of report, e.g. interim, progress, summary, annual or final. Give the inclusive dates when a specific reporting period is covered.)

Contract Report

8. SPONSORING ACTIVITY (The name of the department project office or laboratory sponsoring the research and development – include address.)

Defence R&D Canada – Atlantic
9 Grove Street
P.O. Box 1012
Dartmouth, Nova Scotia B2Y 3Z7

9a. PROJECT OR GRANT NO. (If appropriate, the applicable research and development project or grant number under which the document was written. Please specify whether project or grant.)	9b. CONTRACT NO. (If appropriate, the applicable number under which the document was written.)
12SZ20	W7707-098197

10a. ORIGINATOR'S DOCUMENT NUMBER (The official document number by which the document is identified by the originating activity. This number must be unique to this document.)	10b. OTHER DOCUMENT NO(s). (Any other numbers which may be assigned this document either by the originator or by the sponsor.)
	DRDC Atlantic CR 2011-255

11. DOCUMENT AVAILABILITY (Any limitations on further dissemination of the document, other than those imposed by security classification.)

Unlimited

12. DOCUMENT ANNOUNCEMENT (Any limitation to the bibliographic announcement of this document. This will normally correspond to the Document Availability (11). However, where further distribution (beyond the audience specified in (11) is possible, a wider announcement audience may be selected.))

Unlimited

13. ABSTRACT (A brief and factual summary of the document. It may also appear elsewhere in the body of the document itself. It is highly desirable that the abstract of classified documents be unclassified. Each paragraph of the abstract shall begin with an indication of the security classification of the information in the paragraph (unless the document itself is unclassified) represented as (S), (C), (R), or (U). It is not necessary to include here abstracts in both official languages unless the text is bilingual.)

This report explains the work accomplished during the reporting period (i.e. year 2) in four main areas: (i) Continued development of practical repellent coatings; a procedure was developed that results in improved durability under abrasion and water immersion while maintaining coating versatility. Additionally, a set of different layered superhydrophobic coatings have been proposed. (ii) Understanding the relationship between surface wear and wetting characteristics for superhydrophobic surfaces: a methodology was devised using confocal scanning microscopy that permits collection of quantitative information for surface texture. This, combined with measuring the contact angles on superhydrophobic coatings that were worn systematically, was used to compare findings with the predictions based on the classical Cassie equation. The need to develop a new relationship was identified. (iii) Theoretical work on developing fundamental knowledge about wetting of textured surfaces; a thermodynamic depiction of edge effect has been developed by free energy analysis. Results show good agreement with previous works. A universal wetting plot for describing the four wetting regions was obtained relating edge angle and intrinsic contact angle. The results have provided fundamental rules for designing robust superhydrophobic and superoleophobic surfaces. (iv) Fabrication of textured surfaces by lithographic methods to achieve repellency for oily liquids and surfactant solutions; not only were the re-entrant structures proposed in the original proposal produced, but a new structured surface, called silicon grass that shows considerable promise for oleophobicity, when compared to the re-entrant structures, was produced. The results of this work have been published in peer reviewed publications, and presented at international conferences.

14. KEYWORDS, DESCRIPTORS or IDENTIFIERS (Technically meaningful terms or short phrases that characterize a document and could be helpful in cataloguing the document. They should be selected so that no security classification is required. Identifiers, such as equipment model designation, trade name, military project code name, geographic location may also be included. If possible keywords should be selected from a published thesaurus, e.g. Thesaurus of Engineering and Scientific Terms (TEST) and that thesaurus identified. If it is not possible to select indexing terms which are Unclassified, the classification of each should be indicated as with the title.)

Cassie Baxter; Wenzel; Contact Angle; Superhydrophobic; Superorganophobic; Superomniphobic; Wetting; Lithography; Roughness; Wear; Coating

This page intentionally left blank.

Defence R&D Canada

Canada's leader in defence
and National Security
Science and Technology

R & D pour la défense Canada

Chef de file au Canada en matière
de science et de technologie pour
la défense et la sécurité nationale

www.drdc-rddc.gc.ca